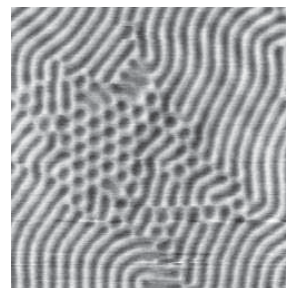
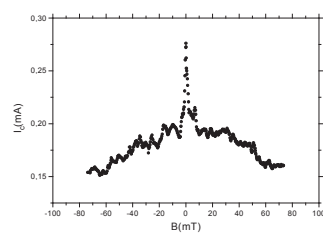
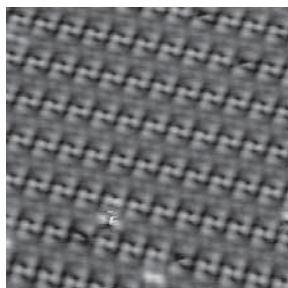
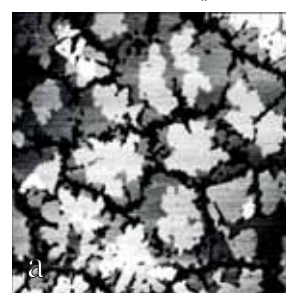
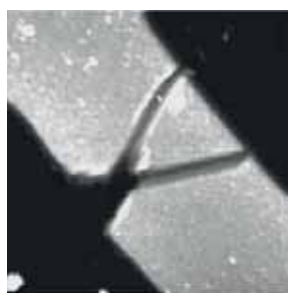
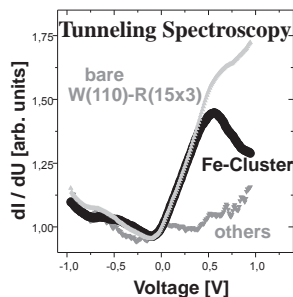
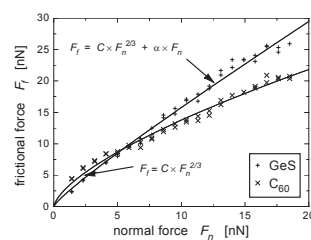
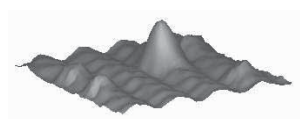


Triannual Report 1993 — 1995

Research Group “Scanning Probe Methods”



University of Hamburg
Microstructure Advanced
Research Center Hamburg
and Institute of Applied Physics



Triannual Report 1993 — 1995

Research Group “Scanning Probe Methods”



University of Hamburg
Microstructure Advanced
Research Center Hamburg
and Institute of Applied Physics

Jungiusstraße 11
D-20355 Hamburg, Germany

Contact:

Prof. Dr. Roland Wiesendanger

Tel. (++)49 40-4123-5244 (direct)

(++)49 40-4123-2028 (secretary)

FAX (++)49 40-4123-6368

e-mail wiesendanger@physnet.uni-hamburg.de

Contents

1	Preface	3
2	Staff Members	5
3	Research Activities 1993-95	7
3.1	Overview	7
3.2	Scanning Tunneling Microscopy/Spectroscopy	11
3.2.1	Carbon-induced reconstructions on W(110)	11
3.2.2	Distance-dependent STM-study of the W(110)/C-R(15×3) surface	16
3.2.3	Imaging and tunneling spectroscopy of individual iron adsor- bates at room temperature	23
3.2.4	Nanostructural and local electronic properties of Fe/W(110) correlated by scanning tunneling spectroscopy . .	26
3.3	Scanning Force Microscopy	30
3.3.1	Growth of C ₆₀ thin films on GeS(001) studied by scanning force microscopy	30
3.3.2	Study of growth stages of YBa ₂ Cu ₃ O _{7-x} thin films and YSZ buffer layers on silicon substrates	34
3.3.3	Scanning force microscopy goniometry	38
3.3.4	Load dependent topographic and friction studies of individual ion tracks in layered materials by scanning and lateral force mi- croscopy	41
3.4	Friction Force Microscopy/Spectroscopy	44
3.4.1	Quantification of friction force microscopy measurements	44
3.4.2	Low-load friction behavior of C ₆₀ thin films	48
3.4.3	Atomic friction in a nonsymmetric potential	51
3.4.4	Anisotropy of sliding friction on the TGS (010) surface	54
3.5	Electrostatic Force Microscopy on ferroelectric crystals	59
3.6	Magnetic Force Microscopy and Tunneling Stabilised Magnetic Force Microscopy	63
3.6.1	Structure of cross-tie wall in thin Co films resolved by magnetic force microscopy	64

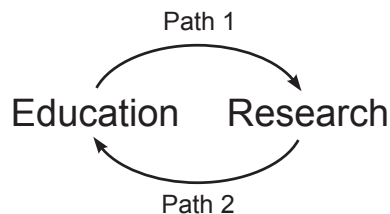
3.6.2	Domain structure of Co/Pt multilayers	66
3.6.3	Tunneling stabilized magnetic force microscopy of $BaFe_{12}O_{19}$ with a magnetic thin film tip	71
3.7	Scanning Capacitance Microscopy	73
3.8	Scanning Thermal Microscopy	77
3.9	Nanostructure fabrication	79
3.9.1	Nanofabrication of weak links based on scanning force methods	79
3.9.2	Surface modifications of magnetic thin films	84
3.9.3	Local charge modifications of nitride-oxide-silicon heterostructures	89
4	Collaborations	93
4.1	Research Partners	93
4.2	Industrial Partners	95
5	Theses	96
5.1	Diploma Theses	96
5.2	Ph. D. Theses	98
6	Scientific Publications	100
6.1	Books	100
6.2	Book Contributions and Review Articles	100
6.3	Original Publications	102
7	Talks	105
7.1	Invited Talks	105
7.2	Conference Contributions and Talks at Other Institutes	107
8	Talks Given by Guests	111
9	Lectures and Courses at the University of Hamburg	116
10	Contributions to International Organisations and Journals	117
11	How to reach us ...	118

Chapter 1

Preface

This is the first triannual report of the research group “Scanning Probe Methods” at the Institute of Applied Physics of the University of Hamburg. The research group “Scanning Probe Methods” started its activities in Hamburg in February 1993 and is embedded in the recently established “Microstructure Advanced Research Center Hamburg (MARCH)” being funded partially by the Bundesland Hamburg and partially by the Federal Government.

The general goal of this new Center is the fabrication of artificial micro- and nanostructures by complementary techniques (including molecular beam epitaxy, photolithography, electron beam lithography, scanning probe nanofabrication) and their investigation by various microscopical and spectroscopical methods (see also the special brochure about MARCH).



Particular emphasis is put on the interaction between education and research including two important paths:

- *Path 1* has been stressed by incorporating the new Center for Microstructure Research directly into pre-existing buildings of the Institute of Applied Physics of the University of Hamburg, thereby guaranteeing the coexistence of lecture halls and special research laboratories side by side. This facilitates greatly the involvement of young undergraduate students into state-of-the-art research activities which is essential to bring new ideas and new enthusiasm into ongoing research projects.
- *Path 2* is strengthened by special courses on “hot research topics” offered by our academic staff for undergraduate as well as graduate students of our University. For instance, a special two-years-course on “Scanning Probe Microscopy

and Spectroscopy: Methods and Applications” has been introduced which is accompanied by a new textbook with the same title. Other education activities at our Center include a lecture series entitled “The Physics of Microstructures” as well as a series of symposia organized by all colleagues of the Research Center. These activities greatly enhance the exchange of ideas with scientists from other research institutions all over the world.

We decided to favor a triannual rather than an annual report in order to emphasize the medium term research achievements and to distinguish the time scale of this report from that of ordinary scientific publications. To keep the extent of this report at a reasonable level we will only provide short summaries of the results of our research projects. For further information, please do not hesitate to contact us. We will be glad to provide reprints of publications on specific topics.

This research report provides a good opportunity to thank all members of the group “Scanning Probe Methods” for their efforts and achievements during the past three years. The set-up of completely new instrumentation and infrastructure within a minimum time period for competitive SPM research has represented a major challenge to all of us. We gratefully acknowledge the excellent support particularly during this difficult time period by our secretaries, the central mechanical and electronical workshops, as well as the administration of our physics department.

Finally, we are all aware of the fact that research at the forefront of science would not be possible without major financial funding from various sources. Therefore, we would like to thank the Bundesland Hamburg, the Federal Ministry for Education and Research (BMBF), the VW Foundation, the Deutsche Forschungsgemeinschaft, as well as the European Community for their support. Additionally, we thank the Studienstiftung des Deutschen Volkes and the Deutsche Akademische Austauschdienst for their support of young members of our research group as well as of foreign academic guests.

Hamburg, December 1995

Prof. Dr. Roland Wiesendanger

Chapter 2

Staff Members

Head

Prof. Dr. Roland Wiesendanger

Secretary

Renate Schulze

Petra Roth (since August 1995)

Birgit Kowitz (left April 1995)

Technical Support

Dipl.-Ing. Christian Wobbe

PTA Norbert Dix

Senior Scientists

Dr. Shuheng Pan (left November 1995)

Dr. Udo Schwarz

Dr. Andrzej Wadas

Ph. D. Students

Wolf Allers

Hendrik Bluhm

Matthias Bode

Ralph Dombrowski

Michael Dreyer

Markus Löhndorf

René Pascal

Alexander Schwarz

Christian Wittneven

Diploma Students

Jörn Asmussen

Axel Born

Cathérine Hahn (left October 1995)

Stefan Heinze

Hendrik Hölscher

Peter Köster (left October 1995)

Wolfgang Kresse

Slavomir Lukas (left August 1994)

Jens Müller

Carsten Oldorf (left Februar 1995)

Martina Seider (left October 1995)

Martin Winzer

Christian Witt

Christoph Zarnitz

Bernd Zenker (left March 1995)

Oliver Zwörner

Chapter 3

Research Activities 1993-95

3.1 Overview

Our research activities are concentrated on nanometer-scale science and technology based on scanning probe methods. In particular, emphasis is put on the investigation of the fundamental relationship between nanostructure and nanophysical properties. Scanning probe methods are ideally suited for such investigations because they provide high spatial resolution combined with spectroscopic capabilities. By choosing an appropriate type of interaction between probe tip and sample, almost any kind of nanophysical property can be studied by scanning probe methods. We apply scanning probe methods (SPM) to various classes of materials, including metals, semiconductors, insulators, superconductors, magnetic materials, molecular thin films etc. Particular emphasis is put on the investigation of *new materials*, including fullerenes (sections 3.3.1 and 3.4.2) and high- T_c superconductors (section 3.3.2), as well as *nanostructured materials*, including nanoparticles (section 3.3.3), ultra-thin films (sections 3.2.4, 3.3.2, 3.6.3) and multilayer systems (section 3.6.2). Laterally nanostructured materials are obtained by using SPM-based nanofabrication processes, which may be based on strong mechanical (section 3.9.1), electronical (section 3.9.3) or magnetic (section 3.9.2) interaction between probe tip and sample. A major goal is the combination of SPM based nanofabrication processes with conventional methods of microfabrication (including photolithography and electron beam lithography) in order to obtain useful nanoelectronic devices. An example is presented in section 3.9.1.

To be able to make significant contributions in this rapidly developing field, a major part of our activities has to be devoted to further improvements on SPM instrumentation, including the development of novel positioning devices with nanometer-scale accuracy and the development of novel types of nanosensors. Particular emphasis is also put on the development of novel experimental methods based on the local probe geometry, which usually requires adjustments of the hardware as well as of the software for SPM data acquisition. These developments are often made in close collaboration with European industrial companies specialized in SPM instrumentation.

In the following, we provide a brief summary of the highlights of our research

activities in the time period 1993–1995 which you will find in this report. This may help to guide you directly to the chapters of your specific interest.

1. Surface structure determination

In section 3.2.1, we describe the first atomic-resolution STM studies of the clean W(110) surface as well as carbon-induced (15×3) and (15×12) reconstructions of W(110). Based on our STM data, contradictory models of these reconstructions proposed earlier on the basis of diffraction data could be tested. The importance of direct real-space observations for the determination of complicated surface structures with large unit cell size became evident. On the other hand, our distance-dependent STM study of the W(110)/C-R(15×3) surface has shown that the interpretation of STM data in the case of multicomponent surfaces with large unit cell can be complicated due to the different decay rate of different Fourier components in the expansion of the surface electronic charge density as well as the spatial variation of the decay rate of the electronic wavefunctions due to the different chemical species present on multicomponent surfaces. A detailed comparison with electronic structure calculations is therefore required.

2. Imaging and tunneling spectroscopy of individual adsorbates at room temperature

In section 3.2.4, we describe the first STM spectroscopic study of individual adsorbates on metal surfaces at room temperature. It was found that the diffusion barrier for individual iron adatoms and small clusters on the W(110)/C-R(15×3) surface is sufficiently high to prevent the iron adsorbates from being mobile at room temperature. This allowed to position the STM tip above individual adsorbates and to record local tunneling spectra. A characteristic empty-state peak for iron adsorbates has been found which has already been observed earlier in low-temperature tunneling spectroscopy studies of individual iron adsorbates on Pt(111) by Eigler and coworkers. This empty-state peak appears to be independent of the chosen substrate and can therefore act as a fingerprint for iron species. This offers novel possibilities for chemical-selective imaging based on spatially-resolved tunneling spectroscopy. In addition, spin-resolved electronic structure calculations have shown that this empty-state peak originates almost exclusively from minority spin-states and therefore offers great opportunities for atom-resolved spin-polarized STM studies as well.

3. Thin film growth studies

Scanning tunneling microscopy (STM) has been applied to study the growth of ultra-thin iron films (up to about ten monolayers) on W(110) as a function of substrate temperature. Complementary studies of their nanoelectronic properties have been performed by spatially-resolved tunneling spectroscopy (section 3.2.4). Scanning force

microscopy (SFM) has been used to study the growth behavior of two types of thin film systems: $\text{YBa}_2\text{Cu}_3\text{O}_{7-x}$ on Si(100) with a YSZ buffer layer (section 3.3.2) and C_{60} on GeS(001) (section 3.3.1). The influence of the deposition parameters (e.g. substrate temperature, deposition rate etc.) on the growth morphology has been characterized in detail. The GeS(001)/ C_{60} -system was studied in view of complementary nanotribological investigations (section 3.4.2), whereas the Si(100)/YSZ/YBaCuO system is of interest for future complementary low-temperature spectroscopic studies.

4. Point-contact friction studies

In section 3.4.2, we report on a detailed nanotribological study of ultra-thin C_{60} films on GeS(001) substrates by friction force microscopy (FFM) and spectroscopy (FFS). For the first time, a contrast reversal as a function of the applied loading force for a multicomponent system has been observed by FFM. The origin of this contrast reversal has been found in the different dependence of the frictional force F_f on the applied loading force F_n for the C_{60} thin film compared with the GeS(001) substrate as revealed by FFS. The $F_f(F_n)$ -dependence on the C_{60} film follows a 2/3-power law characteristic for a sphere-versus-flat contact, whereas a linear $F_f(F_n)$ -dependence, as well known from macroscopic contact behaviour (Amontons' law), is observed for the GeS(001) substrate. The experimental results clearly indicate that detailed investigations of the nanomechanical properties are required before any conclusions about "chemical contrast" based on FFM data can be drawn.

5. Nanomagnetic properties of ultra-thin films and metallic multilayers

Magnetic force microscopy (MFM) has been applied to study in detail magnetic domain structures in ultra-thin Co films (section 3.6.3) as well as in Co/Pt-multilayer systems (section 3.6.2). We also used MFM to investigate domain structures in various hard magnetic (Ba-ferrite, Co-Cr thin film) as well as soft magnetic (permalloy and garnet thin film) materials. The relationship between microstructure and micro-/nanomagnetic structure was studied in detail for magnetite single crystals, garnet as well as permalloy thin films by simultaneous topographic and magnetic imaging techniques. In addition, we used SFM-based nanofabrication methods to intentionally modify the surface microstructure of permalloy thin films and to study the influence of these modifications on the corresponding micromagnetic structure (section 3.9.2).

6. Nanoelectronic properties of semiconductor heterostructures

Electronic properties of nitride-oxide-silicon (NOS) heterostructures on a submicrometer scale have been probed by scanning capacitance microscopy (SCM) and spectroscopy (SCS) (see section 3.7). Spatial inhomogeneities in the charge distribution are revealed by measuring the capacitance between a metallized SFM tip in contact with the top nitride layer and the doped silicon substrate spatially resolved. Upon

the application of bias voltage pulses between the SFM tip and the silicon substrate, charge carriers were enabled to tunnel through the oxide layer which was chosen to be sufficiently thick to prevent recombination processes.

Therefore, charge dots on a submicrometer scale could be created which remained stable in time. If the tribological problems originating from the tip-sample contact can be eliminated, this nanoelectronic modification process could become useful for ultra-high density charge storage devices.

7. Combination of SPM-based nanometer-scale modifications with conventional photolithography for the fabrication of weak links in superconducting microbridges

The combination of conventional microfabrication techniques and SPM-based nanofabrication has been demonstrated by the modification of photolithographically patterned microbridges of low- T_c and high- T_c superconducting materials by means of a scanning force microscope resulting in weak link structures. Low-temperature transport measurements on the modified microbridges, including measurements of the critical current density as a function of an externally applied magnetic field, proved the successful fabrication of weak links by direct writing with a tailored SFM tip. Diamond tips had to be used in order to be able to mechanically modify Nb- and $\text{YBa}_2\text{Cu}_3\text{O}_{7-x}$ microbridges by the SFM. Similar nanometer-scale modifications based on SFM were demonstrated on metallic thin films on insulating substrates.

In the following, we will describe the SPM studies mentioned above as well as further investigations on nanostructured materials in more detail.

3.2 Scanning Tunneling Microscopy/Spectroscopy

3.2.1 Carbon-induced reconstructions on W(110)

R. Pascal and M. Bode

The preparation of a W(110) single crystal in UHV by heating results in a surface layer of tungsten-carbide, originating from carbon from the bulk of the crystal. The accompanying reconstruction was first observed and identified by Stern in 1964 [1] using LEED, and has been denoted R(15×3) because of its 15-fold increase of periodicity between the (0,0) and (3,4) tungsten spots and its 3-fold periodicity between (0,0) and (0,1). Since then, many experiments were carried out and some models were elaborated to clarify stoichiometry and structure of the reconstructed surface [2,3]. Some of the models could be rejected according to the experiments but, until now, no clear decision between the two most probable, but contrasting models could be made. One model was elaborated by Bauer [4] and explains the LEED-pattern by a surface layer of hexagonal W_2C , with size and orientation of the unit cell slightly differing from the substrate. The coincidence of the atoms of surface and substrate leads to a so called “apparent superstructure” in the LEED-pattern. This interpretation was supported by x-ray diffraction studies of strong carburised tungsten [5]. In 1968 Baudoing and Stern [6] discovered the R(15×12)-reconstruction and gave evidence for a periodic surface deformation as the origin of the reconstruction, based on measurements of spot-profile

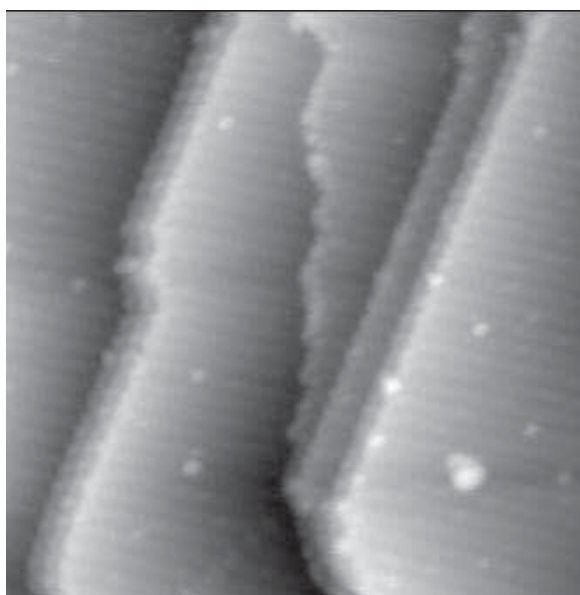


Figure 3.1: STM-image of the W(110)/C surface showing single and multiple steps. The scan-size is $375 \text{ \AA} \times 375 \text{ \AA}$.

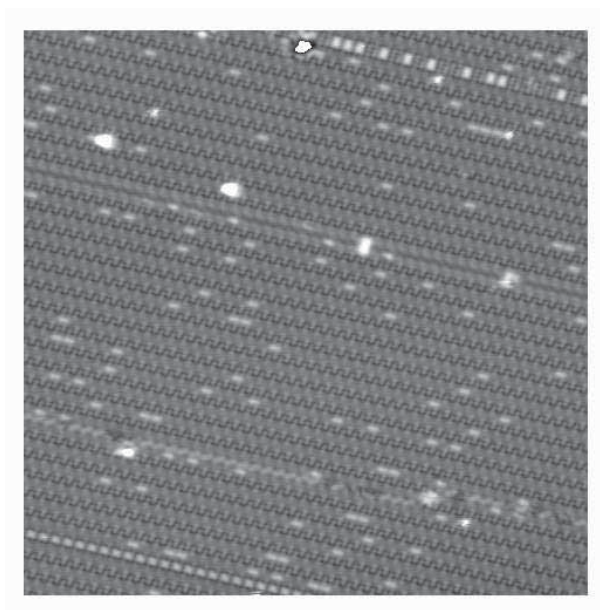


Figure 3.2: Scan area of $400 \text{ \AA} \times 400 \text{ \AA}$ on an atomically flat terrace. The tunneling parameters are $U_{gap} = 80 \text{ mV}$, $I = 60 \text{ pA}$.

analysis and diffuse scattering LEED. We obtained the first atomic resolution STM-images of the carbon induced reconstructions on W(110) [7]. The data give strong evidence for the reconstructions to originate from a periodic surface deformation.

We used electrochemically etched tungsten tips as well as cut Pt80/Ir20-tips. The experimental results were found to be independent of the tip material. STM-data shown here were measured in the constant-current mode and represent raw-data. For preparing the R(15×12)-reconstruction, the W(110)-crystal was heated by electron bombardment up to a temperature $T = 2400 \pm 50 \text{ K}$ in a pressure $p < 10^{-7}$ torr, followed by rapid cooling (quenching). The resulting LEED-pattern allowed to determine the periodicities of the unit cell of the reconstruction to be $13.7 \pm 0.1 \text{ \AA}$ and $7.7 \pm 0.1 \text{ \AA}$, which is in correspondence with literature, as well as the position of maxima and minima in I-V-curves of the R(15×3)-spots. By increasing the preparation temperature up to $2600 \pm 50 \text{ K}$, we succeeded in preparing the R(15×12)-reconstruction as observed earlier by LEED, which is in general agreement with other reports [6].

The W(110)-sample could not be cleaned of carbon by merely flashing at higher temperatures. Instead, it was exposed to 10^{-7} torr of oxygen for 30 minutes at 1750 K with several flashes up to 2600 K. After a final flash to 2600 K in UHV we obtained the (1×1)LEED-pattern and STM images of clean W(110).

Figure 3.1 shows an STM-overview image of the W(110)/C-R(15×3) surface. Single and multiple atomic steps are separated by terraces of $\sim 100 \text{ \AA}$ width. On top of the terraces — perpendicular to the steps — stripes with a periodicity of 13 \AA appear. A smaller area within an atomically flat plane is shown in Figure 3.2. Obviously,

the stripes exhibit a zig-zag-structure. Four structural domain boundaries, decorated partially with adsorbates, as well as single adsorbed atoms appear in addition.

In Figure 3.3 a) an STM-image with a scan area of only $35 \text{ \AA} \times 35 \text{ \AA}$ is shown. Every stripe appears to have alternating “legs” on both sides. The STM-data yields a size of the unit cell of $13.0 \pm 0.7 \text{ \AA} \times 7.9 \pm 0.2 \text{ \AA}$, which is in excellent agreement with the literature [1]. Although the image was taken on the atomic scale, the inner structure of the unit cell is not resolved at high tunneling gap resistance. Upon changing the tunneling parameters towards low tunneling resistance, the inner structure of the unit cell became visible. Figure 3.3b shows an image with highest spatial resolution. Six maxima per unit cell appear, showing a twofold symmetry. The distance between two adjacent maxima is $3.25 \pm 0.15 \text{ \AA}$ and $3.9 \pm 0.1 \text{ \AA}$ in the $[\bar{1}11]$ - and $[\bar{1}1\bar{2}]$ -direction, respectively. This leads to the conclusion, that the surface is not covered with a closed surface layer of hexagonal W_2C , as assumed by Bauer. Otherwise we would expect to see a threefold symmetry of the surface atoms, with the nearest neighbour distance near 2.99 \AA , as for the (0001)-surface of αW_2C . This interpretation is consistent with atomic beam diffraction studies [8], that confirmed the size of the unit cell. Since this technique is sensitive only to the topmost layer, it should not show a diffraction pattern, that originates from multiple scattering between first and second layer.

By increasing the preparation temperature, we succeeded in the preparation and imaging of the $R(15 \times 12)$ -reconstruction on $W(110)/C$. Figure 3.4a shows this reconstruction at high tunneling gap resistance, where it shows a complex inner structure. It consists of square shaped and slightly tilted protrusions of $9 \times 9 \text{ \AA}$ size while two smaller ones appear between them. The size of the unit cell is $13.3 \pm 1.0 \text{ \AA}$ by 31.7

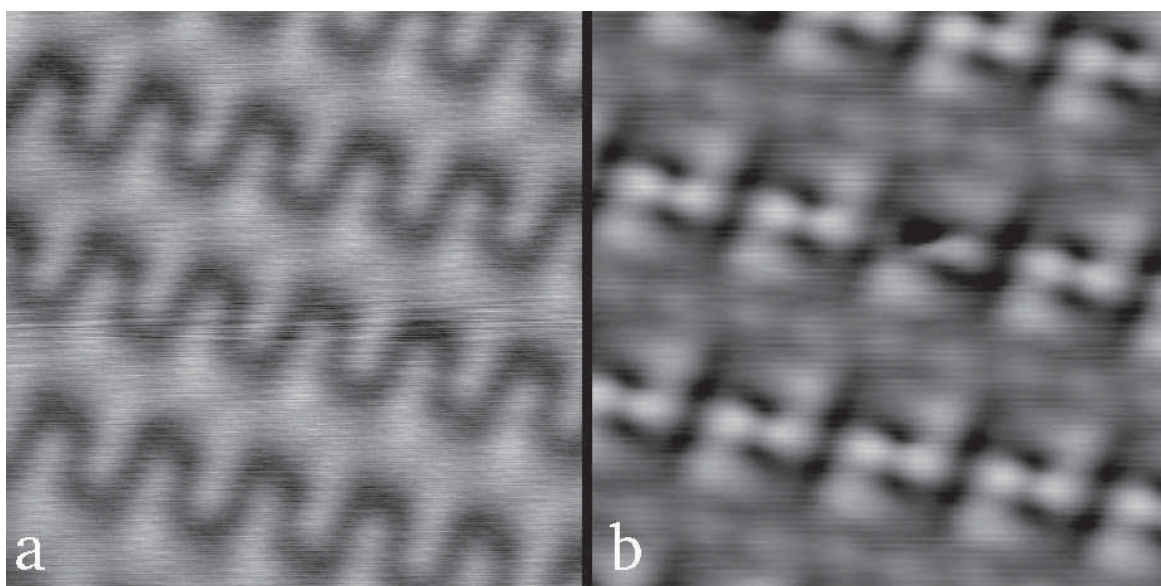


Figure 3.3: The carbon induced $R(15 \times 3)$ reconstruction, measured at high (a: $U_{gap} = 680 \text{ mV}$, $I = 60 \text{ pA}$) and low (b: $U_{gap} = 22 \text{ mV}$, $I = 10.4 \text{ nA}$) tunneling gap resistance.

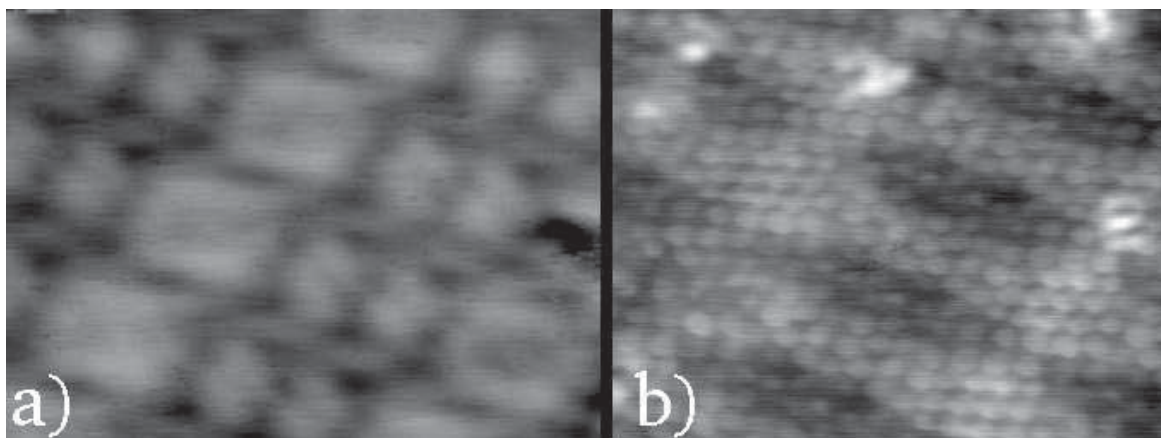


Figure 3.4: The R(15 \times 12) reconstruction, measured at high (a: $U_{gap} = 680$ mV, $I = 60$ pA); and low (b: $U_{gap} = 22$ mV, $I = 10.4$ nA) tunneling gap resistance. The atomic pattern in b) exhibits the periodicities and unit cell of clean W(110), but with a periodic vertical surface lattice distortion.

± 3.0 Å, which is consistent with literature [6]. Again, atomic resolution is achieved at low tunneling gap resistance in Figure 3.4b. An atomic pattern, showing the periodicity and unit cell of clean tungsten, is periodically distorted by a vertical buckling of the surface and a slight lateral shift of surface atoms in the lower parts of the unit cell.

The appearance of the R(15 \times 12) surface, as seen by STM, matches exactly the model of Stern for the carbon induced reconstructions on W(110). In this model, based on diffuse scattering LEED studies [6], carbon is incorporated in the tungsten surface resulting in a periodic vertical buckling, but not in formation of a closed layer of tungsten carbide. These LEED studies also predict a higher vertical buckling of the R(15 \times 3)- than for the R(15 \times 12)-structure. Our data are in good agreement with these studies, because they show a corrugation of 0.3-0.5 Å for the R(15 \times 3)- and a corrugation of less than 0.2 Å for the R(15 \times 12)-structure.

In summary, we resolved the carbon-induced reconstructions on W(110) atomically. Our results suggest, that the origin of the carbon induced reconstructions on W(110) is not a closed surface layer of tungsten carbide, that leads to an “apparent superstructure” in the LEED-pattern, but indeed a surface lattice deformation, triggered by carbon and driven by the minimisation of the total surface energy.

References

- [1] R. M. Stern, *Appl. Phys. Lett.* **5** 218 (1964).
- [2] K. J. Rawlings, S. D. Foulis and B. J. Hopkins, *J. Phys. C* **14** 5411 (1981).
- [3] J. G. MacMillan, A. J. Slavin and K. J. Sunderland, *Surf. Sci.* **173** 138 (1986).
- [4] E. Bauer, *Surf. Sci.* **7** 351 (1967).

- [5] D. F. Ollis and M. Boudart, Surf. Sci. **23** 320 (1970).
- [6] R. Baudoing and R. M. Stern, Surf. Sci. **10** 392 (1968).
- [7] M. Bode, R. Pascal, and R. Wiesendanger, Surf. Sci. (in press).
- [8] W. H. Weinberg and R. P. Merrill, J. Chem. Phys. **56**, 2893 (1972).

3.2.2 Distance-dependent STM-study of the W(110)/C-R(15×3) surface

M. Bode and R. Pascal

One of the most important features of any microscopy is its image contrast formation. In the case of scanning tunneling microscopy (STM) [1,2], the applied bias voltage between tip and sample has been recognized a long time ago as an important parameter, particularly for the investigation of semiconductor surfaces[3-5]. On the other hand, the dependence of STM images on the tip-surface separation has been studied in detail only in some rare cases and for relatively simple surface structures, such as Al(111) [6].

In the present study, we have selected the non-trivial W(110)/C-R(15×3) surface structure as a model system for distance-dependent STM investigations. The STM-images of this surface do not depend significantly on the applied bias voltage, as known for metals. However, we have found a strong influence of the tip-surface separation on the STM image contrast which is related with the suppression of small wavelength features and the spatial dependence of the decay length of the surface wavefunction for multicomponent surfaces.

The experiments were performed under ultra-high vacuum (UHV) conditions ($p \approx 5 \times 10^{-11}$ torr). The preparation of the W(110)/C-R(15×3) reconstructed surface and its characterization by a combined STM and LEED (low energy electron diffraction) study has been described in the previous report.

Figure 3.5 shows a series of five STM images of the same size of the W(110)/C-R(15×3) reconstruction for different values of the tunneling gap resistance R and therefore for different tip-surface separation. While a meander-type structure on a near-atomic scale is observed at high tunneling gap resistance [Fig. 3.5(a)], we resolved the atomic structure only at low tunneling gap resistance [Fig. 3.5(e)]. The

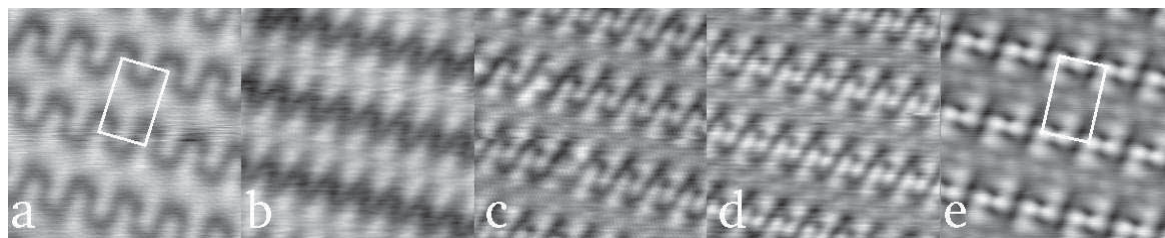


Figure 3.5: Five top-view STM images of the same size ($33\text{\AA} \times 33\text{\AA}$) of the W(110)/C-R(15×3) reconstruction measured at different values of the tunneling gap resistance R : **a**: $R = 1.72 \times 10^{10} \Omega$, **b**: $R = 2.27 \times 10^9 \Omega$, **c**: $R = 1.0 \times 10^8 \Omega$, **d**: $R = 1.2 \times 10^7 \Omega$, **e**: $R = 2.11 \times 10^6 \Omega$. A strong dependence of the apparent surface structure on the tip-surface separation is observed.

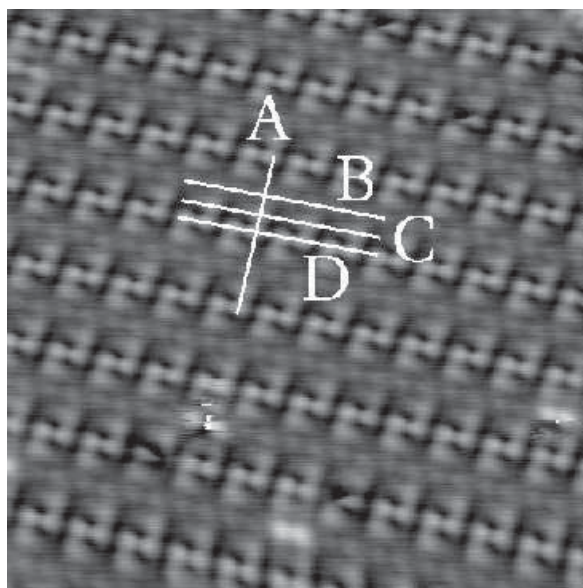


Figure 3.6: STM image with atomic resolution of the W(110)/C-R(15×3) reconstructed surface (80Å × 80Å). Along the lines A, B, C and D we extracted line sections at different tunneling gap resistances which are represented in in the next figure.

Figs. 3.5(b), 3.5(c) and 3.5(d) show the transitions between the images presented in Fig. 3.5(a) and 3.5(e). The surface unit cell has been outlined in Figs. 3.5(a) and 3.5(e) for clarity.

In total, we recorded STM images for twelve different values of the tunneling gap resistance and extracted sections along the lines indicated in Fig. 3.6. Finally, averages over eight equivalent line sections for each value of the tunneling gap resistance were taken. The data sets for the lines A, B, C and D are presented in Figs. 3.7(a-d). The STM line sections displayed in the lower part of Figs. 3.7(a-d) have been obtained at low tunneling gap resistance (i.e. at small tip-surface separation), while the STM line sections in the upper part have been recorded at high tunneling gap resistance (i.e. at larger tip-surface separation). For the data set displayed in Fig. 3.7(a) the STM corrugation is about 0.4 Å at low tunneling gap resistance ($R = 0,8 \text{ M}\Omega$) and about 0.15 Å at high tunneling gap resistance ($R = 2,27 \text{ G}\Omega$), while for the data set in Fig. 3.7(b) the STM corrugation is as small as 0.1 Å at $R = 0,8 \text{ M}\Omega$ and about 0.05 Å at $R = 2,27 \text{ G}\Omega$.

It is apparent from the data sets in Figs. 3.7(a-d) that besides the decrease of the measured STM corrugation with increasing tip-surface separation, as already reported earlier (e.g. [6]), we observe quite generally a suppression of small wavelength features by increasing the distance between tip and surface. To demonstrate this more clearly a plot of the Fourier-transformed line sections of Fig. 3.7(a) is shown in Fig. 3.8. The peaks at $G_1 = 0.073 \text{ \AA}^{-1}$ and $G_2 = 0.292 \text{ \AA}^{-1}$ represent the periodicities 13.7 Å and 3.425 Å of the W(110)/C-R(15×3) reconstructed surface in the $[\bar{1}11]$ -direction, respec-

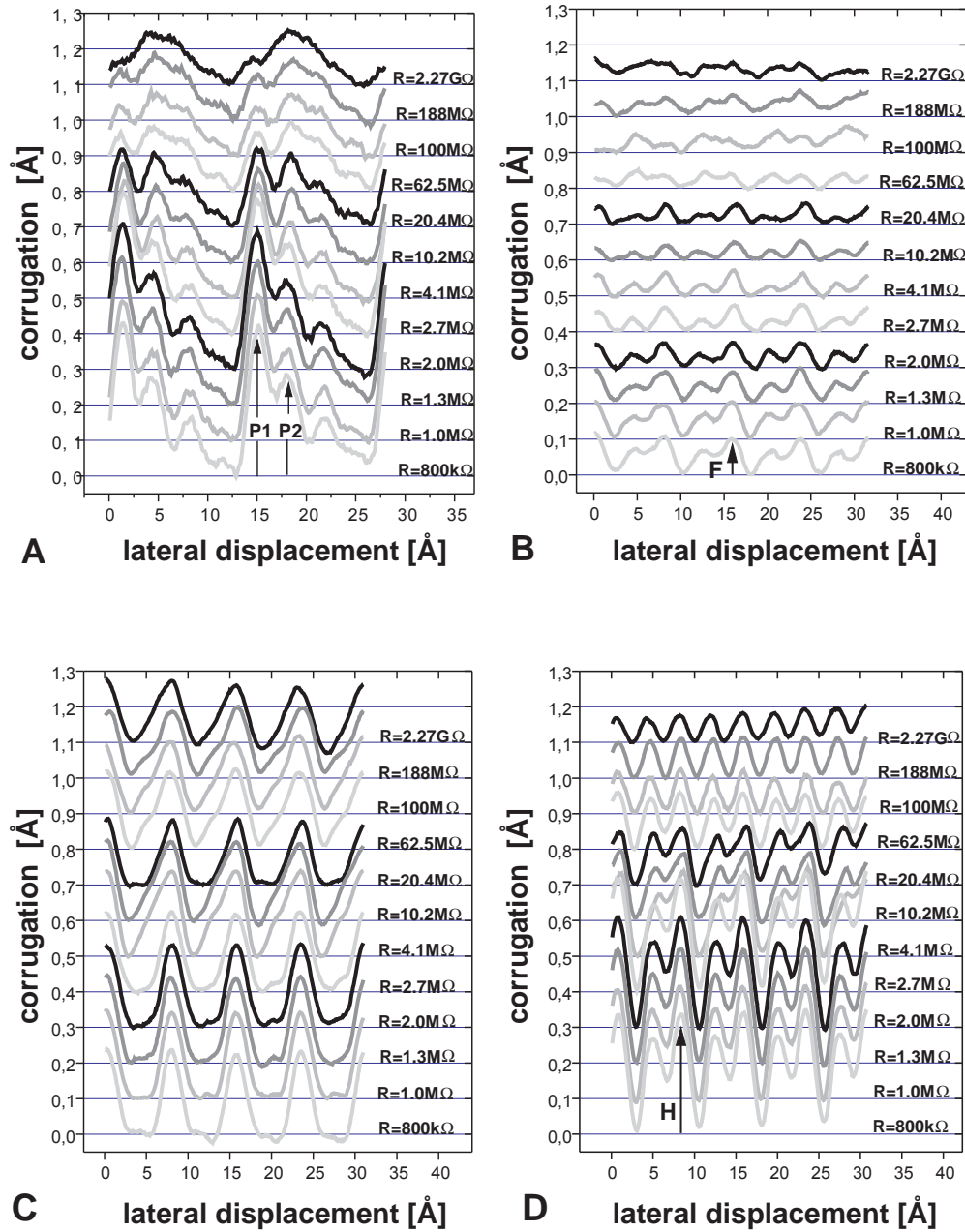


Figure 3.7: Data sets of line sections from STM images obtained with different tunneling gap resistance R along the lines A, B, C and D indicated in the previous figure.

tively. All other peaks are higher harmonics ($G = 0.146 \text{ \AA}^{-1}$ and $G = 0.219 \text{ \AA}^{-1}$) or artefacts due to the limited length of the line sections ($G = 0.036 \text{ \AA}^{-1}$). By increasing the tunneling gap resistance by more than four orders of magnitude the peak amplitude at $G_2 = 0.292 \text{ \AA}^{-1}$ is diminished to 10 % of the original value, while the peak amplitude at $G_1 = 0.073 \text{ \AA}^{-1}$ is still 60 %. In other words, higher Fourier-components

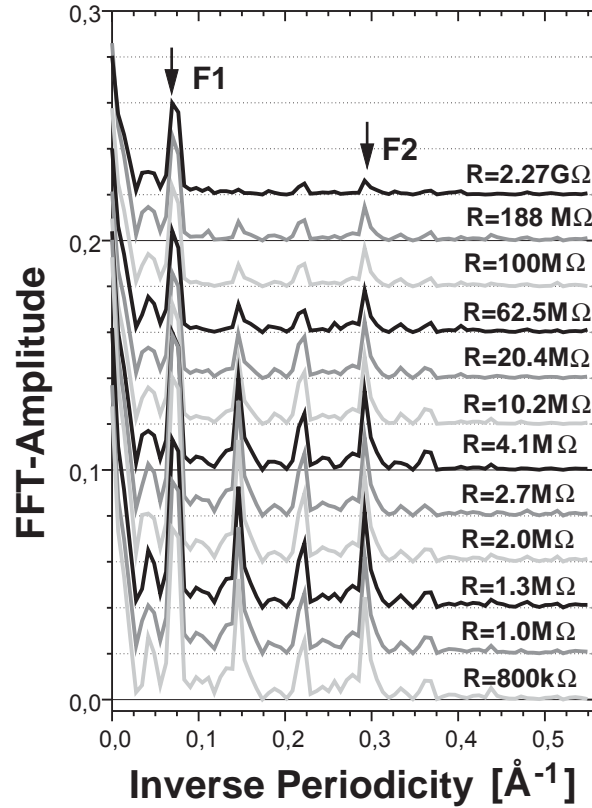


Figure 3.8: Fourier-transformed sections of Fig. 3a. The peaks F1 and F2 represent features of the W(110)/C-R(15×3) surface with the periodicities 13.7 Å ($G_1 = 0.073 \text{ \AA}^{-1}$) and 3.425 Å ($G_2 = 0.292 \text{ \AA}^{-1}$), respectively. While the peak F2, which represents small wavelength features, is suppressed to 10 % of the original value, the peak F1 is diminished weakly.

are suppressed much stronger than smaller Fourier-components. This corresponds to a degradation of the lateral STM resolution which contributes to the strong dependence of the observed STM images on the tip-surface separation as shown in Fig. 3.5.

Following the STM theory of Tersoff and Hamann [9,10] it was found that the spatial resolution is given by geometrical parameters, i.e. the effective tip radius and the tip-surface separation. The measured corrugation of reconstructed metal surfaces could be described by this model under realistic assumptions. The charge density $\rho(\vec{r}, E)$ of a periodic surface structure can be Fourier expanded:

$$\rho(\vec{r}, E) = \sum_{\vec{G}} \rho_{\vec{G}}(\vec{r}, E) \cdot \exp(i\vec{G} \cdot \vec{r}) \quad (3.1)$$

where \vec{G} denotes a reciprocal lattice vector. By defining an STM corrugation amplitude by

$$\Delta \equiv z_+ - z_- \quad (3.2)$$

where z_+, z_- are extremal values of the vertical tip position in the constant-current mode, Tersoff and Hamann [10] showed that the corrugation Δ decreases exponentially with tip-surface separation:

$$\Delta \propto \exp(-\beta z) \quad (3.3)$$

with a decay rate β being very sensitive to the reciprocal lattice vector:

$$\beta \approx (1/4)\kappa^{-1}\vec{G}^2 \quad (3.4)$$

where

$$\kappa = \hbar^{-1} \cdot \sqrt{2m\varphi}. \quad (3.5)$$

The work function φ was assumed to be identical for tip and sample surface and spatially homogeneous. Based on Equ. 3.3 and 3.4, a suppression of higher Fourier components by a factor $\exp(-(1/4)\kappa^{-1}\vec{G}^2 z)$ with increasing tip-surface separation was predicted. Though we do not have information about the absolute value of the tip-surface separation, we know [9,10] that

$$\frac{1}{R} \propto \exp(-2\kappa z) \quad (3.6)$$

By combining Equ. 3.3, 3.4 and 3.6 and introducing the relative corrugation Δ/Δ_0 and the relative tunneling gap resistance R/R_0 , we finally obtain:

$$\ln \frac{\Delta/\Delta_0}{\vec{G}^2} \propto \frac{1}{8\kappa^2} \ln \left(\frac{R_0}{R} \right) \quad (3.7)$$

In Fig. 3.9 we have plotted $\ln \left((\Delta/\Delta_0)/\vec{G}^2 \right)$ of the peaks indicated in Fig. 3.7(a), (b) and (d) against $\ln(R_0/R)$. The reference values are $R_0 = 2.27 \text{ G}\Omega$ and $\Delta_0(R_0)$. The observed linear dependence for different \vec{G} -values is in agreement with the predicted behaviour based on Equ. 3.7. The slope in the data of Fig. 3.8 is inversely proportional to the local work function φ as can be seen by combining Equ. 3.5 and 3.7. While the data sets P2, F, and H exhibit nearly the same slope, the slope of the data set P1 is 3-4 times bigger.

Apparently, φ is not spatially homogeneous for the W(110)/C-R(15×3) surface. Spatial inhomogeneities in the decay constant κ on the atomic scale are most clearly observed in the experimental data presented in Fig. 3.7(a). The strong peak (P1) in the topographic data obtained at low tunnelling gap resistance decays much faster with increasing tip-surface separation compared with the neighbour peak (P2). The most likely explanation for this observation could be the presence of two different atomic species, tungsten and carbon, in the top surface layer. However, detailed electronic structure calculations for the W(110)/C-R(15×3) surface would be required in order to support this assumption.

In conclusion, we have observed a strong dependence of STM images of non-trivial surface structures on the tip-surface separation which can be explained by the suppression of higher Fourier components, i.e. small wavelength structures, with increasing distance between tip and surface. While the energy (bias) dependence of STM images of

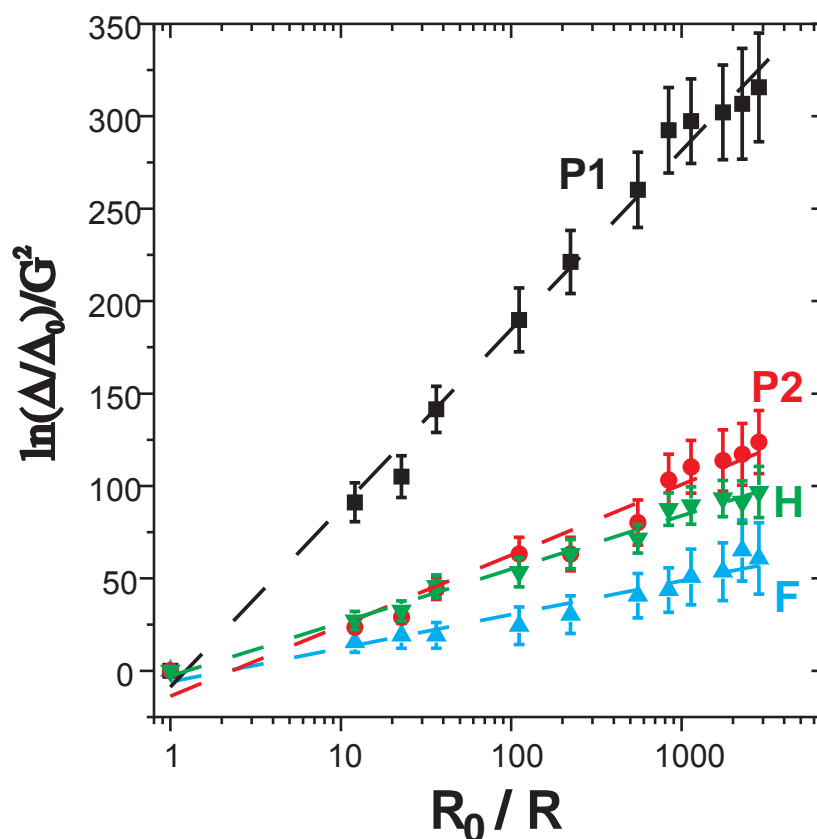


Figure 3.9: Plot of $\ln\left(\frac{\Delta/\Delta_0}{\vec{G}^2}\right)$ versus $\ln(R_0/R)$ which yields a linear dependence for different \vec{G} -values (P1 and P2: $\vec{G} = 0.073 \text{ \AA}^{-1}$, F and H: $\vec{G} = 0.13 \text{ \AA}^{-1}$) as predicted theoretically. The corrugation was measured at the peaks P1, P2, F, and H as indicated in Fig. 3.7(a), (b) and (d). The slope for each data set is inversely proportional to the local work function φ .

semiconductor surfaces has been recognized a long time ago, the distance-dependence of STM images will have to be seriously considered as well in the interpretation of experimental data obtained for non-trivial surface structures [11].

References

- [1] G. Binnig, H. Rohrer, Ch. Gerber, and E. Weibel, Phys. Rev. Lett. **49** 57 (1982).
- [2] R. Wiesendanger, Scanning Probe Microscopy and Spectroscopy: Methods and Applications, Cambridge University Press, Cambridge 1994.
- [3] R.S. Becker, J.A. Golovchenko, D.R. Hamann, B.S. and Swartzentruber, Phys. Rev. Lett. **55**, 2032 (1985).
- [4] R.M. Feenstra, W.A. Thompson, A.P. and Fein, Phys. Rev. Lett. **56** 608 (1986).
- [5] Hamers, R.J. Tromp, R.M. and Demuth, J.E. Phys. Rev. Lett. **56** 1972 (1986).

- [6] J. Wintterlin, J. Wiechers, H. Brune, T. Gritsch, H. Hfer, R.J. and Behm, Phys. Rev. Lett. **62** 59 (1989).
- [7] Micro-STM from OMICRON; Taunusstein, Fed. Rep. Germany.
- [8] M. Bode, R. Pascal, and R. Wiesendanger, Surf. Sci. (in press).
- [9] J. Tersoff, and D.R. Hamann, Phys. Rev. Lett. **50** 1998 (1983).
- [10] J. Tersoff, and D.R. Hamann, Phys. Rev. B **31** 805 (1985).
- [11] M. Bode, R. Pascal, and R. Wiesendanger, Z. Phys. B (in press).

3.2.3 Imaging and tunneling spectroscopy of individual iron adsorbates at room temperature

M. Bode and R. Pascal

Scanning Tunneling Microscopy (STM) has been used extensively in the past to study various adsorbates covalently bound to semiconductor substrates. In the case of metal substrates, however, adsorbates can only be imaged at room temperature if the adsorbate - substrate interactions are sufficiently strong to prevent surface diffusion, as e.g. for O on Ni or C on Al [1]. To image other adsorbates which are only weakly bound to metal substrates, such as noble gas atoms [2, 3], CO [4, 5] or metal species [6, 7], STM investigations have been performed at sufficient low temperatures where surface diffusion has already ceased. Here we report briefly on the first imaging and local tunneling spectroscopy of individual metal atoms and small clusters on a metal substrate at room temperature [8].

We have focussed our investigations on Fe adsorbed on a W(110) substrate with submonolayer coverage. While individual Fe atoms were found to be relatively mobile at room temperature on the clean W(110)-(1×1) surface, we were able to image individual Fe atoms and small clusters on the carbon-induced (15×3)-reconstruction of W(110). This reconstruction, which has recently been resolved by STM [9], modifies the surface potential of W(110) to allow for a sufficient strong bonding of the Fe atoms to the substrate. Consequently, they can be imaged by STM even at room temperature.

Figure 3.10(a) shows an individual Fe atom on the W(110)-C(15×3) substrate. The Fe atom appears as a protrusion with a height of $1.5 \pm 0.1 \text{ \AA}$ and a FWHM of $9.0 \pm 1.0 \text{ \AA}$. These values were found to be rather independent of the applied bias

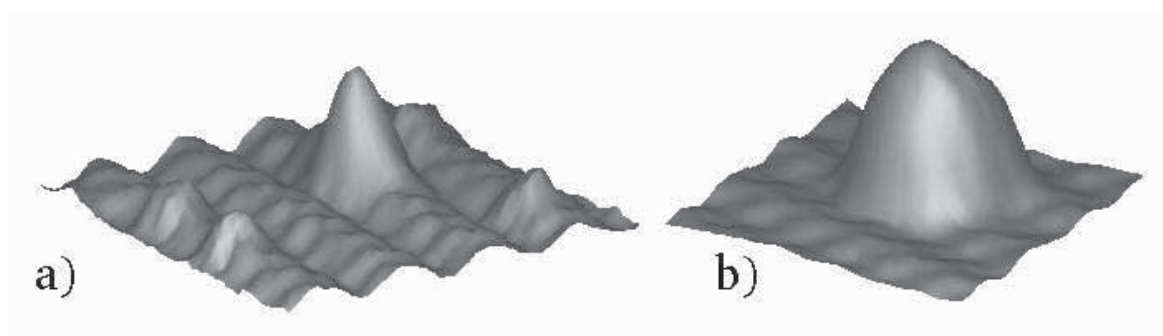


Figure 3.10: **a** Constant current STM image of a single adsorbed Fe atom on the (15×3)-reconstruction of W(110). The Fe atom has a height of $1.5 \pm 0.1 \text{ \AA}$ and a FWHM of $9.0 \pm 1.0 \text{ \AA}$. Single Fe atoms could only be observed at an extremely low coverage of less than 0.001 ML. Higher coverages resulted in clusters as shown in **b**. This cluster has a height of $2.3 \pm 0.1 \text{ \AA}$ and a FWHM of $13.9 \pm 0.3 \text{ \AA}$.

voltage and consistent with low-temperature STM results [10]. Figure 3.10(b) shows a small iron cluster with a height of $2.3 \pm 0.1 \text{ \AA}$ and a FWHM of $13.9 \pm 0.3 \text{ \AA}$. It probably consists of three individual Fe atoms. We have also studied larger clusters and small islands [8]. Based on the ability to image individual Fe adsorbate species at room temperature, we could position the STM tip above the adsorbates and obtain local tunneling spectra. Figure 3.11 shows the measured differential conductivity dI/dU as a function of the applied sample bias voltage at three different locations. Curve A was obtained above the bare W(110)-C(15 \times 3) substrate whereas curve B was measured above an Fe adsorbate similar to the one shown in Figure 3.10(b). A pronounced empty-state peak at about 0.5 eV above the Fermi level appears which was found to be characteristic for Fe adsorbate species. A similar peak has been found for Fe-atoms on Pt(111) [10] and appears to be independent of the chosen substrate and therefore can act quite generally as a fingerprint for Fe species. To illustrate this we have also plotted a third tunneling spectrum (curve C) in Figure 3.11 which was measured above another adsorbate species. The experimental results were found to be independent of the chosen tip. We have used several different W and Pt/Ir tips so far.

In summary, we performed the first room temperature STM and tunneling spec-

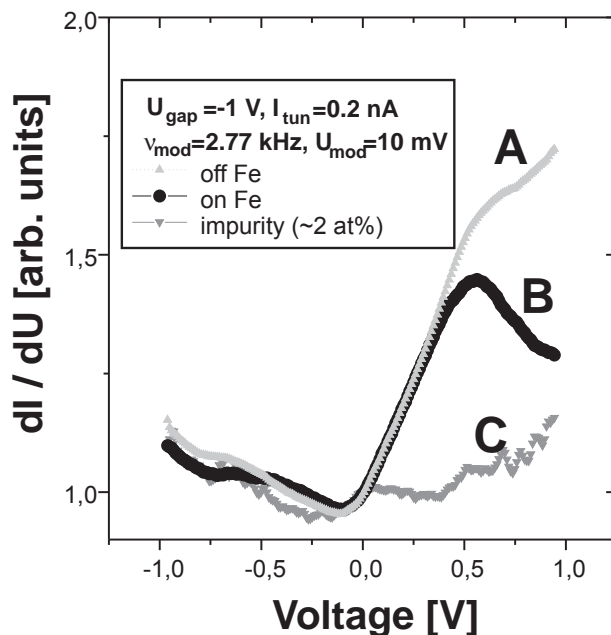


Figure 3.11: Plot of dI/dV spectra (normalized to $V = 0$) which were measured above different locations of the (15 \times 3)-reconstructed surface. The surface was decorated with 0.03 ML of Fe. Spectra, which were taken above a cluster similar to that imaged in Figure 2b, reveal a pronounced empty-state peak at 0.5 eV (B). This peak does not appear on the bare substrate (A). Approximately 2% of the adsorbates exhibited completely different spectra (C). The low differential conductivity indicates that these spectra originate from non-metallic species.

troscopy study of individual metal adatoms on a metal substrate. The tunneling spectra obtained above Fe adsorbates exhibit a pronounced peak at 0.5 eV above E_F which appears to be characteristic for Fe adsorbates and therefore can act as a chemical fingerprint.

References

- [1] J. Winterlin, R.J. Behm, in: Scanning Tunneling Microscopy I, 2nd edition, eds. H.-J. Güntherodt and R. Wiesendanger, Springer 1994.
- [2] D.M. Eigler and E.K. Schweizer, *Nature* **344**, 524 (1990).
- [3] P.S. Weiss and D.M. Eigler, *Phys. Rev. Lett.* **69**, 2240 (1992).
- [4] P. Zeppenfeld, C.P. Lutz, and D.M. Eigler, *Ultramicroscopy* **42-44**, 128 (1992).
- [5] G. Meyer, B. Neu, and K.-H. Rieder, *Appl. Phys. A* **60**, 343 (1995).
- [6] M.F. Crommie, C.P. Lutz, and D.M. Eigler, *Science* **262**, 218 (1993).
- [7] E.J. Heller, M.F. Crommie, C.P. Lutz, and D.M. Eigler, *Nature* **369**, 464 (1994).
- [8] M. Bode, R. Pascal, and R. Wiesendanger, *Z. Phys. B* (in press).
- [9] M. Bode, R. Pascal, and R. Wiesendanger, *Surf. Sci.* (in press).
- [10] M.F. Crommie, C.P. Lutz, and D.M. Eigler, *Phys. Rev. B* **48**, 2851 (1993)

3.2.4 Nanostructural and local electronic properties of Fe/W(110) correlated by scanning tunneling spectroscopy

M. Bode and R. Pascal

Research on thin solid films is of high interest since they offer the opportunity to stabilise solids in structures, i.e. with crystalline symmetries and lattice constants, that are far from those of the corresponding bulk material. This facilitates to create materials with properties that do not exist in nature. Strong effort has been made to investigate refractory 5d-transition metal substrates with high melting temperatures, such as Fe/W(110) [1-10]. Particularly, Fe shows an interesting growth behaviour on W(110) [8,10]. Although there is a large lattice misfit of 9.4% it is known that up to a coverage $\Theta = 1.3$ ML Fe grows pseudomorphically on W(110) at a substrate temperature of 570 K. Above this coverage the Fe film begins to relax. The onset of relaxation in the second Fe layer is indicated by dislocation lines along the [001]-direction with an average separation of 46 Å. The dislocation lines become periodic when the local coverage is 3 ML. From the fourth layer on the Fe film exhibits a two-dimensional dislocation periodic network.

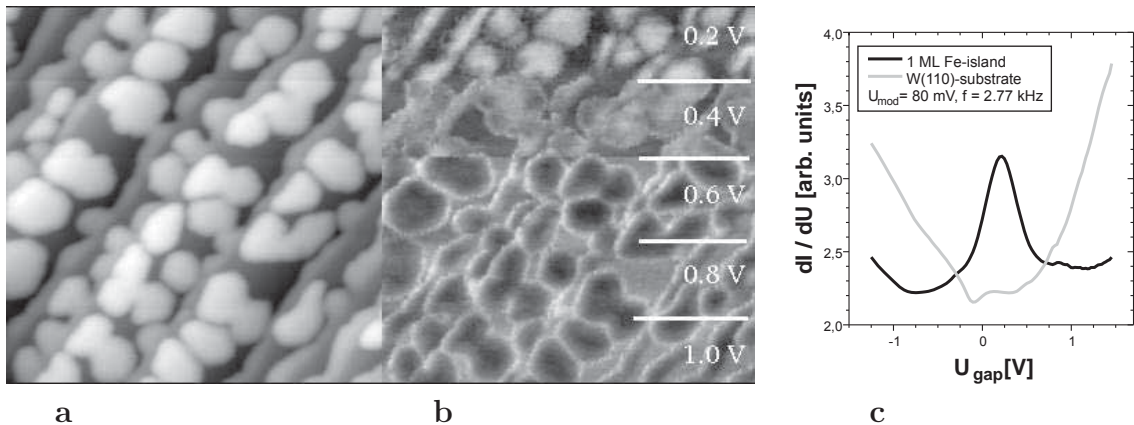
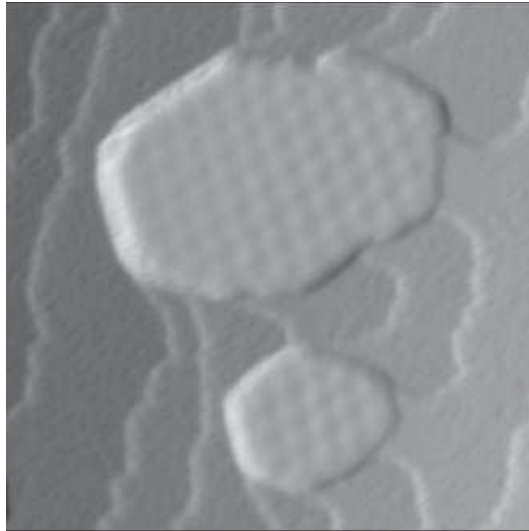


Figure 3.12: **a**: Topography of 0.45 ML Fe on W(110) deposited at room temperature. Fe forms monolayer islands and a small amount decorates the step edges. Maps of the differential conductivity dI/dV are shown in **b**. During the scan the gap voltage was decreased every 80 lines by 0.2 V. Bright and dark areas correspond to high and low differential conductivity, respectively. The contrast between Fe and W flips between $U_{gap} = 0.6$ V and $U_{gap} = 0.4$ V. **c** Averaged spectra of the differential conductivity dI/dV taken above Fe and W sites from the former image. Obviously one monolayer of Fe on W(110) exhibits an empty-state peak which is centered at $U_{gap} = 0.22$ V.

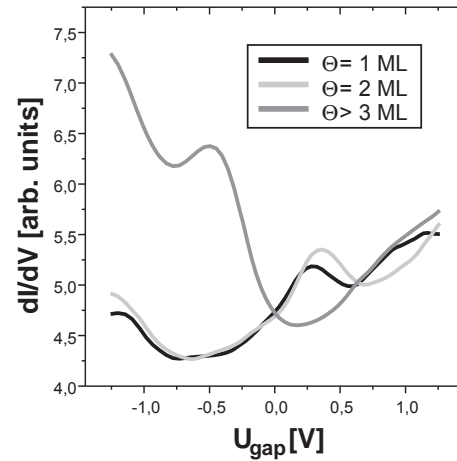
Here we report on a STS study of Fe grown on W(110). We observed directly by STS a stress-induced change of the electronic structure for Fe on W(110) which results in an increased density of states just above the Fermi level E_F [11].

The Fe films were prepared in ultra-high vacuum (UHV) on W(110) substrates held at room temperature by using an electron-beam evaporator. Upon thin film growth the sample was transferred in-situ into our UHV scanning tunneling microscope (STM). All topographic data were achieved in the constant current mode. The spectroscopic data were measured by lock-in technique.

Figure 3.12(a) shows the topography of a submonolayer Fe film ($\Theta \approx 0.45$ ML). The topography is dominated by 2D-islands. A map of the differential conductivity dI/dV is shown in Fig. 3.12(b). During the scan the gap voltage was changed in steps of 0.2 eV. Obviously the contrast between islands and substrate flips. First, at $U_{gap} = 1.0$ V the W(110) substrate appears brighter than the Fe islands, i.e. W exhibits a higher differential conductivity than Fe [Fig. 3.12(b)]. This situation remains unchanged up to a gap voltage $U_{gap} = 0.6$ V. If the gap voltage is further diminished to $U_{gap} = 0.4$ V the contrast flips and the Fe islands appear brighter than the W substrate. This behaviour can be understood based on local tunneling spectroscopy data [Fig. 3.12(c)]. While the plot of differential conductivity dI/dV versus gap voltage of the Fe monolayer exhibits a peak which is centered at $U_{gap} \approx 0.2$ V (empty sample



a



b

Figure 3.13: **a**: STM-image of a 3 ML Fe film on W(110). The film was post-annealed at $T > 600$ K. This results in Fe islands with a height of 4-12 ML. Between the islands the coverage of the pseudomorphic Fe film is 1.3 ML. **b**: Spectra of the differential conductivity dI/dV taken above positions where the local coverage is 1 ML, 2 ML or more than 3 ML. While we find an empty-state peak on pseudomorphic films this peak does not appear above the islands.

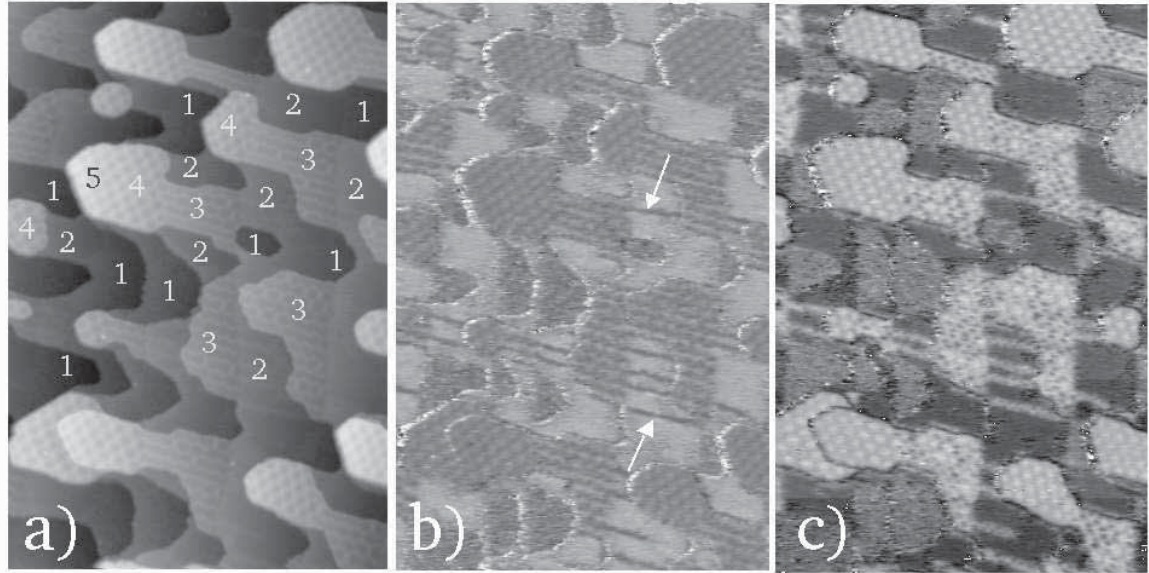


Figure 3.14: **a**: Topography of a 2 ML Fe film on W(110) after post-annealing at $T \leq 600$ K. Fe forms nanometer-scale wedges on the stepped substrate ($1 \text{ ML} \leq \Theta \leq 5 \text{ ML}$). **b**: At $U_{\text{gap}} = 0.4$ V, which is close to the position of the empty-state peak described above, the second monolayer has the higher (brighter) differential conductivity dI/dV . The differential conductivity is diminished wherever the Fe film begins to relax, i.e. at dislocation lines in the second monolayer (marked by arrows). **c** At $U_{\text{gap}} = -0.4$ V, which is close to the occupied state peak, areas appear bright when the local coverage $\Theta \geq 3$ ML. The same is true for the dislocation lines in the second monolayer.

states), W shows no significant features in the gap voltage range under study.

To check if the empty-state peak is characteristic for a thin film of Fe on W(110) or if it is also present on bulk-like Fe(110), we prepared a sample which contains simultaneously different regimes of coverage. We evaporated 3 ML of Fe on the W(110) substrate and post-annealed the sample at a temperature $T > 600$ K for 2 minutes. This results in a topography as displayed in Fig. 3.13(a). The islands have a thickness between 4 ML and 12 ML while between them we found one or two monolayers grown in the step flow mode. Surprisingly the empty-state peak is present in the spectra above the first and second pseudomorphic monolayer but it does not appear in the dI/dV spectra which were measured above the 3D-islands. In contrast, above the islands we measured a peak at $U_{\text{gap}} = -0.5$ V (occupied states). This occupied-state peak corresponds nicely with photoemission data from bulk Fe(110) [9] and from Fe/W(110) samples with $\Theta \geq 3$ ML [1].

We now turn to the question about the nature of the empty-state peak on mono- and bilayers of Fe on W(110). Therefore we prepared nanometer-scale wedges of Fe on W(110) which naturally are formed by moderate post-annealing. The topography of such a sample is shown in Fig. 3.14(a). For clarity the local coverage is indicated.

On any wedge we can observe simultaneously the forthcoming stages of growth of Fe on W(110) [8], i.e. pseudomorphic growth in the first and partially in the second monolayer, non-periodic and periodic dislocation lines in the second and third monolayer, respectively, and the periodic dislocation network from the fourth monolayer on.

On this sample we measured simultaneously the topography and the spatially resolved differential conductivity dI/dV at different gap voltages. In Figure 3.14(b) and (c) maps of dI/dV at a gap voltage $U_{gap} = +0.4$ V and $U_{gap} = -0.4$ V are presented, which correspond to the empty-state and occupied-state peak positions as seen in Fig. 3.13(b), respectively. In accordance with that data the dI/dV signal at $U_{gap} = +0.4$ V is higher above the second monolayer than above the fourth monolayer while the opposite is true at $U_{gap} = -0.4$ V [Fig. 3.14(b)]. Obviously the electronic structure changes on a narrow lateral scale. The full width of ≈ 15 Å of the dislocation lines is the same for both, topographic and spectroscopic data. However, the most important observation is that the behaviour of the dI/dV signal at $U_{gap} = 0.4$ V is almost the same for the dislocation lines in the second monolayer and for locations where $\Theta \geq 4$ ML [Fig. 3.14(b),(c)]. This means that the empty-state peak disappears wherever the Fe film begins to relax. Thus we conclude, that the origin of the empty-state peak as seen by STS in the first two monolayers is stress-induced due to the relative large lattice mismatch of 9.4 %. Our experimental results are in agreement with earlier band structure calculations for Fe on W(110) [3].

In summary, we have observed directly in real space a stress-induced change of electronic structure in heteroepitaxially grown thin films by STS. While an empty-state peak in the differential conductivity was found above pseudomorphically grown Fe films on W(110) for $\Theta \leq 2$ ML this peak disappears wherever the Fe film begins to relax ($\Theta \geq 2$ ML).

References

- [1] R. Kurzawa, K.-P. Kämper, W. Schmitt, and G. Güntherodt, *Solid State Commun.* **60**, 777 (1986).
- [2] M. Przybylski and U. Gradmann, *Phys. Rev. Lett.* **59**, 1152 (1987).
- [3] S. C. Hong, A. J. Freeman and C. L. Fu, *Phys. Rev. B* **38**, 12156 (1988).
- [4] W. Weber et al., *Phys. Rev. Lett.* **65**, 2058 (1990).
- [5] H. J. Elmers and U. Gradmann, *Appl. Phys. A* **51**, 255 (1990).
- [6] H. J. Elmers et al., *Phys. Rev. Lett.* **73**, 898 (1994).
- [7] C. H. Back, C. Würsch, D. Kerkmann, and D. Pescia, *Z. Phys. B* **96**, 1 (1994).
- [8] H. Bethge, *et al*, *Surf. Sci.* **331-333**, 878 (1995).
- [9] H. J. Elmers et al., *Phys. Rev. Lett.* **75**, 2031 (1995).
- [10] U. Gradmann and G. Waller, *Surf. Sci.* **116**, 539 (1982).
- [11] M. Bode, R. Pascal, and R. Wiesendanger, submitted for publication.

3.3 Scanning Force Microscopy

3.3.1 Growth of C_{60} thin films on GeS(001) studied by scanning force microscopy

U. D. Schwarz, W. Allers, and G. Gensterblum

During recent years, solid C_{60} attracted considerable interest in solid state physics due to the spherical shape of the C_{60} molecules [1] and the extraordinary properties of the bulk material. With the invention of a method for the production of macroscopic quantities of C_{60} [2], it has become possible to investigate the structural, vibrational, frictional, and electronic properties of this new form of carbon. For detailed studies of the solid state properties of C_{60} , the availability of millimeter-sized C_{60} single crystals and high-quality single-crystalline thin films is mandatory. In addition, the growth of C_{60} single crystals and thin films is of fundamental interest, because the individual C_{60} molecules are bound only by the weak van der Waals interaction similar to noble-gas crystals and can adequately be approximated by a hard-sphere model. Therefore, the growth of thin films has been extensively studied.

On most substrates, however, the C_{60} thin films were found to grow irregularly or in the Volmer-Weber growth mode (island growth). A more detailed discussion about the growth mechanisms on several different substrates can be found in Ref. [3].

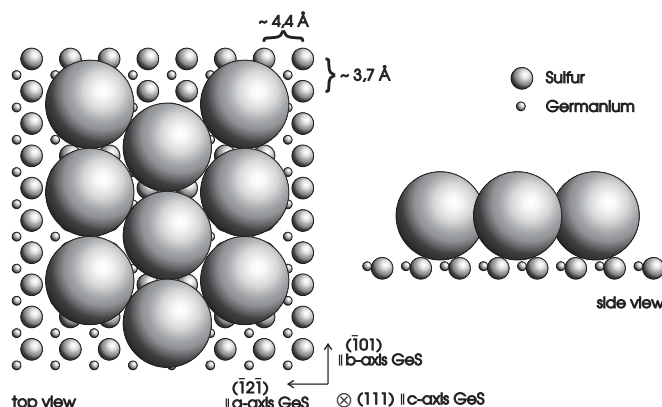


Figure 3.15: Structural model for C_{60} molecules on GeS(001). Due to the anisotropy of the a and b axis of the GeS crystal and the different radii of the sulfur and the germanium ions, parallel rows in b direction with 4.4 \AA distance are formed on the GeS(001) surface. This is nearly half of the interlayer distance of two $\{111\}$ layers in the C_{60} bulk crystal. If every second row is filled, the nearest-neighbor distance of two C_{60} molecules fits well to the 10.02 \AA bulk value. Therefore, large grains with low internal stress can be formed.

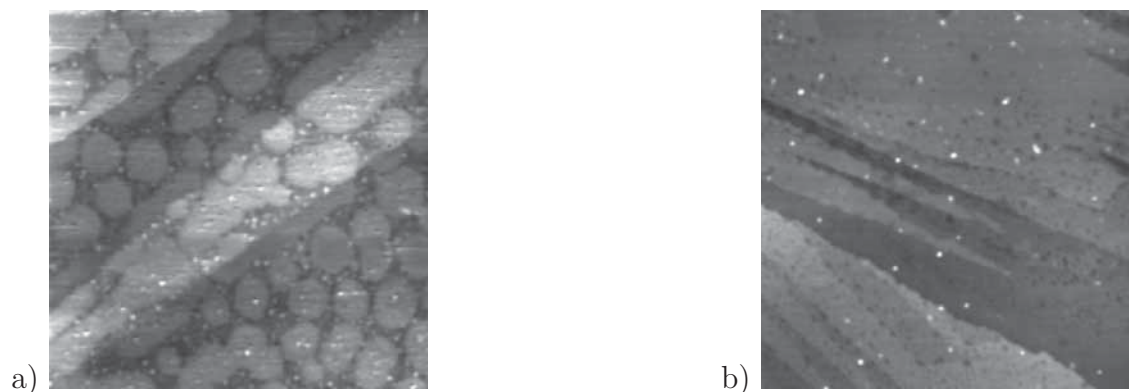


Figure 3.16: (a) Force micrograph of a 0.7-ML film. The scanned area was $9.3 \times 9.3 \mu\text{m}^2$. The observed islands are 1 nm high, corresponding to 1-ML C_{60} . The average diameter of an island is around $1 \mu\text{m}$. Several islands already started to coalesce, but no second layer growth was observed on the whole sample. (b) Large-scale scan ($12.5 \times 12.5 \mu\text{m}^2$) of a 0.95-ML film. Small holes are observed. Closer examination of the holes showed that these holes are 1 nm deep and flat at the bottom. Lateral force images (not shown here) exhibit a different friction at the bottom of the holes compared with the surface of the film. This proves that the surface is really covered by a nearly continuous, 1-ML thick film of C_{60} molecules. The step structure is induced by the cleavage steps of the underlying substrate.

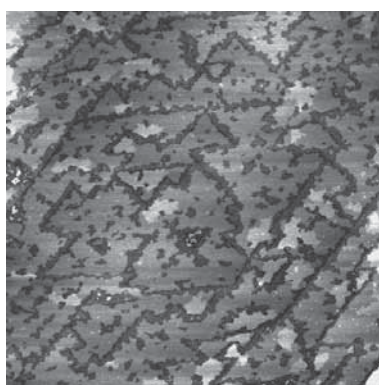


Figure 3.17: Force micrograph of a sample with about 11 ML coverage. The scanned area is $3.6 \times 3.6 \mu\text{m}^2$. The triangular-shaped islands, reflecting the six-fold symmetry of the $\text{C}_{60}\{111\}$ surface, are separated by grooves of 1 ML depth and 50-140 nm width. A mechanism which could explain the observed surface structure is proposed in Fig. 3.18.

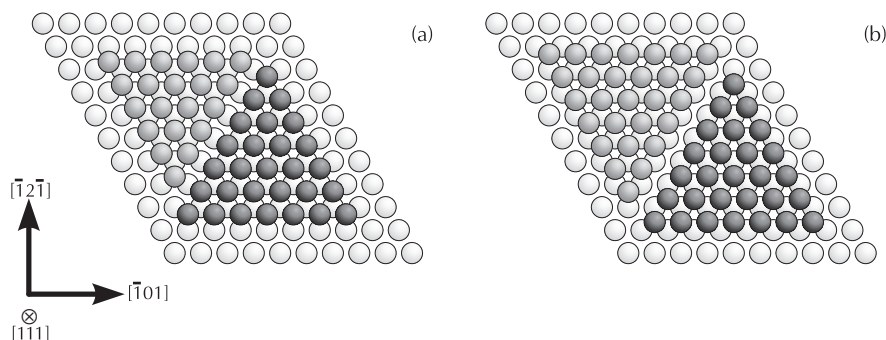


Figure 3.18: A possible mechanism which could explain the observed surface structure of the 11-ML film shown in Fig. 3.17. (a) Triangular islands of different type, bound by steps which are part of small $\{100\}$ microfacets. Different stacking of the C_{60} molecules on the first layer gives rise to the occurrence of a domain boundary. (b) is similar to (a), but with islands bound by $\{111\}$ microfacets. To minimize the surface energy, islands belonging to the same type of domain like to coalesce. On the other hand, the occurrence of grain boundaries is energetically unfavorable. A reduction of the boundary energy might be realised by a reduction of the distance between the individual molecules at the boundary, inducing a stress in the lattice close to the domain boundary. This could explain why areas between different type of domains are filled with C_{60} molecules at a later stage of the growth process.

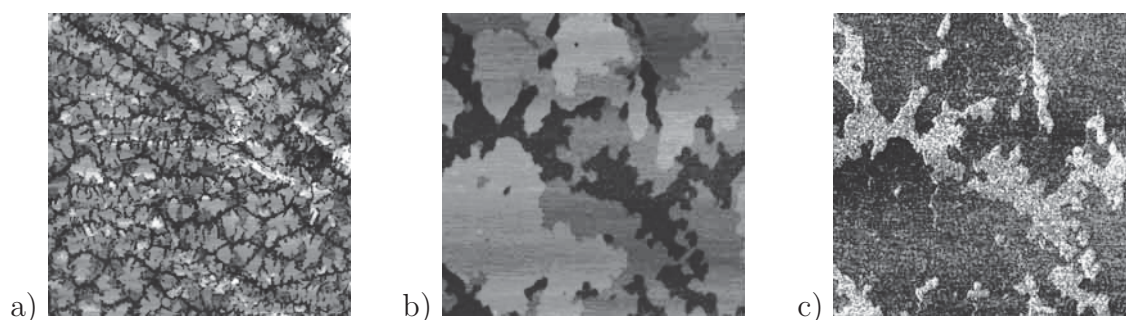


Figure 3.19: Large-scale scan (a; $10 \times 10 \mu\text{m}^2$) and higher magnification image (b; $1.5 \times 1.5 \mu\text{m}^2$) of a film with 1.2 ML nominal coverage. The individual islands have about the same diameter as the islands in Fig. 3.16a, but exhibit dendritic shape. Second and even third monolayer growth starts before the first monolayer has been completed. The individual monolayers are well resolved. (c) Lateral force map of the surface area displayed in (b). The clear contrast allows an easy distinction between substrate and C_{60} layers (see also Sect. 3.4.2).

One of the rare substrates where layer-by-layer growth of single-crystalline films has been reported is GeS(001) [3-5]. The structural model for C₆₀ molecules on GeS(001) is depicted in Fig. 3.15.

In this work, the epitaxial growth of C₆₀ thin films sublimed onto GeS(001) substrates under ultrahigh-vacuum conditions was investigated in the range of 0.7-11 monolayers coverage by scanning force microscopy in air. The growth process follows basically a layer-by-layer mechanism if evaporated in the narrow temperature range from 180-200 °C, but was found to be very sensitive to even small changes in temperature. At substrate temperatures above 200 °C, the second and higher layers are not stable. For temperatures close to 200 °C, our studies indicate pure layer-by-layer type growth (examples for low coverage are given in Fig. 3.16). Somewhat lower substrate temperatures lead to the formation of two different types of triangular-shaped islands (see Fig. 3.17) which originate from a different stacking of the molecules beginning with the second layer (cf. Fig. 3.18). Triangular islands belonging to the same type like to coalesce, whereas islands of different type are separated by grooves. At substrate temperatures close to 180 °C during evaporation, dendritic islands are formed due to the limited mobility of the C₆₀ molecules at this temperature (Fig. 3.19). Furthermore, the growth mode changes to a nonideal layer-by-layer growth where the second and even higher layers start to grow before the first layer has been completed. This behavior can well be explained by a two-dimensional diffusion-limited growth mechanism [5]. Finally, substrate temperatures significantly lower than 180 °C result in films without long-range order. A detailed description of the present growth study can be found in Ref. [5].

References

- [1] H. W. Kroto, J. R. Heath, S. C. O'Brian, R. F. Curl, and R. E. Smalley, *Nature* **318**, 162 (1985).
- [2] W. Krätschmer, L. D. Lamb, K. Fostiropoulos, and D. R. Huffman, *Nature* **347**, 354 (1990).
- [3] G. Gensterblum, K. Hevesi, B.-Y. Han, L.-M. Yu, J.-J. Pireaux, P. A. Thiry, R. Caudano, A.-A. Lucas, D. Bernaerts, S. Amelinckx, G. Van Tendeloo, G. Bendele, T. Buslaps, R. L. Johnson, M. Foss, R. Feidenhans'l, and G. Le Lay, *Phys. Rev. B* **50**, 11981 (1994).
- [4] W. Allers, U. D. Schwarz, G. Gensterblum, and R. Wiesendanger, *Appl. Phys. A* **59**, 11 (1994).
- [5] U. D. Schwarz, W. Allers, G. Gensterblum, J.-J. Pireaux, and R. Wiesendanger, *Phys. Rev. B* **52**, 5967 (1995).

3.3.2 Study of growth stages of $\text{YBa}_2\text{Cu}_3\text{O}_{7-x}$ thin films and YSZ buffer layers on silicon substrates

M. Löhndorf and F. Goerke

The preparation of high-quality thin films of high- T_c superconductors on semiconductor substrates is important in view of potential applications of high- T_c superconductors in microelectronic devices. The film growth has to be optimized with respect to minimal surface roughness, which is required to obtain well-defined interfaces, as well as with respect to electrical properties, e.g. high transition temperature and high critical current density. Scanning probe microscopy has been applied to study various growth stages of YSZ (yttria-stabilized zirconia) buffer layers on silicon and of $\text{YBa}_2\text{Cu}_3\text{O}_{7-x}$ thin films on YSZ/Si. In contrast to the preparation of epitaxially grown $\text{YBa}_2\text{Cu}_3\text{O}_{7-x}$ films on $\text{SrTiO}_3(100)$, $\text{MgO}(100)$ or $\text{LaAlO}_3(100)$ substrates, epitaxial growth of $\text{YBa}_2\text{Cu}_3\text{O}_{7-x}$ films on silicon substrates requires the presence of a buffer layer due to the large lattice mismatch, chemical reactivity and different thermal expansion coefficients between silicon and $\text{YBa}_2\text{Cu}_3\text{O}_{7-x}$. The growth of these buffer layers has to be optimized as well in order to reach optimal properties of the $\text{YBa}_2\text{Cu}_3\text{O}_{7-x}$ thin films. The YSZ buffer layer solves the problem of thermal expansion mismatch of silicon and superconducting copper oxides. In addition, YSZ is chemically inert both with the silicon substrate and the $\text{YBa}_2\text{Cu}_3\text{O}_{7-x}$ top layer and acts as a diffusion barrier for silicon.

The YSZ buffer layers as well as the $\text{YBa}_2\text{Cu}_3\text{O}_{7-x}$ films were grown by pulsed laser deposition. The detailed process has been described elsewhere [1,2]. The natural oxide of the (100) silicon substrates was not removed before the deposition process, but the substrates were rinsed in hot acetone and dried in nitrogen gas flow. The growth rates were 3 \AA/s (corresponding to $0.6 \text{ \AA/laser pulse}$) for YSZ on silicon and 2 \AA/s (corresponding to $2 \text{ \AA/laser pulse}$) for $\text{YBa}_2\text{Cu}_3\text{O}_{7-x}$ on YSZ/Si. After a regulated cool-down process [3] the films were immediately transferred to the scanning

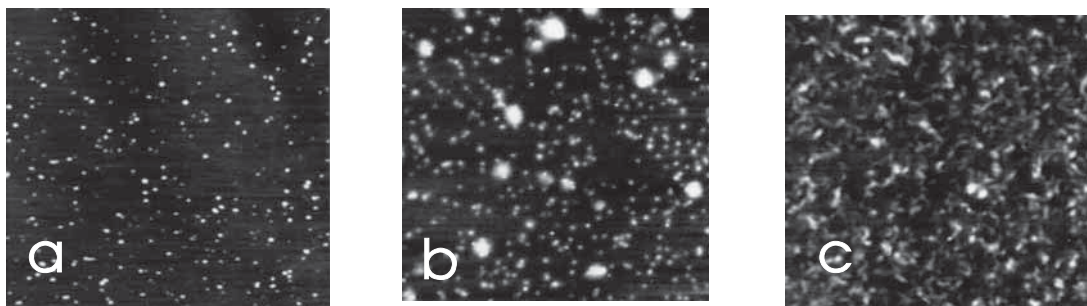


Figure 3.20: Topographic images (scan size: $5 \mu\text{m} \times 5 \mu\text{m}$) of YSZ layer with different thicknesses: **a** 5 nm, **b** 30 nm and **c** 75 nm.

probe microscope. Atomic force microscope (AFM) and scanning tunneling microscope (STM) images were obtained under ambient conditions with a commercially available instrument [4].

The various stages of growth of the thin films have been studied by preparing a series of samples with different deposition time. Upon the deposition of YSZ onto (100) silicon with a nominal thickness of about 0.6 nm the surface remains smooth. At a nominal YSZ film thickness of 5 nm, small particles with a typical diameter of 30 nm, and a height of 3-5 nm are observed on the smooth film (Fig. 3.20 a). At present, the chemical composition of these particles is not clear. The number of these particles increases as the film thickness is increased to 10 nm, whereas their size remains almost constant. At a nominal film thickness of 30 nm some of these particles were found to have grown laterally while the surface of the YSZ film between these particles still appears remarkably smooth (Fig.3.20 b). At a YSZ film thickness of 75 nm, individual particles, as observed before, can no longer be distinguished (Fig.3.20 c). The overall surface roughness has been even decreased leading to a rms-value of only 0.5 nm for a surface area of $5 \times 5 \mu\text{m}^2$. The YSZ film remains to be smooth even for a film thickness

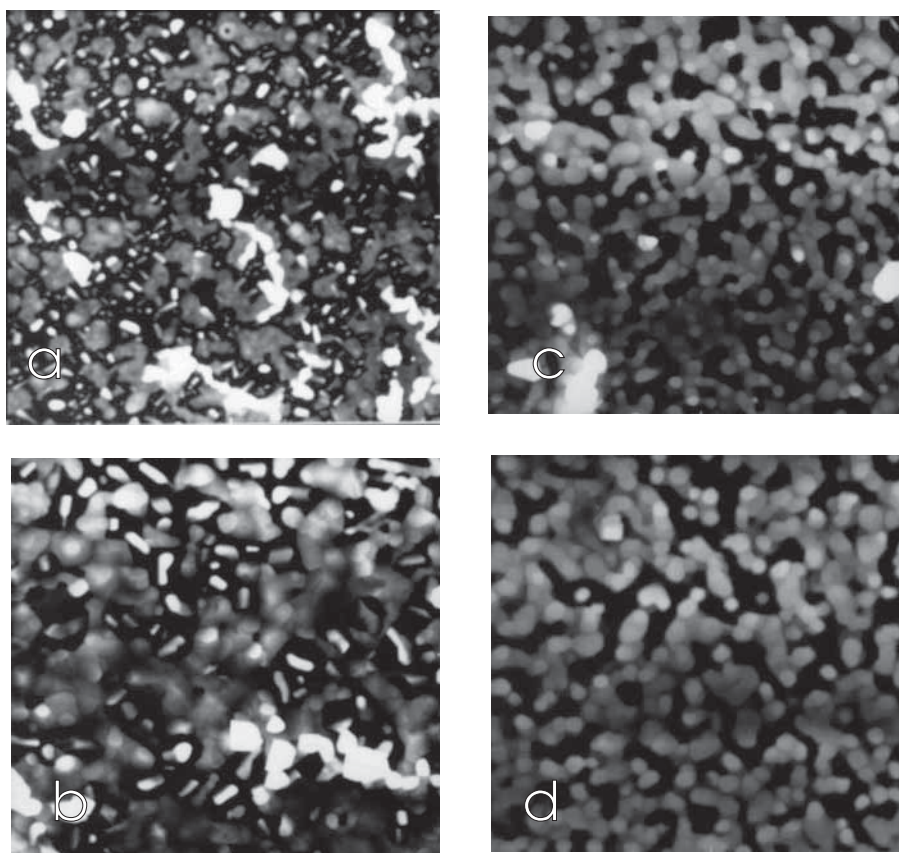


Figure 3.21: Topographic images (scan size: $5 \mu\text{m} \times 5 \mu\text{m}$) of $\text{YBa}_2\text{Cu}_3\text{O}_{7-x}$ layer with different thicknesses: **a** 8 nm, **b** 15 nm, **c** 30 nm and **d** 120 nm.

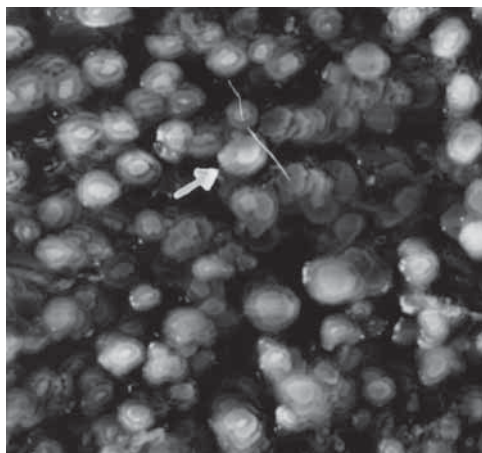


Figure 3.22: STM image of $\text{YBa}_2\text{Cu}_3\text{O}_{7-x}$ layer with thickness of 120 nm. The arrow indicates a screw dislocation (scan size: $2 \mu\text{m} \times 2 \mu\text{m}$).

of 150 nm.

To study the various growth stages of $\text{YBa}_2\text{Cu}_3\text{O}_{7-x}$ thin films on YSZ/Si substrates, we have used a YSZ film thickness of 75 nm because at this thickness no individual particles appear as discussed above. Upon the deposition of nominally 1 nm $\text{YBa}_2\text{Cu}_3\text{O}_{7-x}$, the number of nuclei is found to increase, while the initially formed nuclei have grown laterally to form islands. This behaviour is continued to be observed for a film thickness of up to 4 nm, whereas at 8 nm film thickness, the larger islands start to coalesce (Fig. 3.21 a). At 15 nm thickness the $\text{YBa}_2\text{Cu}_3\text{O}_{7-x}$ film is almost continuous and the initial stages of growth hill formation can be observed (Fig. 3.21 b). Further deposition of $\text{YBa}_2\text{Cu}_3\text{O}_{7-x}$ leads to non-ideal layer-by-layer growth characterized by the nucleation of small islands on non-closed base layers, causing the formation of growth hills separated by voids of various sizes (Fig. 3.21 c and d).

A typical STM image is presented in Fig. 3.22 showing the growth hill morphology, whereas screw dislocations were found only in very rare cases.

Our AFM study of YSZ buffer layers on silicon substrates shows that remarkably smooth YSZ films can be grown by pulsed laser deposition. In Fig. 3.23 the rms-roughness for $5 \mu\text{m}^2$ surface areas is plotted as a function of the YSZ film thickness. The rms-value first increases from 0.2 nm for bare silicon substrates to about 0.3 nm for 10 nm thick YSZ films. For thicker YSZ films the rms-value remains almost constant at the low value of 0.5 nm to 0.6 nm. This experimental observation, which is also made on larger scales, indicates a high degree of structural homogeneity of the YSZ films.

The subsequent growth of $\text{YBa}_2\text{Cu}_3\text{O}_{7-x}$ on YSZ/Si(100) is characterized by the nucleation of islands which continue to grow laterally as well as vertically until they start to coalesce for a $\text{YBa}_2\text{Cu}_3\text{O}_{7-x}$ film thickness of about 8 nm (corresponding to 40 laser pulses). At a $\text{YBa}_2\text{Cu}_3\text{O}_{7-x}$ film thickness of about 30-40 nm an almost closed

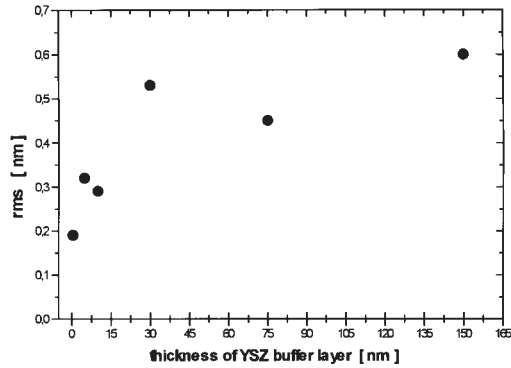


Figure 3.23: rms-roughness for $5 \mu\text{m}^2$ surface areas is plotted as a function of the YSZ film.

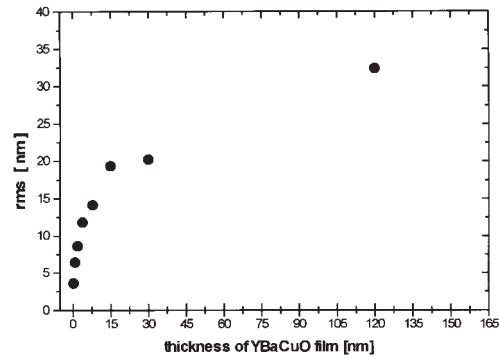


Figure 3.24: rms-roughness plotted as a function of the $\text{YBa}_2\text{Cu}_3\text{O}_{7-x}$ film thickness.

$\text{YBa}_2\text{Cu}_3\text{O}_{7-x}$ layer starts to form with islands nucleated on top of this layer. The non-ideal layer-by-layer growth leads to the formation of growth hills, rather than to the formation of spirals caused by screw dislocations. The formation of growth hills leads to increasing rms-roughness with increasing film thickness as shown in Fig.3.24. This is undesirable with regard to the formation of well-defined interface or multilayer structures.

It remains to be studied whether $\text{YBa}_2\text{Cu}_3\text{O}_{7-x}$ films being smooth and simultaneously having high critical current densities can be grown on YSZ/Si(100) substrates. For further experimental details see Ref. [5,6]

References

- [1] F. Goerke and M. Schilling, Journal of Alloys and Compounds **195** 219 (1993).
- [2] M. Schilling, F. Goerke and U. Merkt, Thin Solid Films **235** 202 (1993).
- [3] M. Schilling, Ph. D. thesis, University of Hamburg, 1992
- [4] Nanoscope III, Digital Instruments, Santa Barbara (CA).
- [5] F. Goerke, Physica C **245**, 15 (1995).
- [6] M. Löhndorf, F. Goerke, U. Merkt, and R. Wiesendanger, Appl. Phys. A **59**, 57 (1994).

3.3.3 Scanning force microscopy goniometry

A. Schwarz, U. D. Schwarz and H. Bluhm

Scanning force microscopy (SFM) is used to obtain three-dimensional topographical data. From these data in- and out-of-plane angles can be determined. In the latter case, the measurement can suffer from tip artefacts. This report will show under which conditions the apparent out-of-plane angle is identical with the true angle and that Miller indices of small crystallographic planes can be calculated. Further details can be found in [1].

In-plane angles, e.g. the angle between two side faces of a crystal, are correct in SFM images, if the scanner calibration is precise. But even atomically sharp edges are rounded due to the finite tip radius. Out-of-plane angles, e.g. slope angles between a substrate and a crystal, are correct below a critical angle θ_c . If the height of the object, e.g. a crystal, is larger than the tip radius, θ_c is defined only by the opening angle α of the tip:

$$\theta_c = 90^\circ - \frac{1}{2}\alpha \quad (3.8)$$

Otherwise θ_c depends on the object height h and the tip radius R

$$\cos(\theta_c) = 1 - \frac{h}{R}. \quad (3.9)$$

For very small objects, as the crystallites investigated below, sharp tips with small opening angles and tip radii are necessary. Therefore only electron beam deposited (ebd) tips [2], with tip radii between 10 nm and 20 nm and opening angles between 6° and 18° were used [1]. For a typical tip with $R = 15$ nm and $\alpha = 10^\circ$, the critical angle for $h = 10$ nm is found to be $\theta_c = 70.5^\circ$. The critical angle depends on the scan direction even for tips with rotational symmetry if the tip axis is not perpendicular to the surface. To check this, the scan should be repeated under different scan angles.

Small haematite (α -Fe₂O₃) crystallites 5-50 nm high with side faces of 80-300 nm length were grown on the (0001) plane of sapphire (α -Al₂O₃) as follows. One drop of a highly monodisperse iron oxide precursor particle solution (particle diameter around 15 nm) [3] is distributed homogeneously on the substrate and heated for 1 h at 1000°C, well above the crystallization temperature. Both sapphire and haematite have identical crystal structure (R $\bar{3}$ c). Therefore, the crystallites grow epitaxially on the substrate with all axes parallel to each other (see Fig. 3.25).

All observed in-plane angles between two adjacent side faces are 60° and 120° , respectively. The crystallites are either of the rhombohedral type with $\{10\bar{1}l\}$ side faces (corresponding to point symmetry $\bar{3}$) or of hexagonal type with $\{1\bar{1}2l\}$ side faces (corresponding to point symmetry 6/m). To decide which crystallite belongs to which type one can compare the general step direction of the substrate, seen as horizontal

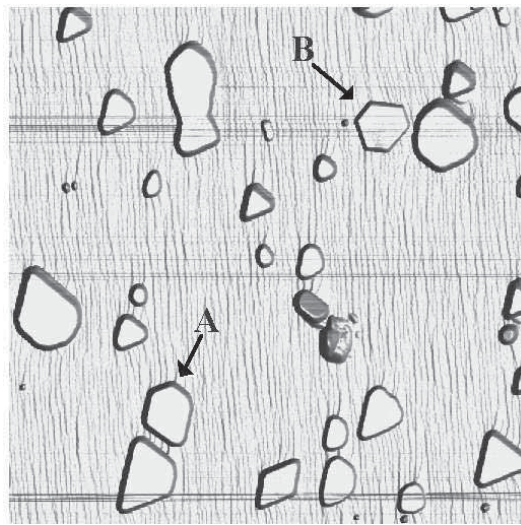


Figure 3.25: Illuminated $2.6 \mu\text{m} \times 2.6 \mu\text{m}$ top-view SFM image of 5-20 nm high haematite crystallites on (0001) sapphire. All crystallites show 60° and 120° in-plane angles only. Crystallite A is of rhombohedral type and B is of hexagonal type.

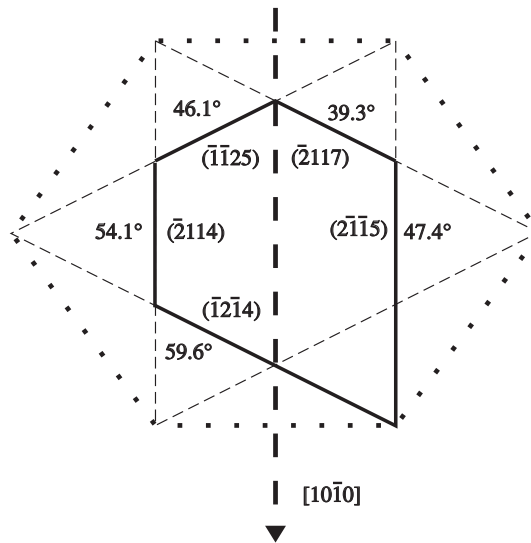


Figure 3.26: Sketch of crystallite A with the measured slope angles and the corresponding Miller indices. The arrow indicates the general step direction of the substrate.

stripes in Fig. 3.25, with the orientation of the crystallite side walls. The sapphire steps are known to be parallel to $[10\bar{1}0]$ [4]. Hence, side faces of hexagonal type crystallites are parallel to the substrate steps or tilted by 60° , while rhombohedral side faces are perpendicular or tilted by 30° . In Fig. 3.25 most of the crystallites are rhombohedral, e.g. the one marked A. An example for hexagonal type side faces is given by crystallite B.

From in-plane angle measurements it was possible to determine the Miller indices h, i and k of the side faces. The last index, l , can be calculated from out-of-plane angle measurements, e.g. the slope angle between the (0001) plane of the substrate and the side face of the crystallite. The angle between two crystal planes ($h_1k_1i_1l_1$) and ($h_2k_2i_2l_2$) in the hexagonal system is given by [5]

$$\cos(\theta_{12}) = \frac{4}{3a^2}[h_1h_2 + k_1k_2 + \frac{1}{2}(h_1k_2 + h_2k_1 + \frac{3}{4}\gamma^{-2}l_1l_2)]d_1d_2 \quad (3.10)$$

with $d_i = \frac{a}{\sqrt{\frac{4}{3}(h_i^2+k_i^2+h_ik_i)+\gamma^{-2}l_i^2}}$ and $\gamma = \frac{a}{c}$ ($a = 0.503$ nm, $c = 1.375$ nm). Since the substrate is cut parallel to the (0001) plane, this simplifies to

$$\cos(\theta_{12}) = \frac{l_2d_2}{c}. \quad (3.11)$$

In Table 3.1, the theoretical slope angle between the (0001) plane and the $\{10\bar{1}l\}$ planes are listed, as calculated from Eq. (3.11). Figure 3.26 shows a sketch of crystallite A with all slope angles and corresponding Miller indices according to Table 3.1. The same can be done for crystallites of hexagonal type. All angles are determined from higher magnification images and are far below the critical angle of the used ebd tip. The side faces of that crystallite are as small as 1600 nm².

Table 3.1: Calculated slope angles between substrate and crystallite side faces according to Eq. 3.11.

$\{10\bar{1}l\}$	$\{10\bar{1}1\}$	$\{10\bar{1}2\}$	$\{10\bar{1}3\}$	$\{10\bar{1}4\}$	$\{10\bar{1}5\}$	$\{10\bar{1}6\}$	$\{10\bar{1}7\}$	$\{10\bar{1}8\}$
slope angle	72.4°	57.7°	46.5°	38.3°	32.3°	27.9°	24.4°	21.7°

References

- [1] A. Schwarz, U. D. Schwarz, H. Bluhm, and R. Wiesendanger, *Surf. Interface Anal.* **23**, 409, (1995).
- [2] K. I. Schiffman, *Nanotechnology* **4**, 163 (1993).
- [3] W. Sager, H. F. Eicke, and W. Sun, *Colloids Surf. A* **79**, 199 (1993).
- [4] D. W. Susnitzky and C. B. Carter, *J. Am. Ceram. Soc.* **69**, C-217 (1986).
- [5] A. G. Jackson, *Handbook of Crystallography*, p. 71, Springer Verlag, New York (1991).

3.3.4 Load dependent topographic and friction studies of individual ion tracks in layered materials by scanning and lateral force microscopy

M.Seider and U.D.Schwarz

Latent nuclear tracks are damaged or amorphous zones, created along paths of moving ions in solids [1]. The shape of the tracks depends of the stopping power. The detailed study of tracks is important in many different fields of science, such as archeology, geochronology, nuclear physics etc., as well as for technological applications, e.g. filters, refining of magneto-optic materials, heavy ion lithography, etc.

Scanning probe microscopy is a useful tool to get information about the local properties of individual latent ion tracks in solids. Scanning force microscopy (SFM)

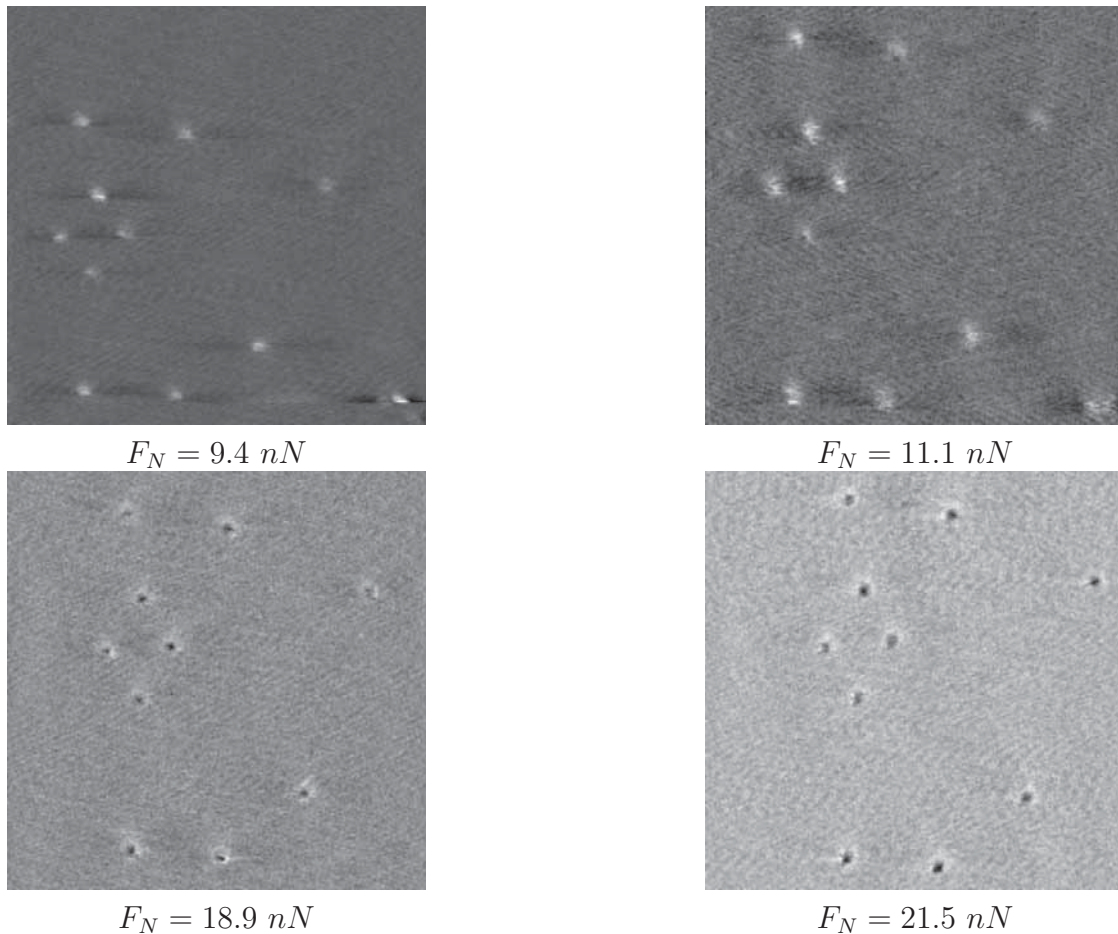


Figure 3.27: Series of four SFM graphs $(300 \text{ nm})^2$ showing a contrast-reversal in the topography as a function of the applied loading force

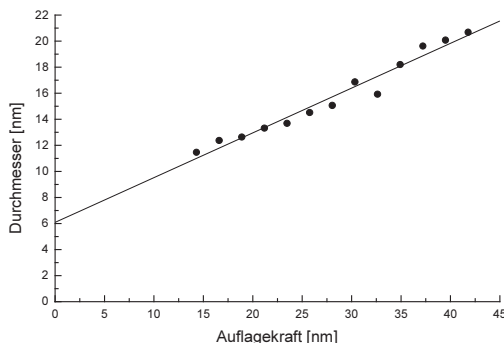


Figure 3.28: Apparent diameter of a latent ion track as a function of the applied loading force

yields information about the topography, mechanical and friction properties of single tracks. In the present study muscovite mica has been irradiated by 500 MeV ^{129}Xe ions. We have found that the apparent diameter of the latent ion tracks and the contrast in topography and lateral force images depends critically on the applied loading force.

In an earlier study it was observed, that the ion tracks are imaged as hillocks or hollows in the topography by SFM depending on the scan direction [2]. Here we have found that at lower loading force the SFM shows only hillocks independent of the scan direction (Fig. 3.27). It is possible that the track formation consists of stressed-induced outgrowth of amorphous material [3]. The average height of an outgrowth is (0.98 ± 0.23) nm.

Likewise it was found that the size of the tracks depends on the applied loading force as can be seen in Fig. 3.28. The apparent diameter appears to decrease nearly linearly with decreasing load. An extrapolation towards zero loading force yields a diameter of (6.0 ± 2.3) nm, which agrees well with the data of small-angle x-ray diffraction. Therefore different results for the diameter, as obtained from SFM and small-angle

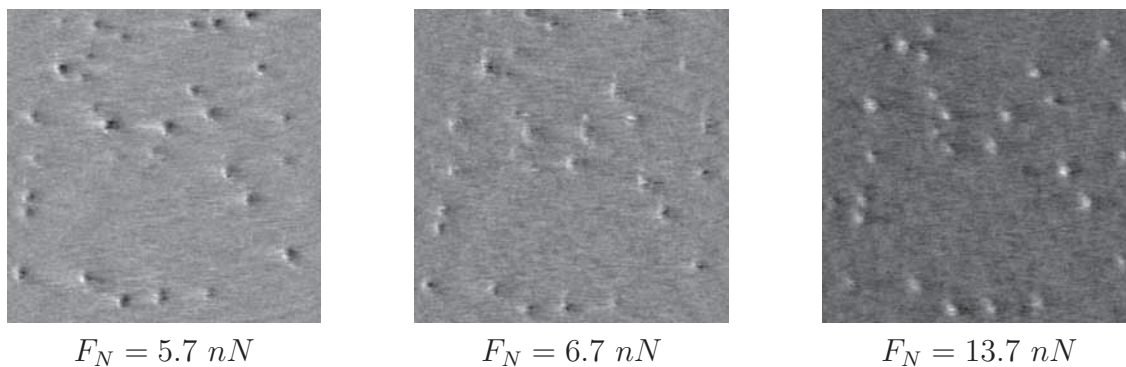


Figure 3.29: Series of lateral force graphs $(500 \text{ nm})^2$ showing a contrast-reversal in the topography as a function of the applied loading force

x-ray diffraction data [4], can be explained by taking the finite load into account.

We also studied the lateral force component as a function of the applied loading force. While in the high-load region the tracks show a higher friction signal compared with the undamaged region (Fig. 3.29), the lowering of the loading force leads to a contrast reversal. It is possible, that the friction force F_R depends on the loading force F_N with a power law [5]:

$$F_R = CF_N^m \quad (3.12)$$

A different value of m for the tracks and the undamaged mica can explain this contrast reversal behaviour [6].

References

- [1] B. E. Fischer, R. Spohr, *Rev.Mod.Phys.* **55**, 903, (1983)
- [2] P. Bauer, C. Giethmann, M. Kraus, T. Marek, J. Burger, G. Kreiselmeyer, G. Saemann-Ischenko, M. Shibowski, *Europhys. Lett.* **23**, 585, (1993)
- [3] P. Bauer, C. Rossel, E. J. Williams, R. Berger, J. Daniel, B. Irmer, M. Kraus, G. Kreiselmeyer, G. Saemann-Ischenko, J. Karpinski, to be published
- [4] V. Chailley, E. Dooryhée, S. Bouffard, S. Balazat, *Nucl.Instr.and Met.in Phys.Res.* **B 91**, 162, (1994)
- [5] U. D. Schwarz, W. Allers, G. Gensterblum, and R. Wiesendanger, *Phys.Rev. B* **52**, (1995)
- [6] M. Seider, U. D. Schwarz, and R. Wiesendanger, submitted for publication.

3.4 Friction Force Microscopy/Spectroscopy

3.4.1 Quantification of friction force microscopy measurements

P. Köster and U. D. Schwarz

Measurements with the lateral force microscope (LFM) [1-3] are often not reproducible if they are obtained with different cantilevers. This has two main reasons. First, the shape of the tip and therefore the load dependence of the actual contact area has an influence on friction forces. Since the tip shape at the actual contact interface can change even during the measurement, absolute reproducible measurements are difficult even within a set of experiments performed with the same cantilever.

The other reason for the frequently observed not satisfying reproducibility of LFM data published by different groups or even obtained with the same instrument might be due to an incorrect analysis and/or due to an underestimation of the unavoidable errors in the gauge of the normal load and friction forces. Due to this uncertainty in the correct analysis of the experimental data, many authors only give relative friction data or publish their results without error calculation. Here, we will briefly discuss how normal and lateral forces in force microscopy have to be calibrated and what the possible errors for lateral force measurements are when using a scanning force microscope based on the beam deflection method. A detailed discussion of these topics will be published in Ref. [4].

Most commercially available force microscopes use the laser beam deflection method for the measurement of the cantilever displacement. A bending ϑ or a torsion β of the cantilever results in a displacement of the beam on the four-segment photodetector. This causes proportional voltage signals

$$U_{ver} \sim \vartheta \Rightarrow U_{ver} = c_{ver} \cdot \vartheta \quad (3.13)$$

and

$$U_{lat} \sim \beta \Rightarrow U_{lat} = c_{lat} \cdot \beta. \quad (3.14)$$

In addition to this, the signal in z -direction is connected with the z displacement of the cantilever by the sensitivity s_{ver}

$$s_{ver} = \frac{U_{ver}}{z} \quad (3.15)$$

which can be determined by force-versus-distance curves. Using the spring constant C_z for a rectangular cantilever with the length L , the width w , the thickness t and Young's modulus E

$$C_z = \frac{Et^3w}{4L^3}, \quad (3.16)$$

we can write for the force F_N acting normal to the surface

$$F_N = \frac{C_z}{s_{ver}} \cdot (U_{ver} - U_{dis}) = B \cdot \Delta U_{ver}. \quad (3.17)$$

Here, the normal force F_N is calibrated to zero where the tip jumps off the surface.

For the absolute calibration of the lateral force F_{lat} , the proportional constant c_{lat} in Eq. (3.14) must be known. In the ideal case c_{lat} and c_{ver} will be identical, leading to $s_{ver} = s_{lat}$. For a cantilever with a rectangular cross section and a large radius of curvature we find

$$c_{ver} = \frac{2L}{3} \cdot s_{lat} \quad (3.18)$$

The absolute value of the lateral force is measured by scanning forward and backward on the same line in order to eliminate any influence from a tilt of the sample. During this scan the lateral voltage signal U_{lat} is recorded. Since the torsion angle changes its sign when the scan direction turns, U_{lat} will change its sign as well. For such a scan cycle (the so-called “friction loop”), the mean difference between trace and retrace is calculated and will be denoted as ΔU_{lat} . Hence, the torsion angle is given by

$$\beta = \frac{\Delta U_{lat}}{2c_{lat}} = \frac{3\Delta U_{lat}}{4Ls_{lat}}. \quad (3.19)$$

It is then possible to calculate the corresponding force for a cantilever with the tip length ℓ

$$F_{lat} = \frac{C_{tor}}{L\ell} \cdot \beta. \quad (3.20)$$

In this equation, C_{tor} is the torsional force constant. For a rectangular cross section with $t \ll w$ and torsional modulus G , C_{tor} is given by

$$C_{tor} = \frac{Gbt^3}{3}. \quad (3.21)$$

Together with Eqs. (3.19) and (3.21), Eq. (3.20) can now be written as

$$F_{lat} = \frac{Gb d^3}{4L^2\ell} \cdot \frac{1}{s_{lat}} \cdot \Delta U_{lat} = A \cdot \Delta U_{lat}. \quad (3.22)$$

The following errors have now to be considered:

Cantilever dimensions: The first error is introduced by uncertainties in the dimensions of the cantilever, namely in the length L , the width w , the thickness t and the tip length ℓ . In our lab, these values are obtained by the individual examination of every cantilever used for friction measurements in the electron microscope.

Position of the laser beam: The angles ϑ and β are measured at the point where the laser beam is reflected from the cantilever backside. It is therefore crucial that the laser beam is reflected exactly above the tip. If we distinguish between the length L of the cantilever from the support to the middle of the tip and the coordinate L^* at which the beam is reflected, Eq. (3.16) and therefore (3.17) will be unaffected. However, in Eq. (3.22), L must be substituted by L^* .

Sensitivities 1: With the assumption that tip and sample are infinitely hard, the sensitivity s_{ver} can be obtained from force-distance curves. In the case of huge adhesive forces, the resulting pull-off force F_{PO} can be so high that the slope in the force-distance curve is not constant due to a non-linear characteristic of the output voltage U_{ver} of the photo-diode if plotted as a function of the displacement Δs in vertical direction. In this case, the slope around the chosen setpoint voltage has to be taken. In most cases, however, the determination of s_{ver} is given by the reading error.

Sensitivities 2: Another effect concerns the assumption that the numerical values of c_{ver} and c_{lat} in Eqs. (3.13) and (3.14) are equal. In the ideal case of a circular shaped laser beam this is true. Most laser diodes have though – due to their internal structure – beams with strong elliptical, often nearly rectangular shape as output. This leads to different dependencies of the output voltage from the photo-diode on the position of the beam on the active photo-diode area, and therefore to different values of c_{ver} and c_{lat} .

Oscillations of the cantilever: It is well-known that if the integral and/or the proportional gain of the feedback loop are set to high values, the feedback loop and therefore the scanner will start to oscillate. Normally, this oscillation can easily be observed in the recorded output signals of the four-segment photo diode (“deflection signal”) or the feedback loop (“height signal”), and it is a well-established method to adjust the gains of the feedback loop to values just below this oscillation threshold. However, it can happen that an oscillation with an amplitude smaller than the noise level arises. This oscillation can already reduce the measured frictional forces significantly without showing up in the deflection or in the height signal if they are analysed by an oscilloscope.

Determination of U_{dis} : One way for the determination of U_{dis} is by means of force-distance curves. U_{dis} is the vertical voltage signal at the lowest point of the hysteresis loop. Normally, this value fluctuates about some tenths of a volt and sometimes U_{dis} even drifts systematically (e.g., due to thermal drift). Therefore, the measurement of a lateral force versus normal force curve must be interrupted several times to check the actual value of U_{dis} .

In addition to this it can happen that this value of U_{dis} is lower than the value which is obtained during the scan. This leads to a nonphysical negative load. To avoid this we used the vertical voltage at which the tip disengages during the

scanning process. After five friction measurements at the same normal load we reduced the setpoint and therefore the normal load until tip and sample separate. The value of the setpoint when this happens is used for U_{dis} .

Statistical errors: We observed two kinds of statistical errors. The first one affects the fluctuation for friction measurements at the same normal load which are performed directly after each other. Measurements on highly oriented pyrolytic graphite (HOPG), which was chosen due to its very low friction and consequently high statistical fluctuations, showed that the different measured values for the friction forces are approximately gaussian distributed. The second error is related to measurements for different normal load. For these measurements, the statistical error is a priori unknown since the exact friction versus load dependence is unknown. Nevertheless, the value for χ^2 can be a clue for this error.

References

- [1] C. M. Mate, G. M. McClelland, R. Erlandsson, and S. Chiang, Phys. Rev. Lett. **59**, 1942 (1987).
- [2] O. Marti, J. Colchero, and J. Mlynek, Nanotechnology **1**, 141 (1990).
- [3] G. Meyer and N. M. Amer, Appl. Phys. Lett. **57**, 2089 (1990).
- [4] P. Köster, U. D. Schwarz, and R. Wiesendanger, manuscript in preparation.

3.4.2 Low-load friction behavior of C_{60} thin films

W. Allers, U. D. Schwarz, and G. Gensterblum

The discovery of a new method to produce macroscopic amounts of C_{60} [1] initiated widespread research activities focussing on its interesting physical properties and possible applications. In particular there have been speculations about a unique lubricating quality of C_{60} thin films, due to the spherical shape of the molecule.

To investigate this experimentally, C_{60} thin films were studied by scanning and friction force microscopy (SFFM) [2, 3] using a commercially available instrument under ambient conditions which permits spatially resolved measurements of both normal and friction forces simultaneously down to the nanometer scale. The C_{60} films were sublimated in UHV onto in-situ cleaved GeS(001) surfaces and subsequently checked by LEED. The growth of films prepared in this manner has already been investigated thoroughly and proven to form epitaxial layers on GeS(001) [4, 5].

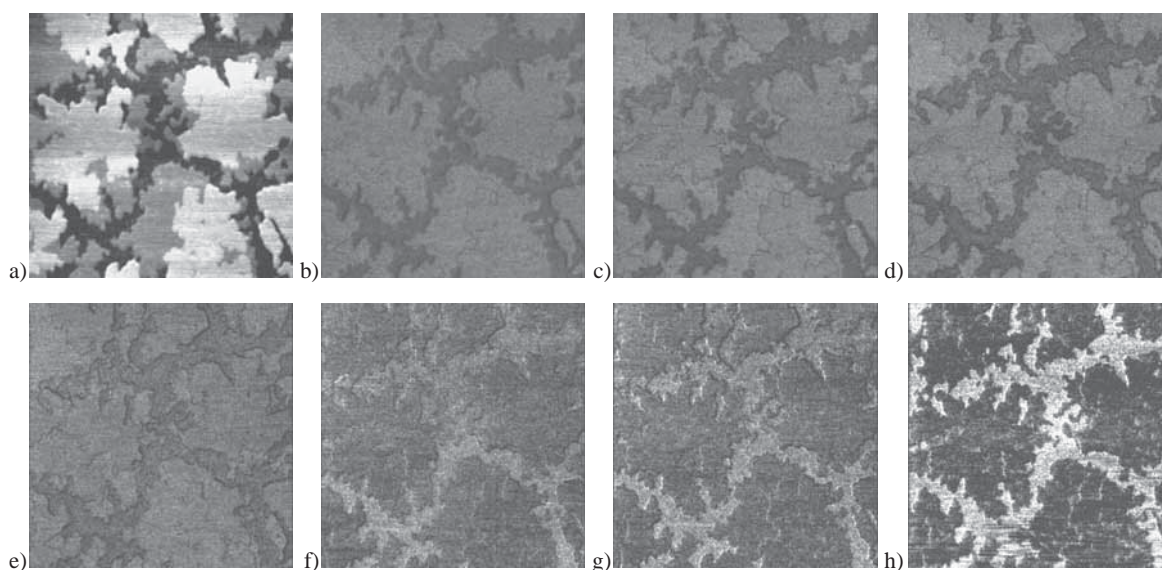


Figure 3.30: **a** Topographic image of an 1.2 ML thin film C_{60} on GeS(001), scan size: $2 \mu\text{m} \times 2 \mu\text{m}$; **b-h** Friction force maps for the same area at loading forces of 1.3 nN **b**, 2.6 nN **c**, 6.7 nN **d**, 10 nN **e**, 15 nN **f**, 20 nN **g**, 30 nN **h**

The results presented here are based on data acquired on a sample with 1.2 monolayers nominal film thickness. Due to a non-ideal layer-by-layer growth [5, 6] only 70 % of the substrate surface was covered by C_{60} islands. For the SFFM investigations a rectangular silicon cantilever with 0.045 N/m spring constant was used; scan speeds were approximately $2 \mu\text{m}/\text{sec}$. The friction force F_f was measured for a series of loads F_n applied to the area of contact of tip and surface. In this context F_n represents not merely the normal force applied externally through the cantilever, but rather the sum

of all normal forces, including capillary and van der Waals forces that are responsible for the repulsive interaction between the foremost atoms of the tip and the sample.

Figure 3.30(a) shows the surface topography of a $2 \mu\text{m} \times 2 \mu\text{m}$ large area, revealing several dendritic islands of up to two monolayers height. The corresponding friction force maps (b–h) were obtained for normal forces F_n ranging from 1.3 nN up to 30 nN. Here, dark areas mean low and bright areas high lateral force. Images 3.30(b–d), obtained with loads below 10 nN, show lower lateral forces on the substrate than on the islands. At approximately 10 nN [Fig. 3.30(e)] this contrast vanishes and flips as the load rises (f–h).

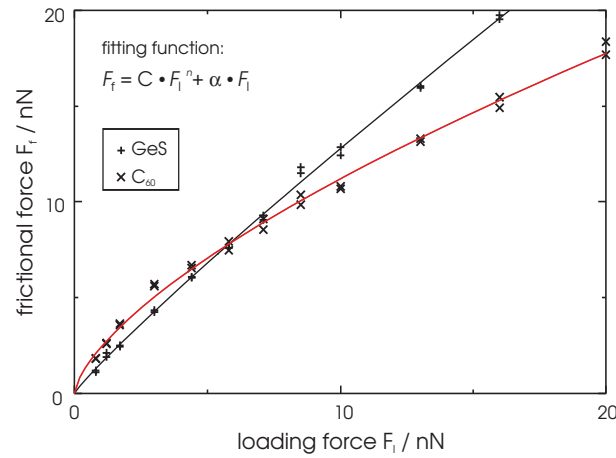


Figure 3.31: Plot of $F_f(F_l)$ for both GeS and C_{60} including fit curves for $F_f = CF_l^n + \alpha F_l$

The quantitative dependence of the frictional force on the applied load for the GeS surface and C_{60} islands is shown in Figure 3.31. The behavior of the frictional force on the C_{60} islands is markedly different compared to the behavior on the GeS substrate. As a result the two data sets exhibit a crossing point, which corresponds to the contrast reversal in the spatially resolved measurements. While the contrast reversal was observed in all measurements, the exact value of the crossing point varied between different measurement series.

According to Amontons's classical law of friction, F_f is expected to be proportional to F_n : $F_f = \mu \times F_n$ (μ = friction coefficient). However, a more recent theory predicts that for adhesive junctions F_f is proportional to the area of contact A : $F_f = S \times A$, where S is the shear stress. A frequently used model approximates the dependence of S on the pressure $p = F_n/A$ as follows: $S = S_0 + \alpha \times p$; α and the offset S_0 are empirical constants. This leads to

$$F_f = S_0 A + \alpha F_n. \quad (3.23)$$

For $S_0 = 0 \text{ N/m}^2$, (3.23) obviously results in the classical law with $\alpha = \mu$.

In all other cases, the friction force will also depend on the contact area A , which itself may be a non-linear function of F_n . To describe a friction coefficient decreasing

with increasing load, A may be written in terms of $A \propto F_n^m$, $0 < m < 1$. Hence, for a finite value of S_0 relation (3.23) results in

$$F_f = CF_n^m + \alpha F_n. \quad (3.24)$$

Using (3.24) to fit the data revealed a value close to 1 for m on the GeS(001) surface, corresponding to an almost linear relation. The frictional behavior can therefore also quite appropriately be described by $C = 0$ and $\alpha = 1.24 \pm 0.01$. For the C₆₀ islands, however, α was close to zero and the term $C \times F_n^m$ clearly dominated over the linear component. A $F_f \propto F_n^{2/3}$ curve was found to match the data excellently ($m = 0.665 \pm 0.012$); a linear fit would fail completely. This $F_n^{2/3}$ -dependence of the contact area A can be interpreted in terms of a generalized Hertzian theory [7] and is discussed in detail in Refs. [8] and [9].

References

- [1] W. Krätschmer, L. D. Lamb, K. Fostiropoulos, and D. R. Huffman, *Nature* **347**, 354 (1990).
- [2] G. Binnig, C. F. Quate, and C. Gerber, *Phys. Rev. Lett.* **56**, 930 (1986).
- [3] C. M. Mate, G. M. McClelland, R. Erlandson, and S. Chiang, *Phys. Rev. Lett.* **59**, 1942 (1987).
- [4] G. Gensterblum, K. Hevesi, B.-Y. Han, L.-M. Yu, J.-J. Pireaux, P. A. Thiry, R. Caudano, A.-A. Lucas, D. Bernaerts, S. Amelinckx, G. Van Tendeloo, G. Bendele, T. Buslaps, R. L. Johnson, M. Foss, R. Feidenhans'l, and G. Le Lay, *Phys. Rev. B* **50**, 11981 (1994).
- [5] U. D. Schwarz, W. Allers, G. Gensterblum, J.-J. Pireaux, and R. Wiesendanger, *Phys. Rev. B* **52**, 5967 (1995).
- [6] W. Allers, U. D. Schwarz, G. Gensterblum, and R. Wiesendanger, *Appl. Phys. A* **59**, 11 (1994).
- [7] A. Fogden, L. R. White, *J. Colloid Interface Sci.* **138**, 414 (1990).
- [8] U. D. Schwarz, W. Allers, G. Gensterblum, and R. Wiesendanger, *Phys. Rev. B* **52**, 15. Nov. 1995 (in press).
- [9] U. D. Schwarz, H. Bluhm, H. Hölscher, W. Allers, and R. Wiesendanger, in: *The Physics of Sliding Friction*, ed. by B. N. J. Persson, NATO ASI Series, Kluwer, Dordrecht, 1996 (in press).

3.4.3 Atomic friction in a nonsymmetric potential

H. Hölscher and U. D. Schwarz

In everyday life it can often be seen that friction depends on the sliding direction. This phenomenon can be met rubbing by hand over certain pieces of clothes. Another example is the one of a saw; there, it depends on the direction how strong you have to pull or to push. The same phenomenon can be met on the atomic scale, too. Profiling a surface with a nonsymmetric crystal structure using a FFM, the friction force can show a dependence on the scan direction.

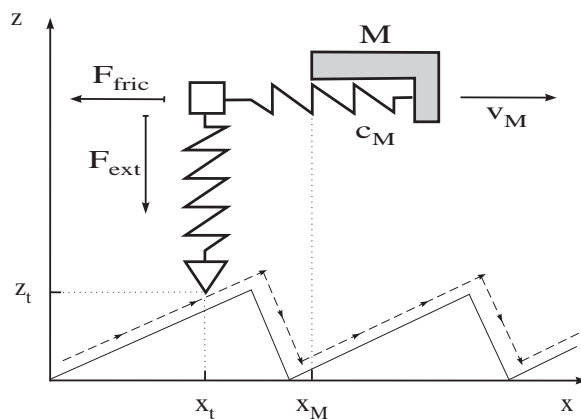


Figure 3.32: A simplified model of a FFM. The bending in y -direction is neglected. x_t represents the position of the tip and x_M the position of the FFM body M which is moved with the velocity v_M in x -direction. If $x_t = x_M$, the horizontal spring is in equilibrium position. $V(x_t)$ is the effective potential between tip and surface. With c_M as spring constant the *momentary friction force* F_{fric} necessary to move the FFM body M in x -direction is given by $F_{fric} = c_M(x_M - x_t)$.

To calculate this atomic friction we use the simple but very instructive Tománek-Zhong-Thomas (TZT) model [1] which considers a simplified version of a FFM (Fig. 3.32). In this model one has to solve the equation

$$c_M(x_t - x_M) = -\frac{\partial V(x_t)}{\partial x_t} \quad (3.25)$$

to determine the path of the tip of the FFM. With this solution the *momentary friction force* F_{fric} – necessary to move the tip over the surface – can be calculated from

$$F_{fric}(x_M) = c_M(x_M - x_t(x_M)). \quad (3.26)$$

Unfortunately, with most potentials, it is not possible to calculate the frictional forces analytically and numerical calculations have to be made. Only for certain simple

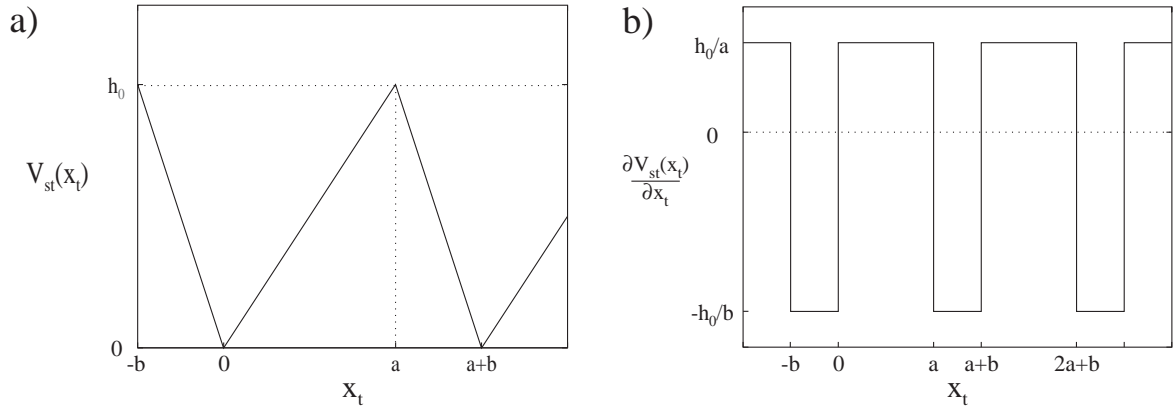


Figure 3.33: a) A saw-tooth potential $V_{st}(x_t)$. b) First derivative of $V_{st}(x_t)$ resulting in a step function.

potentials $V(x_t)$, simple analytical solutions can be derived. Let us therefore consider a *saw-tooth* potential $V_{st}(x_t)$ with a height h_0 and widths a and b [see Fig. 3.33a for the exact definition of $V_{st}(x_t)$]. This potential is very close to the example of a saw mentioned above and so we expect different frictional forces between forward and backward scan if $V_{st}(x_t)$ is nonsymmetric, i.e. $a \neq b$. Especially in the limit $b \rightarrow 0$ it seems clear that F_{fric} in backward direction becomes very high. Mathematically, the advantage of this simplification of a nonsymmetric potential is the comfortable form of the first derivative which is just a simple step function.

Depending on the spring constant c_M different types of paths $x_t(x_M)$ are possible. We restrict ourselves to a very soft spring [$c_M \leq h_0(\frac{1}{a^2} + \frac{1}{ab})$ and $c_M \leq h_0(\frac{1}{b^2} + \frac{1}{ab})$] and determine for this case the difference between the *average friction forces* of the

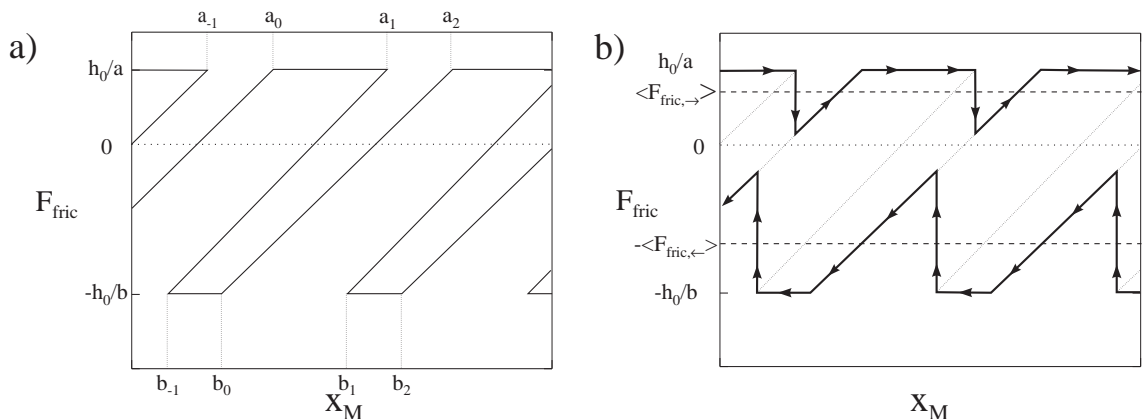


Figure 3.34: a) The solution of Eq. 3.25 for a saw-tooth potential introduced in Eq. 3.26. b) F_{fric} (solid lines with arrows) and $\langle F_{fric} \rangle$ (dashed lines) for a forward and a backward scan of a FFM equipped with a soft spring. $\langle F_{fric} \rangle$ is obviously in forward direction lower than in backward direction.

two scan directions

$$\langle F_{loop} \rangle = \langle F_{fric,\rightarrow} \rangle - \langle F_{fric,\leftarrow} \rangle = \frac{\frac{1}{2}c_M(a^2 - b^2) + h_0(\frac{b}{a} - \frac{a}{b})}{a + b}. \quad (3.27)$$

It is obvious that ($\langle F_{loop} \rangle = 0$) vanishes for a symmetric potential ($a = b$) and that $\langle F_{loop} \rangle$ is antisymmetric under the transformation $a \leftrightarrow b$ as expected. Furthermore, $\langle F_{loop} \rangle$ diverges in the limiting case $a, b \rightarrow 0$ as mentioned above. This demonstrates that even with the use of this simple potential, it is possible to show a dependence of frictional forces on the scan direction. A more detailed discussion of the model and the obtained results can be found in Ref. [2].

References

- [1] D. Tománek, W. Zhong and H. Thomas, *Europhys. Lett.* **64**, 887 (1991)
- [2] U. D. Schwarz, H. Bluhm, H. Hölscher, W. Allers, and R. Wiesendanger, in: *The Physics of Sliding Friction*, ed. by B. N. J. Persson, NATO ASI Series, Kluwer, Dordrecht, 1996 (in press).

3.4.4 Anisotropy of sliding friction on the TGS (010) surface

H. Bluhm, U. D. Schwarz and K.-P. Meyer

A conventional experimental procedure to verify the frictional anisotropy predicted in Sect. 3.4.3 would include the measurement of the friction coefficient on a sample in one direction before rotating the sample to a different angle relative to the sliding direction and measuring the friction coefficient again. This requires in the case of friction force microscopy that the cantilever is retracted and reapproached for each of the subsequent measurements, i.e. the experimental conditions are each time slightly changed. This involves errors of about $\pm 10\%$ even if the same cantilever is used and even if the measurements are performed under the same experimental conditions. Thus, if the differences in the friction coefficients caused by different arrangements of the molecules are not significantly larger than 10 %, a frictional anisotropy cannot be demonstrated.

In order to prove the predicted dependence of the frictional forces on the scan direction, friction force microscopy measurements were carried out on freshly cleaved (010) surfaces of triglycine sulfate (TGS). TGS is a ferroelectric material with a Curie temperature of $T_c = 49\text{ }^\circ\text{C}$. In its ferroelectric phase, TGS exhibits the monoclinic space group $P2_1$ with lattice constants $a = 9.15\text{ \AA}$, $b = 12.69\text{ \AA}$, $c = 5.73\text{ \AA}$ and $\beta = 105^\circ$ [1]. The orientation of the unit cell relative to the sample edges was determined by means of X-ray diffraction.

The crystal structure of TGS is built up from layers stacked along the b -axis [2]. Subsequent layers consist either of glycinium and sulfate ions (type A), or only glycinium ions (type B). Neighboring layers have a distance of $b/4$, layers with equal chemical composition are separated by $b/2$. The surface of the positive domain is of A-type, whereas the surface of the negative domain is always of B-type. [3]

Figure 3.35 displays a view on two neighboring terraces separated by a $b/2$ step at

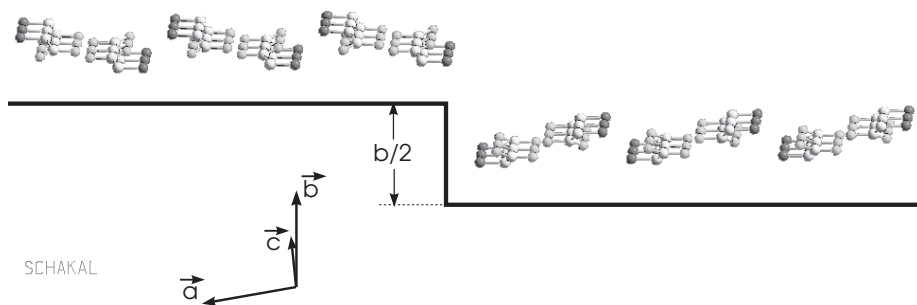


Figure 3.35: Perspective view of the (010) surface of a negative domain exhibiting a surface step of half of the unit cell height.

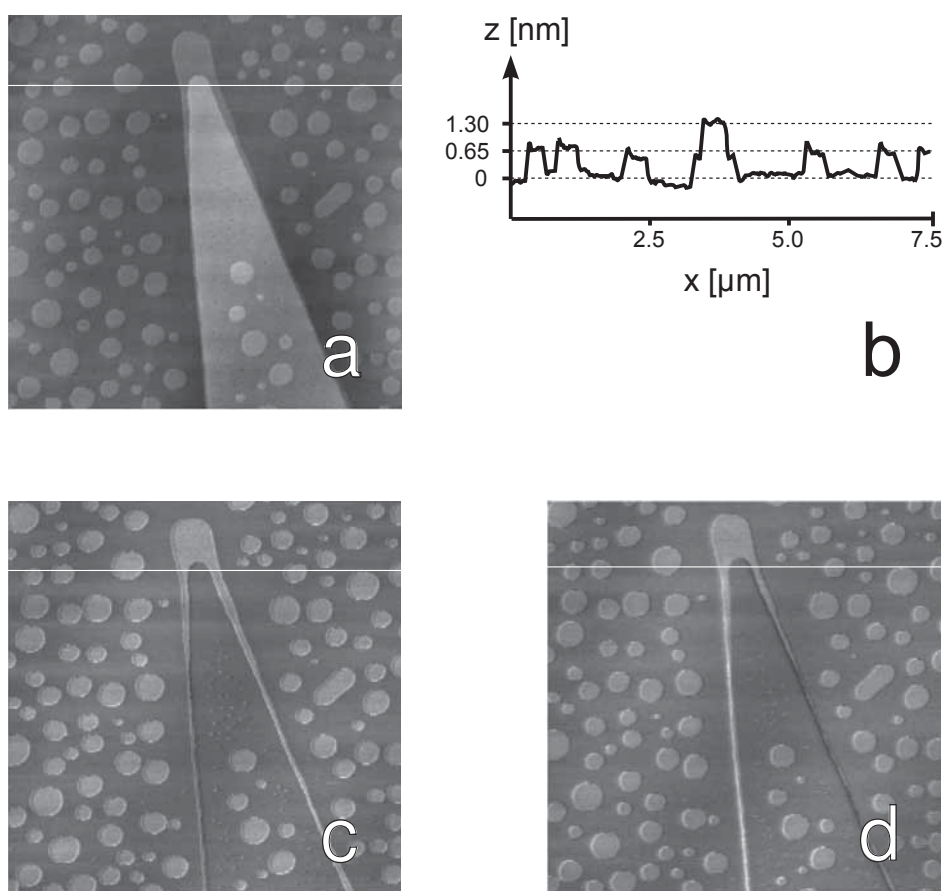


Figure 3.36: a) $7.5 \times 7.5 \mu\text{m}^2$ topographical image of the surface of a negative domain. Single steps have a height of $b/2$. b) z -profile taken along the line indicated in a. c) Friction force map acquired in forward scan direction on the same surface spot as shown in a. d) Friction force map acquired in backward scan direction.

the negative domain. The glycinium molecules form a saw-tooth like pattern perpendicular to the c -axis. The arrangement of the molecules on the upper terrace is rotated by 180° compared to the structure on the lower terrace. This saw-tooth like surface structure is very similar to the case considered theoretically in Sect. 3.4.3. Therefore, an asymmetry in friction can be expected. It is important to notice that $\langle F_{fric,\rightarrow} \rangle$ and $\langle F_{fric,\leftarrow} \rangle$ can be independently measured under identical experimental conditions due to the convenient arrangement of the surface structure on the different terraces in this example.

The friction force microscopy investigations were carried out with an instrument which is able to monitor the topography and frictional forces simultaneously [4]. All measurements were performed in contact mode and under ambient conditions using V-shaped silicon nitride cantilevers with integrated pyramidal tips and force constants of about 0.06 N/m [4].

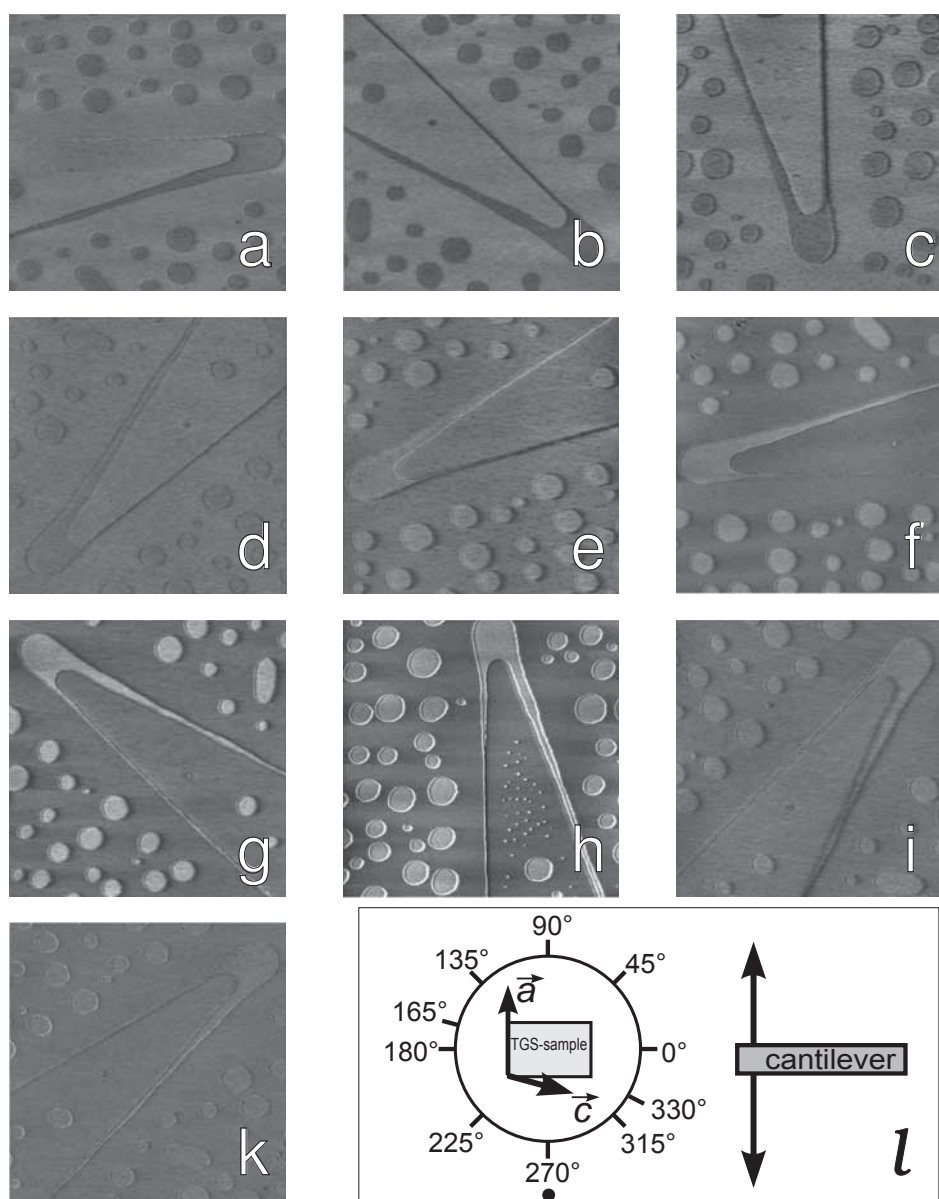


Figure 3.37: $5 \times 5 \mu\text{m}^2$ large forward friction scan images of the same surface spot as in Fig. 3.36, acquired at different scan angles: a) 0° , b) 45° , c) 90° , d) 135° , e) 165° , f) 180° , g) 225° , h) 270° , i) 315° , k) 330° . l) Experimental arrangement of the measurements shown in a-k. The cantilever scan direction is fixed. The rotation angles given in a-k refer to that number which points to the black dot indicated in the sketch. In the present case, the sample rotation angle would be denoted by 270° , and the cantilever would scan parallel to the a -axis.

Figure 3.36a shows a topographical image of the surface of a negative domain. A cleavage step runs from the bottom to the top of the image. The round islands visible

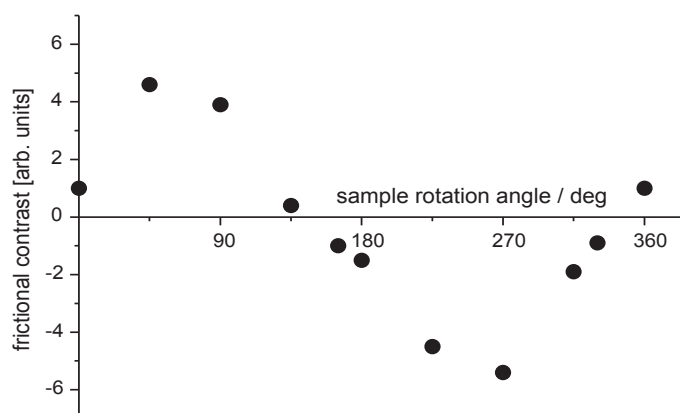


Figure 3.38: Relative frictional contrast as a function of the sample rotation angle. Each data point represents an average value of several profile lines taken from the images presented in Fig. 3.37a-k.

on the terraces are recrystallization products [5, 6]. Each monostep in Fig. 3.36a has a height of 0.65 nm ($b/2$). A z -profile taken along the line indicated in Fig. 3.36a is shown in Fig. 3.36b.

The corresponding friction force map acquired during the time when the tip was moving from the left to the right (“forward friction image”) is given in Fig. 3.36c. Bright colors represent high and dark colors low frictional forces. Two types of areas differing in their frictional behavior are obvious. The comparison of the friction image with the topographical map reveals that terraces separated by steps with height nb ($n = 0, 1, 2 \dots$) always show similar frictional contrast, whereas the frictional signal differs for terraces separated by steps with height $nb + b/2$. Fig. 3.36d shows the friction force map which was recorded when the tip was moving from the right to the left (“backward friction image”). The contrast on the terraces is similar to that observed for the forward scan direction, i.e. areas which appear bright in the forward friction image are also bright in the backward friction image (same for dark areas). However, in Fig. 3.36d, bright colors mean low and dark colors mean high frictional forces. Thus, this behavior is contrary to conventional friction force measurements where the frictional contrast is inverse for forward and backward scan direction [7]. This behavior points to a directional dependence of the friction coefficients mentioned above. The difference of the absolute values of the frictional forces between terraces which show different frictional contrast was about 4 %.

In order to investigate the frictional behavior in more detail, the sample was rotated by different angles relative to the cantilever movement. A series of images is presented in Fig. 3.37a-k. Only the forward scan direction images are displayed since the contrast was always similar for both scan directions, as seen in Fig. 3.36. The orientation of the sample relative to the cantilever movement at the different rotation angles is sketched in Fig. 3.37l.

The comparison of the FFM images at different sample rotation angles (Fig. 3.37a-

k) reveals variations in both sign and magnitude of the frictional contrast. The contrast is reversed for rotation angles ϑ and $\vartheta + 180^\circ$. The strongest contrast appears at rotation angles $\vartheta = 45^\circ$ and 90° , respectively (and also at $\vartheta = 225^\circ$ and 270° , but with opposite sign). At $\vartheta = 135^\circ$, 165° , 315° and 330° , the frictional contrast is weak.

For a quantification of the magnitude of the frictional contrast, the differences between the frictional signals acquired on the terraces separated by steps with height $nb + b/2$ was calculated from z -profiles taken from the friction force maps shown in Fig. 3.37a-k. A reversed frictional contrast is expressed by an opposite sign of the contrast value. Fig. 3.38 shows the qualitative behavior of the frictional contrast as a function of the sample rotation angle ϑ .

This is in good agreement with the structural model shown in Fig. 3.35 which suggests that the frictional contrast between terraces separated by steps with height $nb + b/2$ will be strongest for scan directions perpendicular to the c -axis, since the anisotropy in the surface potential is most prominent in this direction. On the other hand, the frictional contrast should vanish for scan directions parallel to the c -axis.

In summary, it was shown that the frictional forces on the TGS (010) surface are highly anisotropic. This behavior could be correlated with the crystallography of TGS which features an asymmetric arrangement of the molecules at the (010) surface, thus causing an asymmetric surface potential. For a more detailed discussion of the friction anisotropy of the TGS (010) surface, including the friction properties of the positive domains, see Ref. [6].

References

- [1] E. A. Wood and A. N. Holden, *Acta Cryst.* **10**, 145 (1957).
- [2] S. Hoshino, Y. Okaya, R. Pepinsky, *Phys. Rev.* **115**, 323 (1959).
- [3] N. Nakatani, *Jpn. J. Appl. Phys.* **18**, 491 (1979).
- [4] Nanoscope III, Digital Instruments, Santa Barbara, CA, USA.
- [5] H. Haefke, R. Lüthi, K.-P. Meyer, E. Meyer, L. Howald, H.-J. Güntherodt, *Ferroelectrics* **151**, 143 (1994).
- [6] H. Bluhm, U. D. Schwarz, K.-P. Meyer, R. Wiesendanger, *Appl. Phys. A*, **61**, 525 (1995).
- [7] see, e.g., R. M. Overney and E. Meyer, *Bull. Mater. Res.* 26-34 (1993).

3.5 Electrostatic Force Microscopy on ferroelectric crystals

H. Bluhm, A. Wadas, L. Szczesniak and K.-P. Meyer

The domain structure of ferroelectric crystals can be imaged by a variety of techniques as, e.g., scanning electron microscopy [1], optical microscopy [2], and transmission electron microscopy using the decoration technique [3]. Scanning force microscopy allows direct mapping of the domain structure with high resolution. In previous work Saurenbach et al. [4] detected charges of the domains as well as domain walls by means of non-contact dynamical force microscopy (DFM). Lüthi et al. [5] used friction force microscopy (FFM) for the imaging of ferroelectric domains. These authors also applied DFM for the visualization of the domain walls. In this chapter, three different methods for the imaging of the ferroelectric domain structure of guanidinium aluminium sulfate hexahydrate (GASH) crystals are compared: FFM, static non-contact (dc lift-mode [6]) and dynamic non-contact force microscopy (ac lift-mode).

1) Friction force microscopy

Figure 3.39(a) shows a typical image of a freshly cleaved GASH (0001) surface. Cleavage steps with a height of 0.9 nm can be observed. This value corresponds to a step height of one unit cell in c -direction. Fig. 3.39(b) gives the forward friction scan image (i.e. the tip was moved from left to right) of the same area as in (a). The cleavage steps appear as straight lines due to the torque of the cantilever at the step edges. Additionally, ferroelectric domains of various shapes are obvious. Domains of different polarity can be distinguished by a different contrast in the friction image. Fig. 3.39(c) shows the backward friction image which reveals a reversed frictional contrast



Figure 3.39: **a** Topographic image of the GASH (0001) surface, scan size: $20 \mu\text{m} \times 20 \mu\text{m}$; **b** Forward friction scan image for the same area, **c** Backward friction scan image.

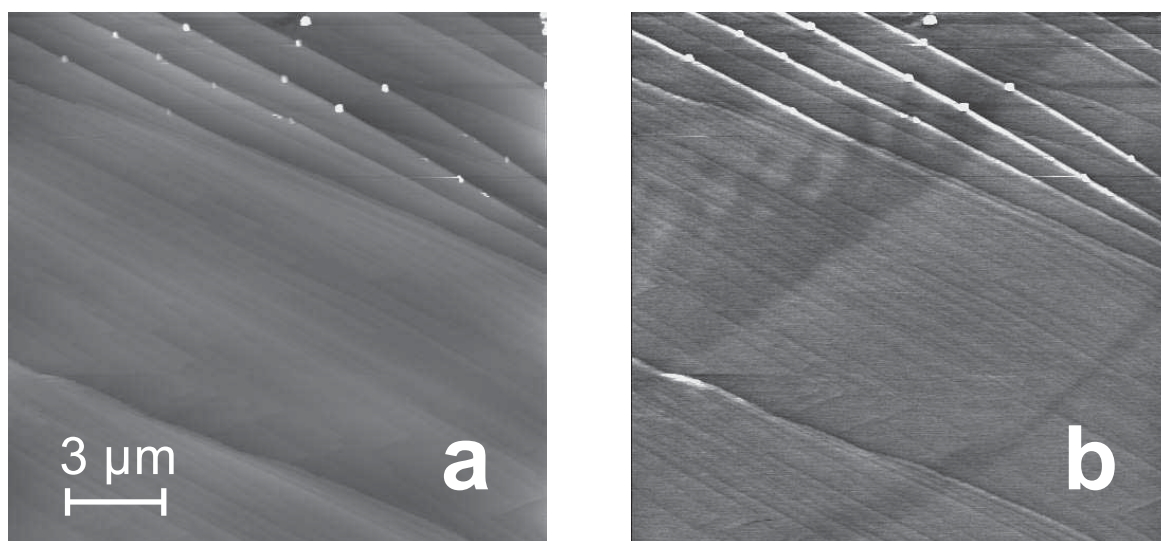


Figure 3.40: **a** Sample topography of GASH (0001), scan size: $15 \mu\text{m} \times 15 \mu\text{m}$; **b** dc lift-mode image of the same area (lift height 100 nm). Domains can be distinguished by the deflection of the cantilever due to attractive or repulsive electrostatic forces originating from the domains of different polarity. The tip is attracted above areas with dark contrast.

of the ferroelectric domains. A discussion of the contrast mechanism of ferroelectric domains in FFM imaging is given in [5].

II) Static non-contact force microscopy (dc lift-mode)

In lift-mode [6] the tip probes the sample surface twice: First, the tip tracks the sample topography on one scan line. In a second step, the tip is raised to a certain height above the surface (typically 50-100 nm) and scanned again above the same line as in the first scan. The distance to the sample surface is kept constant during the lift scan. Thus, only long range forces (such as magnetic or electrostatic forces) contribute to the deflection of the cantilever in the second scan. However, due to small deviations in the actual lift height during the second scan a cross-talk of the topography on the deflection signal can be observed.

Figure 3.40(a) shows the topography of the sample measured in the repulsive force regime (i.e. the tip is in contact with the surface) revealing a typical cleavage step structure.. The corresponding lift-mode image is given in Fig. 3.40(b). Beside the above mentioned cross-talk of the topography, a domain structure similar to that shown in Figs. 3.39(b) and (c) can be observed. The domain contrast is caused by the different interaction of the tip carrying trapped charges with the surface charges of domains with opposite polarity.

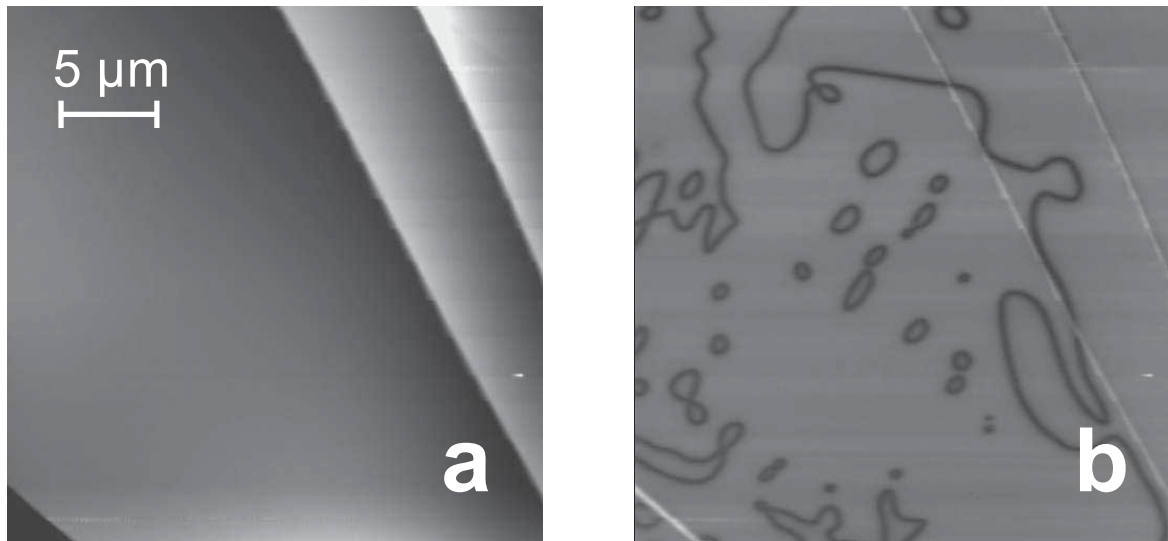


Figure 3.41: **a** Topographic image of the GASH (0001) surface, scan size: $45\ \mu\text{m} \times 45\ \mu\text{m}$; **b** ac lift-mode image (phase contrast) of the same area. A darker contrast means a negative shift of the resonance frequency, i.e. a more attractive force gradient than on brighter areas.

III) Dynamic non-contact force microscopy (ac lift-mode)

While the dc lift-mode gives a direct measure of the long-range forces acting on the cantilever, the ac lift-mode is sensitive to force gradients above the sample surface [7]. The cantilever is vibrated close to its resonance frequency. A force gradient acting on the cantilever leads to a shift in the resonance frequency which can be measured by different methods [8].

The topography of the GASH (0001) surface is given in Figure 3.41(a) showing some cleavage steps with heights of several nanometers. Fig. 3.41(b) is the corresponding lift-mode image (lift height 150 nm). A change in the resonance frequency (i.e. a change in the force gradient) is detected by the change in the phase lag between the drive frequency and the actual frequency of the cantilever [8]. A darker contrast means a lower resonance frequency and hence a more attractive force gradient. In contrast to the friction force and dc lift-mode measurements which are sensitive to the domains, ac lift-mode rather reveals the walls of ferroelectric domains.

In conclusion, different operation modes of the force microscope can be used to image the ferroelectric domain structure. A comparative discussion of the domain contrast observed with friction force microscopy as well as with static and dynamic non-contact force microscopy will be given in a forthcoming paper.

References

- [1] L. Szczesniak and L. Szczepanska, *Ferroelectrics* **111**, 167 (1990).

- [2] N. Nakatani, *J. Phys. Soc. Jpn.* **39**, 741 (1975).
- [3] G.I. Distler, V.P. Konstantinova, Y.M. Gerasimov, and G.A. Tolmacheva, *Nature* **218**, 762 (1968).
- [4] F. Saurenbach and B.D. Terris, *Appl. Phys. Lett.* **56**, 1703 (1990).
- [5] R. Lüthi, H. Haefke, K.-P. Meyer, E. Meyer, L. Howald, and H.-J. Güntherodt, *J. Appl. Phys.* **74**, 7461 (1993).
- [6] NanoScope IIIa manual, Digital Instruments, Santa Barbara, CA.
- [7] see, e.g., Y. Martin, C.C. Williams, and H.K. Wickramasinghe, *J. Appl. Phys.* **61**, 4723 (1987).
- [8] see, e.g., T.R. Albrecht, P. Grütter, D. Horne, and D. Rugar, *J. Appl. Phys.* **69**, 668 (1991).

3.6 Magnetic Force Microscopy and Tunneling Stabilised Magnetic Force Microscopy

Andrzej Wadas

Magnetic force microscopy (MFM) is already a third generation of scanning probe techniques after scanning tunneling microscopy and scanning force microscopy. MFM has been designed to study the fringing field above magnetic materials. The principal idea of that method relies on the magnetostatic interaction between the magnetic sample and the magnetic sensor attached to the flexible cantilever. It is raster scanned over the sample surface typically in the range of tens to hundreds of nanometers. A magnetic sample with a domain structure produces a complicated stray field over the surface. The aim of the MFM is to map the stray field as close to the surface as possible. An interaction which appears when a sample is scanned by a MFM sensor, is monitored via a deflection of a cantilever. It is important to have corresponding topographic and magnetic images of the same area. We have applied a form of MFM operation which affords line-by-line simultaneous acquisition of topography and magnetic force giving us the opportunity to study correlations between the morphology of the surface and the magnetic domain structure.

Recently, another approach named Tunneling Stabilized Magnetic Force Microscopy (TSMFM) was developed. TSMFM is performed by using a scanning tunneling microscope with a flexible, magnetic tunneling tip instead of the usual rigid tip. The tip position is stabilized near the surface of the magnetic sample using the STM feedback system as tunneling occurs between the tip and sample surface. If the stray field from the sample attracts the tip, then the feedback system (maintaining a constant tunneling gap) pulls the tip off the surface. It is obvious that TSMFM images are then combinations of surface topography and the magnetic forces on the tip. This method is especially useful to study flat surfaces of magnetic materials. Even nonconductive samples covered by a very thin layer (2 nm) of Pt-C were studied using this technique.

Either MFM or TSMFM provide a high sensitivity and a very high lateral resolution of 50 nm or better. This has mainly been achieved by using complex magnetic thin film sensors. The preparation of these sensors determines not only the resolution and sensitivity of MFM but also opens a possibility to study magnetic features on a nanometer scale. We present some of results obtained by using MFM and TSMFM in the next few sections.

3.6.1 Structure of cross-tie wall in thin Co films resolved by magnetic force microscopy

M. Löhndorf, A. Wadas, and H.A.M. van den Berg

Recent interest in magnetic domain structures of Co and Co-based thin films results mainly from the possible application of these compounds as data storage media.

We have chosen magnetic force microscopy (MFM), a technique capable to detect a stray field of a sample some tens of nanometers above a surface. No special sample preparation is required for this method. MFM detects the magnetic force exerted on a magnetic tip while it is scanned over the sample surface.

The measurements reported here have been performed in a DC-mode under ambient conditions. We have used non invasive magnetic thin film sensors in order to observe domain structure in magnetically soft materials. The Co films were prepared on glass and SiO₂ substrates at room temperature by sputtering.

In the past, domain walls in thin ferromagnetic materials were investigated by means of different methods like Kerr-microscopy or Bitter technique. Due to the higher lateral resolution of MFM in comparison with optical methods, we have been able to study the magnetic structure of a cross-tie wall. Figure 3.42(a) presents an example of MFM image of a cross-tie wall. The proposed domain configuration is shown in Figure 3.42(b).

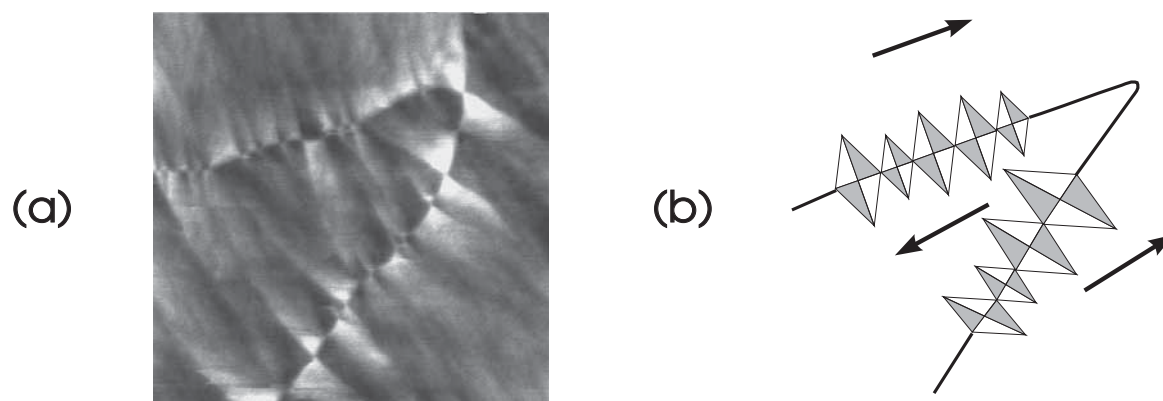


Figure 3.42: **a)** MFM image ($20\ \mu\text{m} \times 20\ \mu\text{m}$) of a 50 nm polycrystalline Co film showing a cross-tie wall enclosing a domain. A schematic drawing of the domain structure is given in **b)**. Single cross-ties in our model are represented by rhombs. The magnetization directions of the domains are marked by arrows.

The arrows represent the possible directions of domain magnetization. Rhombs are graphical models of cross-ties within the domain wall. In contrast to Bitter pattern, where cross-ties appear as bright short bars perpendicular to a wall, the MFM image shows a more detailed check-pattern representing a system of cross-ties. A single cross-

tie in the MFM image consists of four segments: one dark and one bright region on each side of the domain wall with reversed contrast with respect to the wall. A section of a domain wall with some cross-ties of different sizes observed by MFM is shown in Fig. 3.43(a). Below the image we enclose the theoretical model of a cross-tie (left) and a schematic drawing of the observed data (right). According to the model the direction of magnetization changes more rapidly at every second Bloch line forming the cross-tie. Since Bloch lines (marked in our case by \odot and \otimes) are located periodically, we identify their positions in the MFM picture as shown in the schematic drawing using letters A and B. The center of each cross-tie is placed where two either bright or dark parts meet each other within one rhomb (point A). This point is characterized by a maximum magnetic contrast. Bloch lines with opposite direction (marked with \otimes) are located between two cross-ties (marked by B).

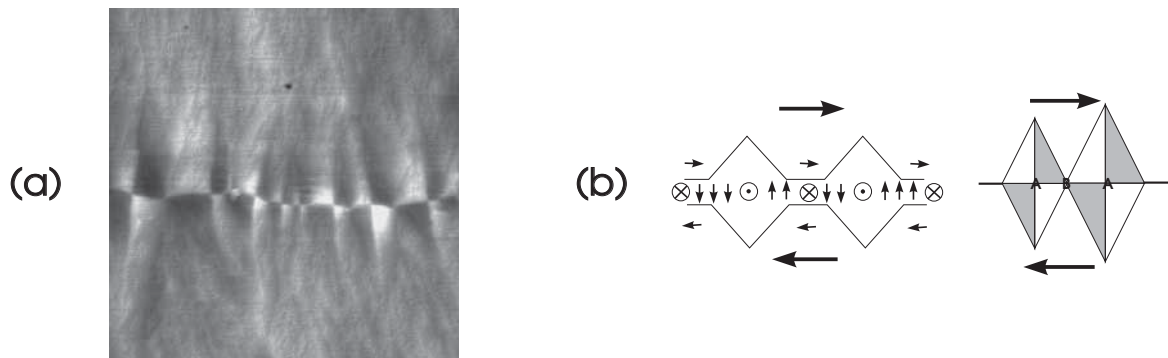


Figure 3.43: **a)** MFM image ($20 \mu\text{m} \times 20 \mu\text{m}$) showing cross-ties of various sizes. A schematic drawing of a theoretical model is shown on the left side **b)**. The magnetization directions are indicated by arrows, whereas the Bloch lines are marked by \odot and \otimes respectively. On the right hand side a model of our MFM data is given. Proposed locations of the Bloch lines are indicated by A and B.

In summary we have resolved cross-tie walls of thin polycrystalline Co films by MFM. The measurements were performed with magnetically soft tips (low coercivity) to avoid an influence of the magnetic stray field of the tip on the sample domain configuration. The observed MFM contrast led to a model for the interaction between the MFM tip and sample which will be explained in more detail in a forthcoming publication [1].

References

- [1] M. Löhndorf, A. Wadas, H.A.M. van den Berg, and R. Wiesendanger, submitted for publication.

3.6.2 Domain structure of Co/Pt multilayers

M. Löhndorf, A. Wadas, and H. W. van Kesteren

Since Co/Pt multilayers with perpendicular anisotropy were suggested for the application as perpendicular recording media, growing interest in these materials initiated numerous investigations [1-10]. A major part of these investigations was concentrated on the influence of the two factors: thickness of the Co layer and the interface roughness on the magnetic properties of these multilayers (ML). It was found that below a certain Co layer thickness ($< 8 \text{ \AA}$) these materials exhibit a perpendicular anisotropy. Only few investigations concentrated on the domain structure of multilayer systems [6,10].

We have chosen magnetic force microscopy (MFM) as an appropriate method to study simultaneously the surface morphology and the magnetic structure. This technique revealed high lateral resolution of at least 50 nm and high force sensitivity of 10^{-12} N. We report here on the domain structure of Co/Pt multilayer in a demagnetized state obtained either by lowering the field or by an oscillating field. We also studied the stability of the domain structure with respect to a small magnetic field using MFM.

The Co/Pt ML [$15 \times \text{Co} (3.5 \text{ \AA}) / \text{Pt} (6 \text{ \AA})$] were prepared on glass substrates at room temperature by electron-beam evaporation from separate Co and Pt sources. The domain structure of the multilayer system with perpendicular anisotropy is determined by oppositely polarized domains, perpendicular with respect to the surface and separated by 180° domain walls.

First, MFM measurements on the Co/Pt ML were carried out without an external

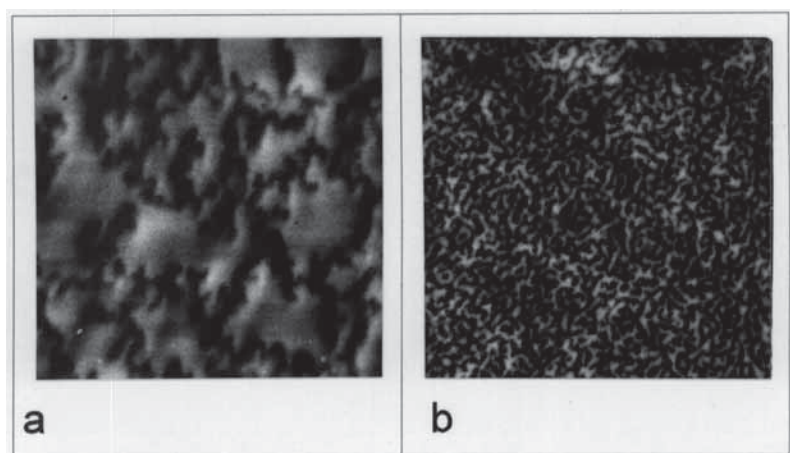


Figure 3.44: **a** MFM image of an Co/Pt multilayer demagnetized by lowering the field, scan size: $10 \mu\text{m} \times 10 \mu\text{m}$; **b** MFM image of an Co/Pt multilayer demagnetized by an oscillating field, scan size: $10 \mu\text{m} \times 10 \mu\text{m}$.

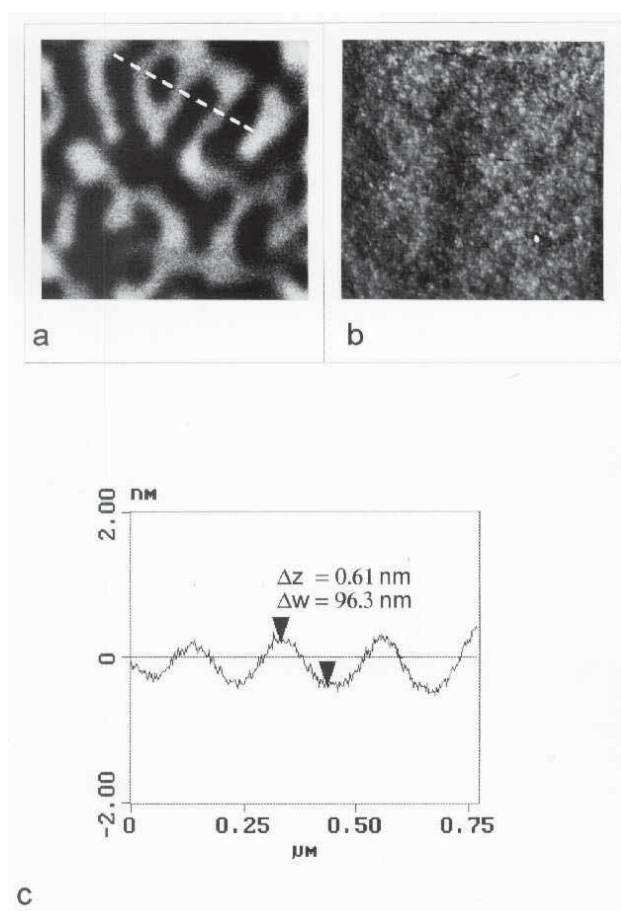


Figure 3.45: **a** MFM image of an Co/Pt multilayer demagnetized by an oscillating field, scan size: $1.3 \mu\text{m} \times 1.3 \mu\text{m}$, **b** Corresponding topographic image; **c** Cross section along dashed line, showing the width of the domains.

field. Figure 3.44 shows two MFM images ($10 \mu\text{m} \times 10 \mu\text{m}$) of differently demagnetized Co/Pt samples. In our case, bright and dark area in the MFM picture correspond to different domains due to repulsive or attractive forces acting between the tip and the sample. The MFM image of the sample demagnetized by lowering the field (Fig. 3.44 a) shows different domain widths for both types of domain polarization. The width of the bright domains, which are dominant for this sample, is about 3 to 5 μm , whereas the size of the dark domains are about 200 to 250 nm. In contrast, the sample demagnetized by an oscillating field (Fig. 3.44 b) has a different domain structure. The domain width is of the same order of 70 to 130 nm for both, dark and bright domains.

In our case demagnetization by lowering the applied field did not lead to a complete demagnetization of the Co/Pt ML. Domain structures obtained by both demagnetization methods remained stable and were unaffected by the scanning MFM tip.

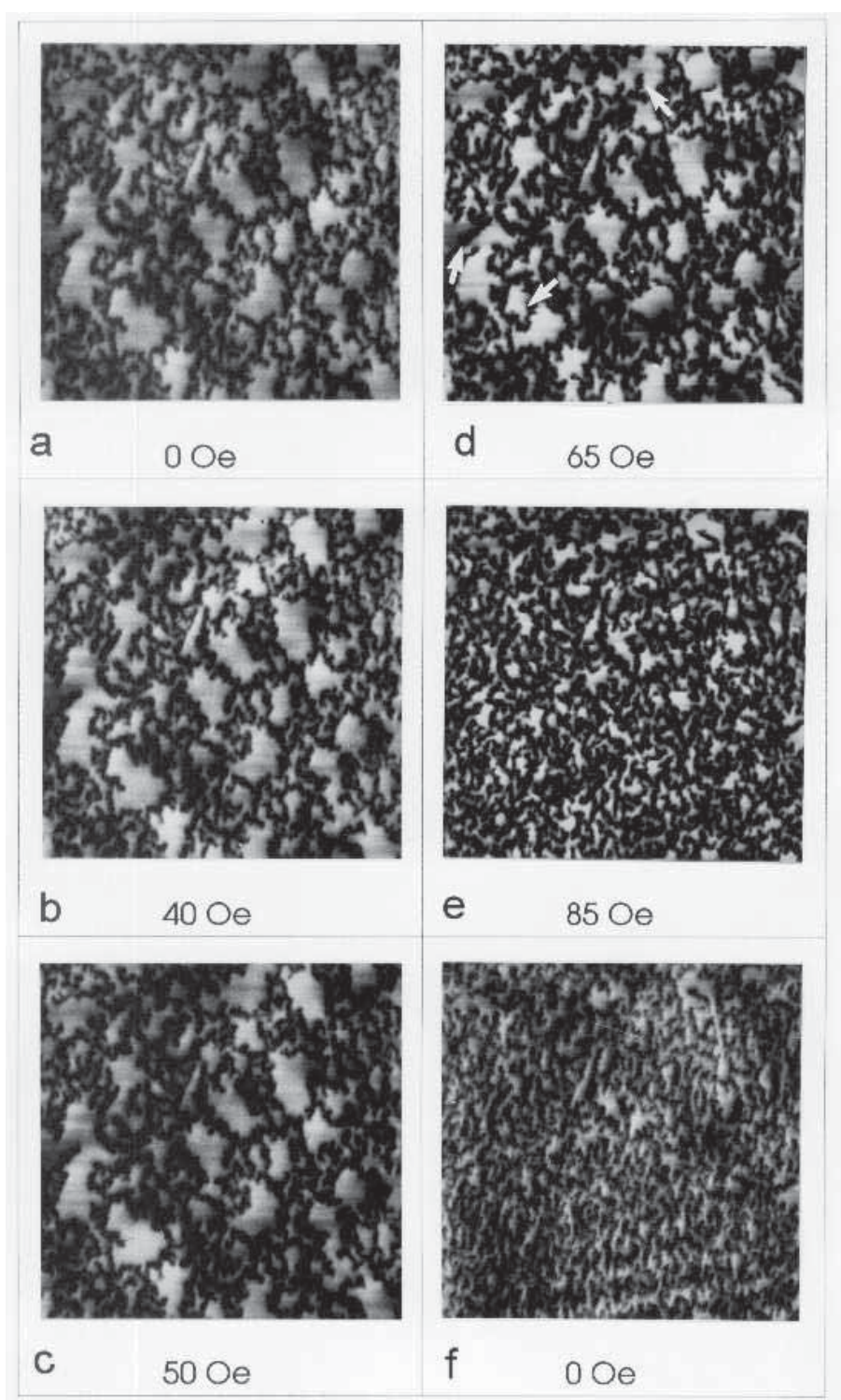


Figure 3.46: Series of MFM images, scan size: $20 \mu\text{m} \times 20 \mu\text{m}$; of the same location showing the influence of an applied field at different field strength on the domain structure. **a** 0 Oe, **b** 40 Oe, **c** 50 Oe, **d** 65 Oe (arrows indicating changes of domains), **e** 85 Oe and **f** field strength of 0 Oe 2 min. afterwards.

Figure 3.45 shows the domain structure (left) and the corresponding topography of the sample (right) demagnetized by an oscillating field on a small ($1.3 \mu\text{m} \times 1.3 \mu\text{m}$) area. The rms roughness of the topography image is 0.37 nm which is typical for the entire sample. We did not find any correlation between surface topography and the magnetic domain structure. In order to better illustrate the magnetic contrast, a cross section along the dotted line of the magnetic image is presented (Fig. 3.45 c). The peak-peak distance (marked on the cross section) represents approximately a measure of a domain width and is in the range of 70 to 110 nm (Δw). The force associated with the difference in the magnetic contrast between dark and bright domain is about 4×10^{-11} N (Δz).

In order to study the stability of the domain structure of the Co/Pt ML with respect to a small external magnetic field we placed the MFM microscope into a solenoid with a field perpendicular to the sample surface.

Figure 3.46 presents a series of MFM pictures ($20 \mu\text{m} \times 20 \mu\text{m}$) of the same location on the sample. The field applied normal to the plane of the multilayer sample (same direction as the dark domain) was increased from 0 Oe to 85 Oe (Fig. 3.46 a-e) and finally decreased to 0 Oe (Fig. 3.46 f). The domain structure was unchanged until a field up to 50 Oe was applied. Then dark domains began to expand. Simultaneously bright domains shrunk (Fig. 3.46 c). Further increasing of the applied field led to an irreversible movement of domains. A splitting of the big bright domains ($> 5 \mu\text{m}$) started (see arrows Fig. 3.46 d) and the domain structure became unstable. At a field strength of 85 Oe the final domain structure is similar to the one of the sample demagnetized by an oscillating field. The width of the domain is now almost the same for both types of domain, bright and dark, now with a width of 200 to 300 nm. They are still by a factor of 2 wider than domains presented in Fig. 3.44 b. Decreasing the field to 0 Oe did not change the domain structure with respect to Fig. 3.46 e but the MFM contrast was reduced (Fig. 3.46 f). We explain the reduction of magnetic contrast by a tip change due to release of the external field. Figure 3.46 f was taken 2 min after switching off the applied field. Further change of the domain structure was not observed.

Similar experiments as described above, performed on the sample demagnetized by an oscillating field revealed no change of the domain structure even at a field strength of 110 Oe. This means that the method of an oscillating field leads to the demagnetized state which is stable with respect to small magnetic fields. For further experimental details see Ref. [11].

References

- [1] P. F. Carcia, A. D. Meinhaldt, and A. Suna Appl. Phys. Lett. **47**, 178 (1985).
- [2] F. J. A. den Broeder, H.C. Donkersloot, H. J. G. Draaisma, and W.J.M. de Jonge J. Appl. Phys. **61**, 4317 (1987).
- [3] P. F. Carcia J. Appl. Phys. **63**, 5066 (1988).

- [4] A. J. den Boef *Appl. Phys. Lett.* **56**, 2045 (1990).
- [5] S. Hashimoto, Y. Ochiai, and K. Aso *J. Appl. Phys.* **67**, 4429 (1990).
- [6] H. W. van Kesteren, A.J. den Boef, W.B. Zeper, J.H.M. Spruit, B. A. J. Jacobs, and P. F. Carcia *J. Appl. Phys.* **70**, 2413 (1991).
- [7] W. B. Zeper, H.W. van Kesteren, B. A. J. Jacobs, J. H. M. Spruit, and P. F. Carcia *J. Appl. Phys.* **70**, 2264 (1991).
- [8] H. Takeshita, K. Hattori, Y. Fujiwara, K. Nakagawa, and A. Itoh *J. Appl. Phys.* **75**, 6415 (1994).
- [9] R. T. Heap, and S. J. Greaves *J. Phys. D: Appl. Phys.* **27**, 1343 (1994).
- [10] J. R. Barnes, S. J. O' Shea, M. Welland, J.-Y. Kim, J. E. Evetts, and R.E. Somekh *J. Appl. Phys.* **76**, 2974 (1994).
- [11] M. Löhndorf, A. Wadas, H. W. van Kesteren, and R. Wiesendanger, submitted to *J. Vac. Sci. Technol. B*.

3.6.3 Tunneling stabilized magnetic force microscopy of $BaFe_{12}O_{19}$ with a magnetic thin film tip

A. Wadas and Ch. Wittneven

The experimental method of tunneling stabilized magnetic force microscopy is performed by using a scanning tunneling microscope (STM) with a flexible, magnetic tunneling tip instead of the usual rigid tip [1]. The tip position is stabilized near the surface of the magnetic sample using the STM feedback system as tunneling occurs between the tip and surface. If the stray field from the sample attracts the tip, then the feedback system (maintaining a constant tunneling gap) pulls the tip off the surface. The measured magnetic forces have their origin in the interaction between the tip and the sample magnetic microstructure. Small effects on the measured signal can also be expected because of the influence of surface roughness on the sample stray field. The magnetic tip plays the most important role in the TSMFM experiment. Lateral resolution is limited by its geometry, e.g. shape and size, and by its magnetic state. We have found that a thin film tip in particular should give us high lateral resolution [2]. The magnetic anisotropy energy of the tip, the demagnetization energy of the tip and the interaction energy between the tip and the sample determine the minimum energy of the tip while scanning the magnetic sample. Therefore, the behavior of the magnetic tip depends on which of these factors is dominating under the particular set of experimental conditions. It is obvious that a value of the sample stray field is different at different heights above the sample, increasing its value towards the surface. A tip with a defined magnetic anisotropy will be magnetically soft or hard depending

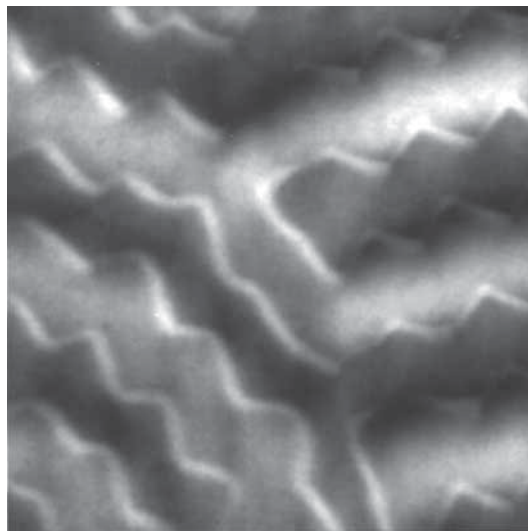


Figure 3.47: The magnetic domain structure observed on Ba-ferrite. White lines represent domain walls. The scan size is $11.5 \mu\text{m} \times 11.5 \mu\text{m}$.

on the scanning height. Softness means that the tip's magnetization mainly depends on changes in the stray field of the sample, whereas hardness describes the constant direction of the tip's magnetization regardless of the lateral position of the tip over the sample.

The purpose of this work is to image magnetic domain structure on a thin platelet of $\text{BaFe}_{12}\text{O}_{19}$ single crystal using TSMFM with a thin film tip. The tunneling probe consists of a cantilever with an integrated tip with $k = 0.3\text{N/m}$ coated in our laboratory first with a 30 nm Fe film and then with a 5 nm Au film. The gold film protects the magnetic layer against oxidation and ensures good tunneling conditions. The image presented in Figure 3.47 has been obtained with a bias voltage of 450 mV and a tunneling current of 0.5 nA. Different orientations of the magnetic domains appear as different height levels. The domains are separated by narrow bright lines which we have interpreted as domain walls. The width of the narrow bright line is around 150 nm. The part of the tip which is magnetically soft is responsible for giving the contrast of a domain wall. We estimate our lateral resolution to be better than 50 nm.

References

- [1] J. Moreland and P. Rice, *J. Appl. Phys.* **70**, 520 (1991)
- [2] A. Wadas, P. Rice, and J. Moreland, *Appl. Phys. A* **59**, 63 (1994).

3.7 Scanning Capacitance Microscopy

M. Dreyer and A. Born

Spatially resolved capacitance measurements by means of a sharp metal probe being scanned in close proximity to a sample [1] appear to be highly promising for the characterization of dielectric thin films and semiconductor devices on a submicrometer length scale.

With the advent of scanning probe technology [2,3], scanning capacitance microscopes (SCM) [4-10] have usually been realized by a combination of an atomic force microscope (AFM) [11] with a commercial RCA [12], JVC resp. or a home-built capacitance sensor. Interesting applications of SCM were found in the near-field lateral dopant profiling of semiconductor devices [5] and charge storage in nitride-oxide-silicon (NOS) heterostructures [6-8] on a submicrometer scale. Another interesting potential application of the SCM would be high-resolution capacitance spectroscopy at low temperatures [13].

We started our SCM activities by combining a home-built capacitance sensor (Fig. 3.48) and a commercial scanning force microscope [14]. Home-made tungsten cantilevers cut from 5- μm -thick tungsten foil and electrochemically etched to obtain sharp probe tips were used. The front end of these cantilevers was bent mechanically so that the tip end could easily be brought in contact with the NOS heterostructure without large tilt angles. The contact area was chosen not to be too small in order to obtain reasonable signal-to-noise ratio for the measured capacitance signal.

This SCM has been used to study nitride-oxide-silicon (NOS) heterostructures, which offer potential applications in charge storage technology (see chapter 3.9.3 for details) and to image the lateral change in capacitance for some semiconductor devices. In addition, SCM appears to be very useful for the characterization of sub-

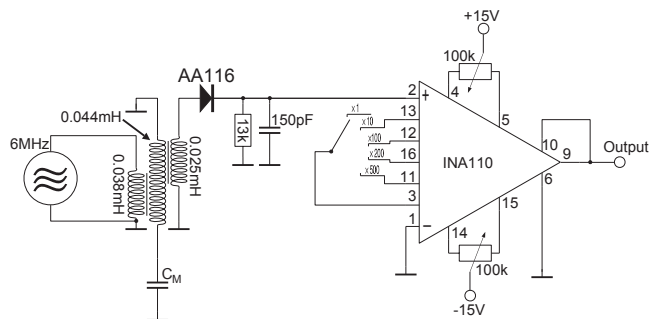


Figure 3.48: Schematics of our home-built capacitance sensor

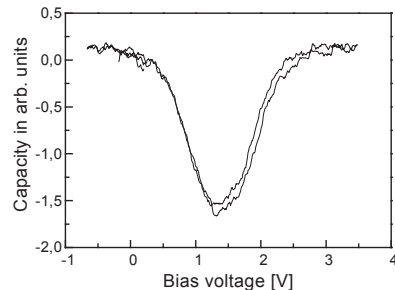


Figure 3.49: Typical $C(U)$ characteristic as measured for the tungsten tip-nitride-oxide-silicon diode.

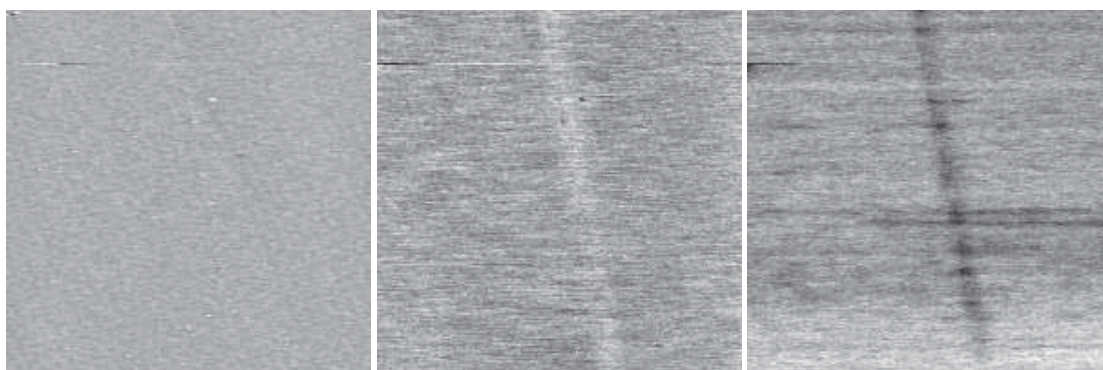


Figure 3.50: Simultaneously recorded topographic, capacitance and dC/dU -image of the same area ($35 \times 35 \mu\text{m}^2$) of a NOS heterostructure sample. A subsurface defect shows up in the C - and dC/dU -images but remains invisible in the surface topographic image.

surface defects in semiconductor devices which are inaccessible by most of the other scanned probe microscopies. Finally, a spectroscopic mode of SCM operation offers combined voltage-dependent and spatially-resolved information about inhomogeneous charge distributions in semiconductor devices.

Experimental

A metal electrode brought in contact with the top nitride layer of the NOS heterostructure forms a metal-insulator-silicon (MIS) diode. The capacity of the MIS diode is a function of a bias voltage U applied to the silicon substrate. A $C(U)$ dependency of the tungsten tip-nitride-oxide-silicon diode is shown in figure 3.49. This curve is in good agreement with theoretical MIS $C(U)$ curves as shown in [15].

As a next step, we have combined the capacitance detection with spatially resolved measurements by scanning the NOS sample relative to the metal probe tip. Three signals were recorded simultaneously as a function of lateral (x,y)-position:

- the topographic (z-) signal of normal contact AFM operation,
- the capacitance (C-) signal, and
- the first derivative (dC/dU) signal by using lock-in detection (see figure 3.63 in chapter 3.9.3).

Two examples are presented here. In Fig. 3.50 we have succeeded in locating a subsurface defect which is easily recognizable in the capacitance and dC/dU -images but does not show up in the corresponding topographic image. Such defects, which probably result from inhomogeneities at the oxide-silicon interface, were extremely

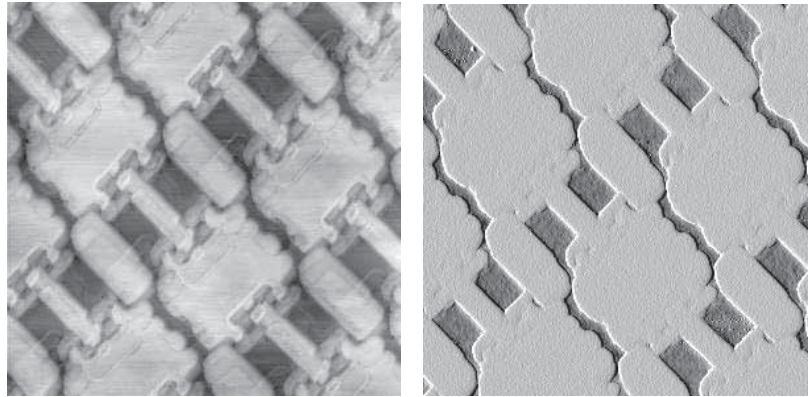


Figure 3.51: Simultaneously recorded topographic and dC/dU -image showing a memory array of a commercial silicon integrated circuit (area $50 \times 50 \mu\text{m}^2$). The dC/dU data are shown as a mix of height and derivative for contrast enhancement within the bright/dark areas.

rare in our samples. However, the present example demonstrates nicely the potential of scanning capacitance microscopy for imaging and characterization of subsurface defects with submicron spatial resolution which do not show up at the surface and therefore remain invisible for most other scanned probe microscopies [16].

Fig. 3.51 displays part of a memory array taken on a commercial silicon integrated circuit. The SCM data were measured using a capacitance sensor manufactured by JVC. The dC/dU -image shows two main areas of different contrast.

A method to extract more information about the lateral and voltage dependence of the capacitance of a semiconductor heterostructure sample, is to scan only one line repetitively while changing the bias voltage from line to line. This method is called scanning capacitance spectroscopy. An example of application to local charge modifications is shown in chapter 3.9.3.

References

- [1] J. R. Matey and J. Blanc, *J. Appl. Phys.* **57**, 1437 (1985).
- [2] G. Binnig and H. Rohrer, *Helv. Phys. Acta* **55**, 726 (1982).
- [3] R. Wiesendanger, *Scanning Probe Microscopy and Spectroscopy: Methods and Applications*, Cambridge University Press, Cambridge, 1994.
- [4] C. C. Williams, W. P. Hough, and S. A. Rishton, *Appl. Phys. Lett.* **55**, 203 (1989).
- [5] C. C. Williams, J. Slinkman, W. P. Hough, and H. K. Wickramasinghe, *Appl. Phys. Lett.* **55**, 1662 (1989).
- [6] R. C. Barrett and C. F. Quate, *J. Appl. Phys.* **70**, 2725 (1991).
- [7] R. C. Barrett and C. F. Quate, *Ultramicroscopy* **42-44**, 262 (1992).

- [8] B. D. Terris, R. C. Barrett, and H. J. Mamin, *SPIE* **1855**, 195 (1993).
- [9] Y. Huang and C. C. Williams, *J. Vac. Sci. Technol. B* **12**, 369 (1994).
- [10] Š. Lányi, J. Török, and P. Rehurek, *Rev. Sci. Instrum.* **65**, 2258 (1994).
- [11] G. Binnig, C. F. Quate, and Ch. Gerber, *Phys. Rev. Lett.* **56**, 930 (1986).
- [12] R. C. Palmer, E. J. Denlinger, and H. Kawamoto, *RCA Review* **43**, 194 (1982).
- [13] R. C. Ashoori, H. L. Stormer, J. S. Weiner, L. N. Pfeiffer, S. J. Pearton, K. W. Baldwin, and K. W. West, *Phys. Rev. Lett.* **68**, 3088 (1992).
- [14] TMX 2000, Topometrix
- [15] S. M. Sze, *Semiconductor Devices: Physics and technology*, John Wiley & sons, New York (1985)
- [16] M. Dreyer and R. Wiesendanger, *Appl. Phys. A***61**, 357 (1995)

3.8 Scanning Thermal Microscopy

J. Asmussen

The development in the production of integrated circuits is leading to smaller dimensions. Today individual structures on a chip are well below $1\ \mu\text{m}$. Thus, there is an increasing demand for new methods in failure analysis, because the resolution of conventional optical imaging is limited by the wavelength of the light used. The localisation of "hot spots" on these chips is one substantial part of failure analysis.

For imaging thermal properties of several samples a scanning thermal microscope (SThM) was developed. It is based on a commercial AFM equipped with a thermal sensor. To build this sensor different approaches were made:

First a small resistive filament was used. By measuring the resistance of the filament the temperature can be determined [1]. However, to determine the resistance a small electric current is necessary which is heating up the tip. By limiting this current to 1 mA the thermal sensitivity is limited to about $5\ \mu\text{V}/\text{K}$. The spatial resolution is limited by the diameter of the filament. A diameter of $5\ \mu\text{m}$ leads to a resolution of about $1\ \mu\text{m}$.

Second a thermocouple was built from thin metal wires. These wires were made of Alumel and Cromel. They were electrochemically etched in NaOH to form a tip and bond together by discharging a capacitor over a mechanical contact [2]. After sticking a mirror to these wires we got a working AFM tip with a thermal sensitivity of about $40\ \mu\text{V}/\text{K}$. The lateral resolution is limited by the radius of curvature of the etched tip of a single wire. It is well below 500 nm.

The third approach is to coat an AFM tip with two different metals [3]. A standard AFM cantilever made of Si_3N_4 is used. A gold film is deposited on one cantilever arm, while a platinum film is deposited on the other arm. This forms a thermocouple junction on the cantilever tip. This thermocouple has got a lower thermal sensitivity than an Alumel-Cromel junction, but the spatial resolution is further improved.

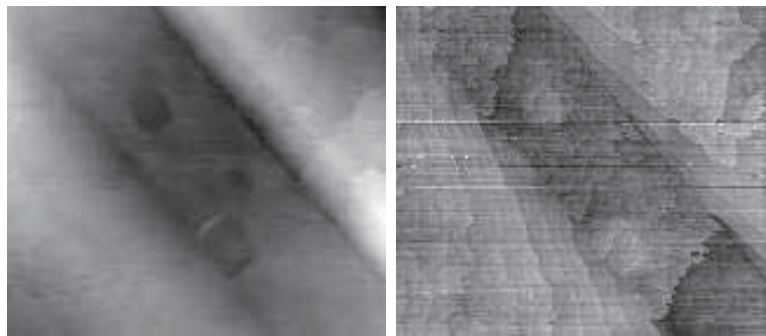


Figure 3.52: Topographic (left hand) and thermal (right hand) image of a part of an integrated circuit.

To investigate the potential of these different approaches, several samples were studied. This included integrated circuits as well as conducting wires on an insulating substrate. The thermal images were taken simultaneously with the topography.

A simple example is shown in the figure 3.52. It is a small part ($30\ \mu\text{m} \times 30\ \mu\text{m}$) of an integrated amplifier. On the left side is the topographic image. Two metallisation lines are crossing the picture. In the thermal image a connection between these lines can be seen in the lower right corner of the image. This is a resistor in the feedback part of the amplifier. A current of about $300\ \mu\text{A}$ is heating up the substrate at the connection point causing a thermal difference against the rest of the substrate.

References

- [1] R.B. Dinwiddie, R.J. Pylkki and P.E. West, *Thermal Conductivity* **22**, 668 (1994)
- [2] A. Majumdar, J.P. Carrejo and J. Lai, *Appl. Phys. Lett.* **62** (20), 2501 (1993)
- [3] A. Majumdar, J. Lai, M. Chandrachood, O. Nakabeppu, Y. Wu and Z. Shi, *Rev. Sci. Instrum.* **66** (6), 3584 (1995)

3.9 Nanostructure fabrication

3.9.1 Nanofabrication of weak links based on scanning force methods

C. Hahn and T. Matsuyama

One of the key elements of superconducting electronics are Josephson junctions which are based on weak links like SNS sandwich structures, proximity effect bridges, point contacts, or variable thickness bridges [1]. Miniaturized weak link structures offer advantages in complex devices where the dimensions have to be small, e. g., dc SQUIDS for magnetic and scanning SQUID microscopes [2-6]. Nanobridges acting as weak links have been fabricated in the past by using electron- beam lithography. They have found applications in dc SQUIDS based either on conventional [7] or high- T_c superconducting materials [8-10]. In the present study we have evaluated the possibility of using scanning force nanofabrication methods for introducing weak links in Nb thin film microbridges produced by conventional photolithography. Variable thickness bridges have been obtained by a mechanical surface modification technique using a scanning force microscope with a diamond probe tip. The weak link behavior of these variable thickness bridges has been tested by low-temperature transport measurements.

Polycrystalline thin films of Nb on Si(100) substrates were prepared by DC magnetron sputtering. The thickness of these films was chosen in the range of 60 - 80 nm. The rms-roughness as measured by SFM was found to be on the order of 1

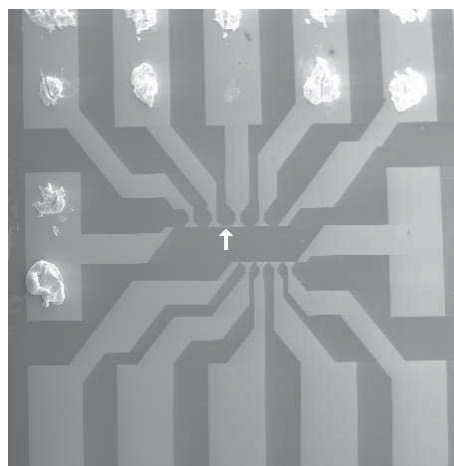


Figure 3.53: Scanning electron micrograph of a photolithographically patterned sample with five Nb microbridges of 20 μm length and five Nb microbridges of 200 μm length (see arrow).



Figure 3.54: Two test patterns written mechanically into a niobium thin film by using an SFM with a diamond tip.

nm over a surface area of about $10 \mu\text{m}^2$. By using conventional photolithography we have prepared samples as shown in Fig. 3.53. They contain five microbridges of 20 nm length, five microbridges of 200 nm length, and contact pads required for the transport measurements.

A scanning force microscope (SFM) based on the laser beam deflection technique was used for imaging as well as for modification experiments. Two different methods were applied for mechanical surface modifications based either on a quasistatic or on a dynamic mode of SFM operation. In the quasistatic mode, the probe tip is moved at high loading force over the sample, thereby scratching the surface. In the dynamic mode, the applied loading force is modulated while the tip is moving which leads to a 'nanohammering'-induced surface modification [11-14]. We have evaluated several different types of cantilevers and probe tips for mechanical surface modifications of

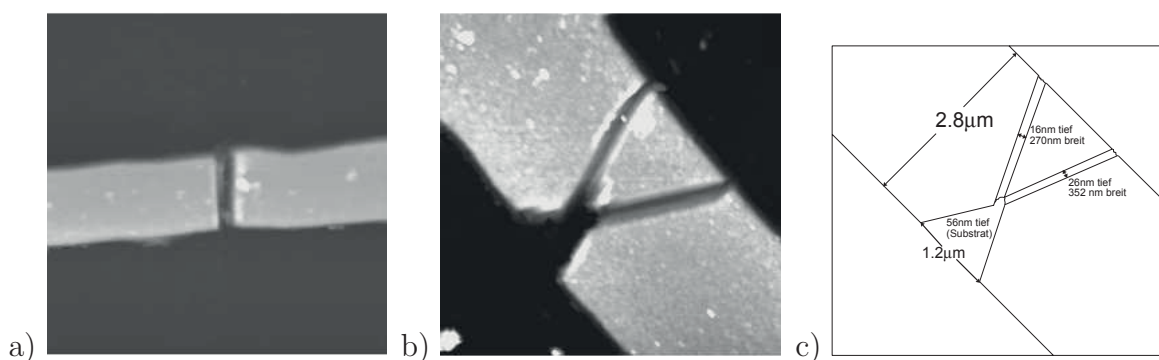


Figure 3.55: a) Nanometer-scale modification of a single Nb microbridge by means of an SFM with a diamond tip in the writing mode. b) Another example of a modified Nb microbridge together with a schematic drawing (c) showing all dimensions.

hard substrates such as niobium. In general, the spring constant has to be sufficiently high (on the order of several hundred N/m). Si_3N_4 - and Si-cantilevers with integrated tips proved to be inappropriate for reliable surface modifications of hard substrates over an extended time period. Tungsten probe tips were found to be more reliable. However, the best results were obtained with CVD-diamond coated Si-cantilevers and with diamond probe tips glued onto SFM cantilevers. In Fig. 3.54 we present two test patterns written mechanically in the quasistatic mode into a niobium thin film by using a diamond tip.

The pattern 'UNI HH' was written with a loading force of 3.8×10^{-4} N and a speed of 100 nm/s. The letters are 2 μm high and are built up by lines of 220 nm width and 2-4 nm depth. The pattern 'Scratch' was written with a loading force of 2.2×10^{-3} N and a speed of 170 nm/s. The letter 't' is 2.5 μm high. The width of the lines is in the range of 300 - 400 nm while their depth is 1.4 - 2.4 nm. The two test patterns clearly demonstrate the reproducibility of the SFM-based mechanical modification process even for hard substrates.

We have subsequently applied the mechanical nanofabrication process based on the quasistatic mode of SFM operation to modify Nb microbridges as presented in Fig. 3.53. The successful fabrication of a variable thickness bridge is demonstrated in Fig. 3.55a. The as-prepared Nb microbridge had a width of 2.4 μm and was 68 - 70 nm thick. By moving the diamond probe tip with a loading force of 1.1×10^{-3} N and a speed of 100 nm/s over the microbridge, about 70 - 80 % of the material was removed on average, leaving a 10 - 20 nm thick nanobridge. Another example of a double bridge structure is presented in Fig. 3.55b. It has been fabricated with a loading force of 1.2×10^{-4} N and a speed of 100 nm/s. The dimensions of this double bridge structure are given in Fig. 3.55c.

In order to test whether the fabricated constriction-type variable thickness bridges show weak link behavior, we have performed low-temperature transport measurements. In particular, we have measured current-voltage-characteristics to determine the critical current as a function of temperature and externally applied magnetic field. The data obtained after the mechanical nanofabrication process were compared with the results for an unmodified microbridge of the same sample. In Fig. 3.56a we present

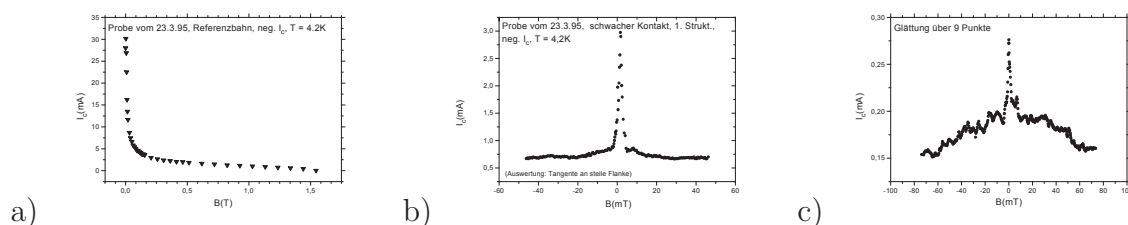


Figure 3.56: a) $I_c(B)$ -curve of a Nb microbridge prior to the mechanical nanofabrication process. b) $I_c(B)$ -curve of the constriction-type variable thickness bridge in Fig. 3.55a. c) $I_c(B)$ -curve of another mechanically modified Nb bridge.

measurements of the critical current I_c as a function of magnetic field B at 4.2 K for an unmodified Nb microbridge. For comparison, the $I_c(B)$ curve of the variable thickness bridge of Fig. 3.55a is presented in Fig. 3.56b. The maximum critical current is 2.98 mA. A contact area of $0.73 \mu\text{m}^2$ and an effective length of 200 nm can be estimated for this particular bridge. There are no modulations visible in the $I_c(B)$ -curve as one would expect in the case of an ideal weak link structure. This is the result of an inhomogeneous current distribution caused by the inhomogeneous structure of the weak link of Fig. 3.55a.

Another example of an $I_c(B)$ measurement on a mechanically modified Nb bridge is presented in Fig. 3.56c. In this case, irregular modulations in the $I_c(B)$ -curve are visible resembling the Fraunhofer pattern expected for an ideal Josephson contact. The contact area is estimated to be 6 nm^2 , while the effective length is on the order of 1 μm . These values are considerably larger compared to those of the Nb bridge shown in Fig. 3.55a.

The $I_c(B)$ data presented in Fig. 3.56 clearly demonstrate that the constriction-type variable thickness bridges fabricated by the SFM in the quasistatic mode exhibit weak link behavior. However, the geometric contact area is still too large compared with the Josephson penetration depth which is about 67 nm in our case. Furthermore, the structural homogeneity of the contacts has to be improved considerably. Further progress is expected by using electron beam lithography instead of photolithography in order to produce superconducting microbridges of considerable smaller width. This will greatly facilitate the SFM-based nanofabrication process because much less material would then have to be removed.

In summary, we have fabricated variable thickness bridges of superconducting Nb thin films by using a combination of conventional photolithography and SFM-based nanofabrication methods. The weak link behavior of such bridges was verified by $I_c(B)$ measurements at low temperatures. Further progress is expected by using SFM nanofabrication methods in combination with electron beam lithography. A direct combination of low-temperature transport measurements and in-situ low-temperature SFM nanomodification of the bridges will further help to tailor their transport properties. Possible applications of miniaturized Josephson junctions include dc SQUIDS for high-resolution magnetic and scanning SQUID microscopy.

References

- [1] K.K. Likharev, Rev. Mod. Phys. 51, 101 (1979)
- [2] R.C. Black, A. Mathai, F.C. Wellstood, E. Dantsker, A.H. Miklich, D.T. Nemeth, J.J. Kingston, and J. Clarke, Appl. Phys. Lett. 62, 2128 (1993)
- [3] R.C. Black, F.C. Wellstood, E. Dantsker, A.H. Miklich, J.J. Kingston, D.T. Nemeth, and J. Clarke, Appl. Phys. Lett. 64, 100 (1994)
- [4] L.N. Vu, M.S. Wistrom, and D.J. Van Harlingen, Appl. Phys. Lett. 63, 1693 (1993)

- [5] L.N. Vu, M.S. Wistrom, and D.J. Van Harlingen, *Physica B* 194-196, 1791 (1994)
- [6] J.R. Kirtley, C.C. Tsuei, J.Z. Sun, C.C. Chi, Lock See Yu-Jahnes, A. Gupta, M. Rupp, and M.B. Ketchen, *Nature* 373, 225 (1995)
- [7] H. Rogalla, B. David, and J. Rhl, *J. Appl. Phys.* 55, 3441 (1984)
- [8] J.R. Wendt, J.S. Martens, C.I.H. Ashby, T.A. Plut, V.M. Hietala, C.P. Tigges, D.S. Ginley, M.P. Siegal, J.M. Phillips, and G.K.G. Hohenwarter, *Appl. Phys. Lett.* 61, 1597 (1992)
- [9] J.R. Wendt, T.A. Plut, R.F. Corless, J.S. Martens. S. Berkowitz, K. Char, M. Johansson, S.Y. Hou, and J.M. Phillips, *J. Vac. Sci. Technol.* B12, 3607 (1994)
- [10] J. Schneider, M. Mück, and R. Wördenweber, *Appl. Phys. Lett.* 65, 2475 (1994)
- [11] T.A. Jung, A. Moser, H.H. Hug, D. Brodbeck, R. Hofer, H.R. Hidber, and U.D. Schwarz, *Ultramicroscopy* 42-44, 1446 (1992)
- [12] W. Allers, C. Hahn, M. Löhndorf, S. Lukas, S. Pan, U.D. Schwarz, and R. Wiesendanger, *Nanotechnology* (in press)
- [13] R. Wiesendanger, *Jpn. J. Appl. Phys.* 34, 3388 (1995)
- [14] C. Hahn, T. Matsuyama, U. Merkt, and R. Wiesendanger, submitted for publication.

3.9.2 Surface modifications of magnetic thin films

M. Löhndorf

The relationship between the surface morphology and the micromagnetic structure is important for understanding macroscopic properties of magnetic materials. Surface defects like impurities and surface cracks strongly influence the distribution of the magnetic stray field of thin magnetic films. Mechanical modifications of surfaces of magnetic materials were used to determine the direction of the magnetization of these materials [1,2]. The lateral dimensions of scratches were in the range from 100 μm to a few millimeters. Scanning tunneling microscopy (STM) opened new possibilities to produce well defined patterns on a much smaller scale. We have used this technique to make surface grooves arranged in different patterns. Local surface modifications have been made by mechanical interaction between the STM tip and the sample surface. Subsequently, changes of the magnetic stray field have been measured by magnetic force microscopy (MFM) [3].

MFM has been used to study domains and domain walls on different types of magnetic materials including soft magnetic samples as, for instance, Garnet or Permalloy [4]. MFM detects the magnetic force exerted on a magnetic probe tip while the tip is scanned over the surface of the sample. To distinguish between the surface morphology and magnetic structure of the sample, first, a topographic scan is obtained with the probe tip in contact with the Permalloy surface. Subsequently, the probe tip is lifted up about 40-80 nm and the same trace is repeated. A single layer or a double layer of Fe has been used as a magnetic coating of our tips. We have magnetized each tip along its axis in a magnetic field of 0.8 Tesla prior to the MFM measurements.

Thin films of Permalloy (81% Ni, 19% Fe) have been chosen for our experiments. We have patterned Permalloy thin films by using a copper grid as a mask with 100

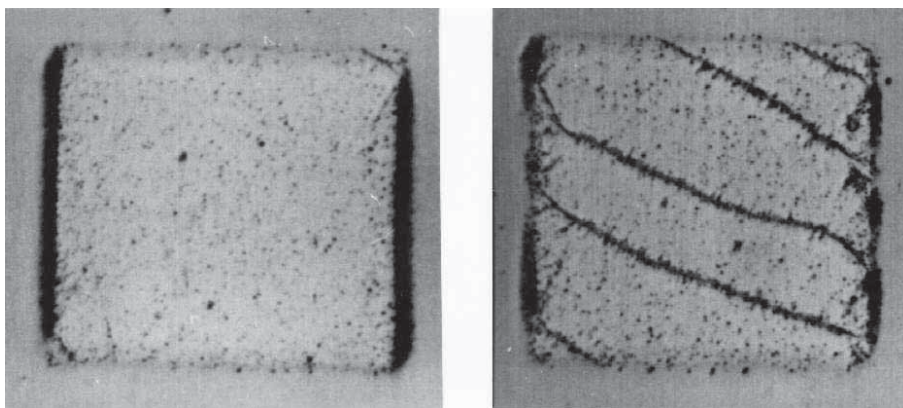


Figure 3.57: Bitter technique images of Permalloy squares with different thicknesses, left 20 nm, right 30 nm.

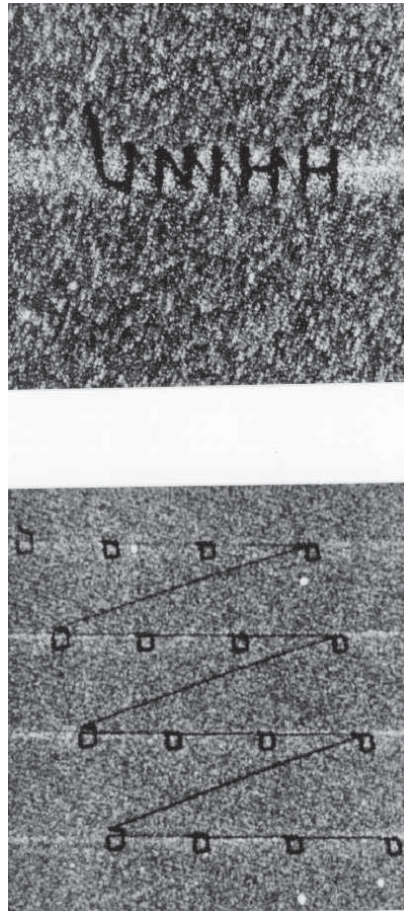


Figure 3.58: STM images of structured Permalloy films. **a** Test pattern (UNI HH), **b** matrix of squares with 400 nm side length.

$\mu\text{m} \times 100 \mu\text{m}$ squares during the evaporation process. In order to characterize the domain structure of our Permalloy samples in the as-prepared state we have used the Bitter technique. Permalloy squares were found to be in a monodomain state for a film thickness of $d = 20 \text{ nm}$ (Fig. 3.57a). Thicker Permalloy films exhibit more complicated domain structures. An example of the domain structure obtained for a Permalloy film with a thickness of $d = 30 \text{ nm}$ is presented in Fig. 3.57b. We have chosen Permalloy films with a thickness of $d = 20 \text{ nm}$ for our experiments to avoid an influence of the magnetic strayfield from pre-existing domain walls with the stray field originating from our local surface modifications.

The surface modifications of the Permalloy films have been performed by STM. Two examples of surface modifications of thin Permalloy films are shown in Fig. 3.58. The first image shows the letters “UNI HH” written onto the Permalloy film by using a tungsten tip and the second one shows a matrix of squares ($400 \text{ nm} \times 400 \text{ nm}$) with a lateral spacing of $2 \mu\text{m}$. The width of the grooves of the fabricated structures is about 100 nm and the depth is about 3-5 nm. The smallest width we achieved so far

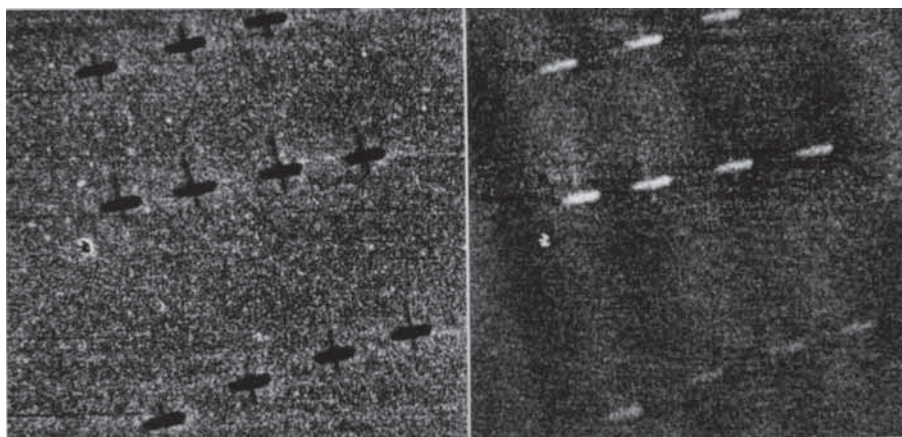


Figure 3.59: Topographic and the corresponding MFM image of an array of crosses. Scan size $7.25 \mu\text{m} \times 7.25 \mu\text{m}$.

was on the order of 70-80 nm.

The topographic and the corresponding MFM image of an array of crosses is shown in Fig. 3.59 with a width of the grooves of 175 nm, a length of 650 nm and a depth of 6 nm. The MFM contrast is enhanced for grooves orientated in the horizontal direction, whereas for the orthogonal direction no measurable magnetic contrast is observed.

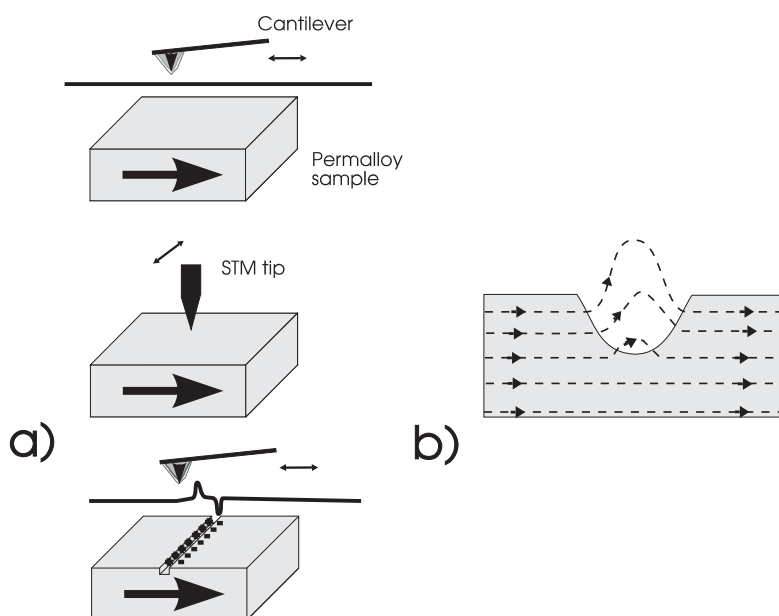


Figure 3.60: **a** Schematic drawing explaining the principle of our experiment: Local topographic modifications are produced by an STM tip. If the scratches are orientated perpendicular to the magnetization direction, magnetic charges are accumulated at the sides of the scratch, leading to a magnetic stray field (see Fig. **b**).

Our explanation of this observation is illustrated in Fig. 3.60. If a surface scratch is orientated perpendicular to the magnetization vector of the monodomain Permalloy sample, magnetic charges are accumulated at the sides of the scratch. To minimize the magnetic energy of the sample, the magnetic flux is closed. As a result, the distribution of the magnetic stray field is changed locally which can be detected by the MFM.

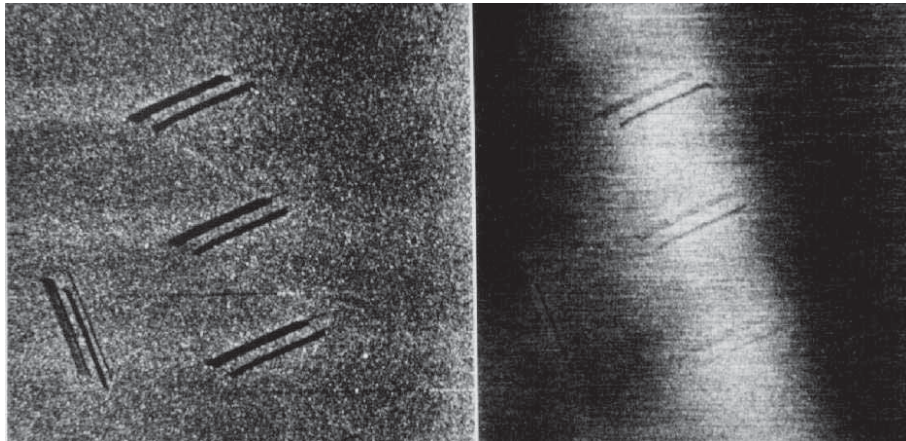


Figure 3.61: Topographic and MFM image of a written test pattern consisting of double grooves orientated in two orthogonal directions. Scan size $7.25 \mu\text{m} \times 7.25 \mu\text{m}$.

If a scratch is aligned parallel to the magnetization direction then magnetic charges will not appear on the sides of the scratch and therefore no magnetic stray field will emerge. The difference in the magnetic contrast between the lower and the upper part of the MFM image in Fig. 3.59 is due to a change of the magnetic probe tip. The magnetization direction of the magnetic tips is not fixed and can be altered by touching some surface features, even if the tip is magnetized in a strong magnetic field prior to the measurement. Fig. 3.61 shows the simultaneously obtained MFM and topographic image of a double groove test pattern. A magnetic stray field was measured above the scratches in the middle part of the imaged area, while from the perpendicularly orientated scratches no significant magnetic signal appeared. In contrast to the crosses in Fig. 3.59 the magnetic signal is distributed over a larger area.

In Fig. 3.62 the magnetic stray field distribution from a fabricated square of $4 \mu\text{m}$ side length was imaged by MFM. The detected magnetic contrast inside the square seems to originate from small domains formed by internal stress or strain resulting from the mechanical modifications. For evaporated Permalloy films with negative magnetostriction, it has been found that cross walls occur on scratches in the easy direction of magnetisation. The kind of walls which can occur depends on the size of the scratch [5,6].

Our results led to the distinction of two different types of mechanism causing a measurable magnetic stray field. In one case the magnetic signal seems to originate directly from surface scratches (Fig. 3.59), while in the other case the detected magnetic signal was distributed over a larger area (Fig. 3.61 and Fig. 3.62) due to the

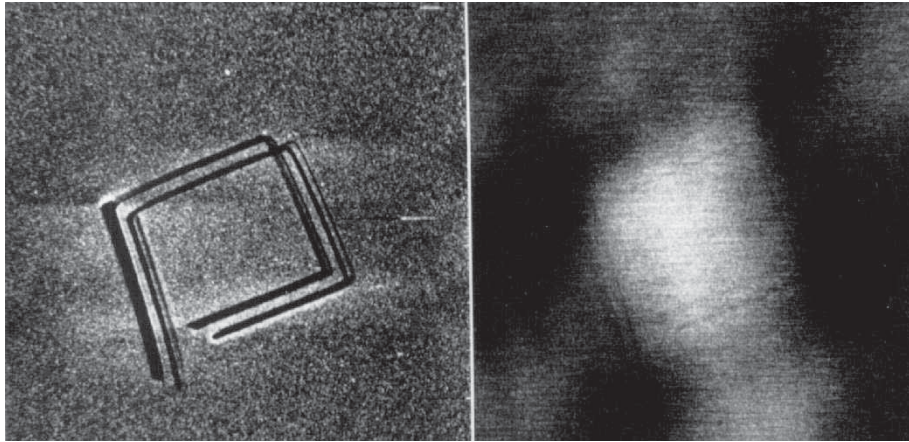


Figure 3.62: Topographic and MFM image of a square with 4 μm side length.

formation of small domains. Future investigations will focus on the influence of the shape of the surface scratches on the magnetic stray field distribution and a comparison with theoretical simulations. For further experimental details see Ref. [7]

References

- [1] H. J. Williams, *Phys. Rev.* **71**, 646 (1947).
- [2] H. J. Williams, R. M. Bozorth, and W. Shockly, *Phys. Rev.* **75**, **155** (1949).
- [3] Y. Martin, H. K. Wickramasinghe, *Appl. Phys. Lett.* **50**, 1455 (1987).
- [4] A. Wadas, J. Moreland, R. R. Katti, and P. Rice, *Appl. Phys. Lett.*, **64**, 1156 (1994)
- [5] S. Methfessel, S. Middlehoek and H. Thomas, *IBM J. Res. Develop.* **4**, 96 (1960).
- [6] R. F. Soohoo, *Magnetic thin films*, Harper & Row (1965).
- [7] M. Löhndorf and R. Wiesendanger, *Appl. Phys. A* **61**, 93 (1995).

3.9.3 Local charge modifications of nitride-oxide-silicon heterostructures

M. Dreyer and A. Born

Nitride-oxide-silicon (NOS) heterostructures provide interesting model systems for charge storage [1-3], leading to a spatially varying capacitance signal as measured by means of a sharp metal probe being scanned in close proximity to the top nitride layer. The substrates of the NOS heterostructures consisted of p-doped Si (100) wafers with a resistivity of 10-20 mΩcm, on which a tunnel oxide of varying thickness (5.1 nm, 6.6 nm, and 8.2 nm) has been grown. Finally, a 52-53 nm thick nitride layer has been deposited on top.

If a metal electrode is brought in contact with the top nitride layer of the NOS heterostructure (Fig. 3.63), a metal-insulator-silicon (MIS) diode is formed. The capacitance C of such a device is a function of the bias voltage U applied to the silicon substrate as shown in chapter 3.7.

NOS heterostructures have been considered as charge storage devices for a long time (see e.g. [3]): When applying a voltage pulse between the top metal electrode and the silicon substrate, electrons can tunnel through the oxide layer leaving holes behind. This charge carrier separation leads to an additional electrical voltage across the NOS structure and can be detected capacitively by measuring C or dC/dU at an appropriate fixed value of the externally applied bias voltage, as shown below. Depending on the oxide thickness, which should be not too small and homogeneous, the separated charge remains stable for many years. By applying a voltage pulse of opposite polarity, however, the stored charge can be erased which is an attractive feature for memory applications.

If the top electrode is a metallized sharp probe tip as used for atomic force mi-

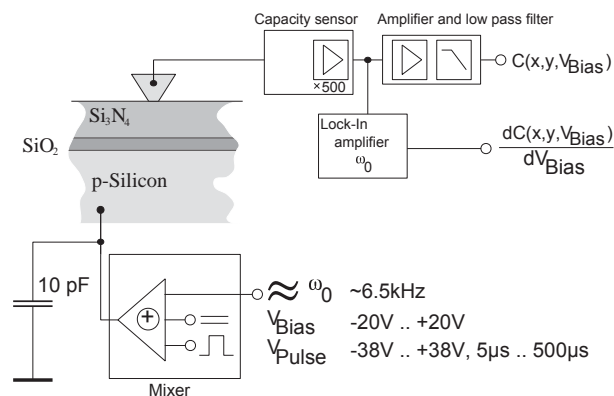


Figure 3.63: Schematic drawing of the NOS heterostructure in contact with a metal probe tip and the capacitance detection circuitry.

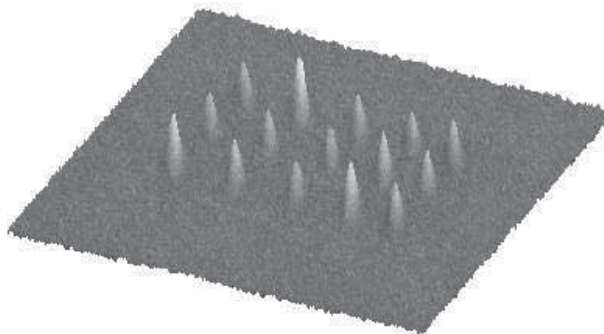


Figure 3.64: Perspective dC/dU -image ($15 \times 15 \mu\text{m}^2$) of a 5×3 array of charge bits which were written by applying -35 V pulses of $40 \mu\text{s}$ width between the metal tip and the silicon substrate of the NOS heterostructure with an oxide thickness of 5.1 nm . No features appeared in the corresponding topographic image.

scopy (AFM), ultra-high density storage devices may be realized [1,2]. Read-out is achieved by combining a capacitance sensor with a standard AFM instrument to obtain a scanning capacitance microscope (SCM). Assuming a contact area of $A = 1 \mu\text{m}^2$ and a thickness of the insulating layer of $d = 55 \text{ nm}$, the capacitance C_I is on the order of 1 fF . If the contact area is further reduced to the nanometer-scale regime, C_I is only on the order of aF (10^{-18} F).

For capacitance measurements we have initially used home-made tungsten cantilevers cut from $5\text{-}\mu\text{m}$ -thick tungsten foil and electrochemically etched to obtain sharp probe tips as mentioned in chapter 3.7.

By applying voltage pulses between the metal tip and the silicon substrate, we succeeded in charge separation by tunneling through the oxide layer. The patterns of stored charge bits have subsequently been imaged with the SCM. An example is presented in Fig. 3.64, where a 5×3 array of charge bits is visible which was written with -35 V pulses of $40 \mu\text{s}$ width.

The size of the written charge bits, as they appear in the SCM images, depends mainly on three parameters [4]:

- The contact area between the metal tip and the NOS heterostructure which determines the degree of charge localization during the writing process as well as the contour profile of the charge bits during the SCM imaging (read-out) process.
- The parameters for the voltage pulses (height and width) which determine how much charge can actually tunnel through the oxide layer. Fig. 3.65 shows a series of charge bits written with variable pulse parameters, but with the same SCM tip. The size of the charge bits varies considerably.
- The chosen value of the applied bias voltage during SCM imaging which has also

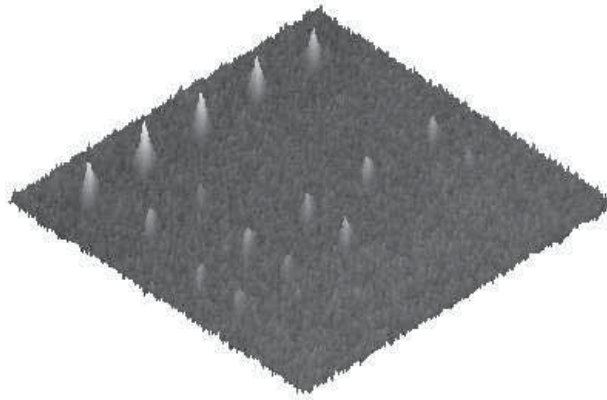


Figure 3.65: Perspective dC/dU -image of an array of charge bits which were written with voltage pulses of variable height and width. Upper two rows: pulse height of -38 V, pulse width varied between $100 \mu\text{s}$ and $20 \mu\text{s}$; lower two rows: pulse height of -35 V, pulse width varied between $100 \mu\text{s}$ and $40 \mu\text{s}$. For this series of charge modifications the NOS heterostructure with an oxide thickness of 6.6 nm has been used.

great influence on the apparent size of the charge bits as will be discussed below.

To extract more information about the characteristics of the stored charge bits, we have performed scanning capacitance spectroscopy (SCS) studies, i.e. we have investigated the bias-dependence of the dC/dU signal as a function of the spatial coordinates (x, y) . In Fig. 3.66, we present SCS data ($dC/dU [x,U]$) measured over three previously written charge dots. The data is shown in a top-view (left) as well as in a perspective view (right). The information content of such maps is extremely high because both the spatial as well as the bias-dependence of the dC/dU -signal

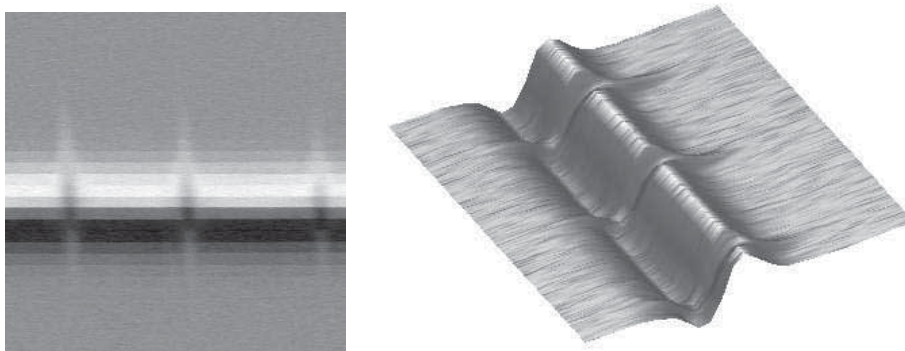


Figure 3.66: Top-view of a scanning capacitance spectroscopy (dC/dU) image of three previously written charge dots (pulse height: -35 V, pulse widths: $100 \mu\text{s}$, $80 \mu\text{s}$ and $60 \mu\text{s}$ from bottom to top). The applied bias voltage has been varied along the horizontal axis whereas the vertical axis represents the spatial (x -) coordinate. The plot to the right shows a perspective view of the same spectroscopic SCM data.

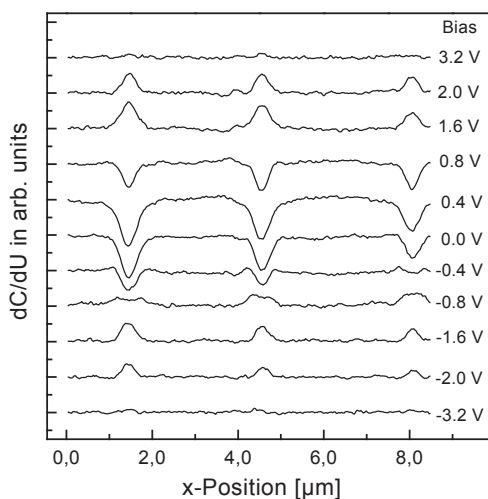


Figure 3.67: Individual section lines across the data shown in Fig. 3.66 at several different values of (fixed) bias voltage U .

is presented simultaneously. To discuss the information content of this data, it is therefore advantageous to plot section lines at fixed bias voltage (Fig. 3.67) separately.

In Fig. 3.67 we present $dC/dU(x)$ curves for several different values of the applied bias voltage U . It is obvious that the apparent size of the charge dots, as imaged with the SCM, depends critically on the chosen U -value. Therefore, it is not useful to provide numbers for the size of the written charge bits without specifying the bias voltage used for imaging (read-out). If the applied bias voltage is chosen too high, the written charge dots are not showing up at all in the dC/dU image.

As a next step we are going to use a commercial capacitance sensor from JVC, reaching a higher sensitivity. Instead of the tungsten foil cantilevers metal coated silicon nitride cantilevers will be used as a probe, leading to an improved lateral resolution.

References

- [1] R. C. Barrett and C. F. Quate, *J. Appl. Phys.* **70**, 2725 (1991).
- [2] R. C. Barrett and C. F. Quate, *Ultramicroscopy* **42-44**, 262 (1992).
- [3] S. Iwamura, Y. Nishida, and K. Hashimoto, *IEEE Trans. on Elec. Dev.* ED-28, 854 (1981).
- [4] M. Dreyer and R. Wiesendanger, *Appl. Phys.* **A61**, 357 (1995)

Chapter 4

Collaborations

4.1 Research Partners

- MARCH, Hamburg:
Prof. M. Harsdorff, Prof. D. Heitmann, Prof. J. Kötzler,
Prof. U. Merkt, Dr. F. Goerke, Dr. T. Matsuyama
- HASYLAB, Hamburg:
Prof. R. J. Johnson
- Institute for Physical Chemistry, University of Hamburg:
Prof. H. Weller, Prof. C. Benndorf
- Institute for Inorganic and Applied Chemistry, University of Hamburg:
Prof. A. Reller
- Philips Forschung, Hamburg:
Dr. J.-P. Krumme
- Beiersdorf AG, Hamburg:
Dr. D. Emeis
- University of Kiel:
Prof. R. Knöchel, Prof. Skibowski
- Fraunhofer Institut für Schicht- und Oberflächentechnologie, Braunschweig:
Prof. D. Dimigen
- MPI for Microstructure Physics, Halle:
Dr. K.-P. Meyer
- Forschungszentrum Jülich
Dr. S. Blügel

- Hahn-Meitner-Institut, Berlin
Dr. S. Klaumünzer
- IFW Dresden:
Dr. G. Reiss
- University of Münster:
Prof. H. Fuchs
- University of Saarbrücken:
Prof. U. Hartmann
- University of Göttingen
Prof. H. C. Freyhardt
- Siemens, Erlangen:
Dr. H. A. M. van den Berg
- GSI Darmstadt:
Prof. R. Neumann
- EPF Lausanne, Switzerland:
Prof. F. Lévy
- University of Nijmegen, The Netherlands:
Prof. H. van Kempen, Prof. R. A. de Groot
- Dept. for Physical and Macromolecular Chemistry, University of Leiden, The Netherlands:
Dr. W. Sager
- Philips Research, Eindhoven, The Netherlands:
Dr. H. W. van Kesteren, Dr. R. M. Wolf
- University of Namur, Belgium:
Prof. J.-J. Pireaux, Dr. G. Gensterblum
- University of Dublin, Trinity College, Ireland:
Prof. J. M. D. Coey, Dr. I. V. Shvets
- Institute of Chemical Technology, Prague, Czech Republic:
Prof. P. Novotny
- Institute of Physics, Polish Academy of Sciences, Warsaw, Poland:
Prof. J. Rauluszkiewicz
- Institute of Molecular Physics, Polish Academy of Sciences, Nauk, Poland:
Prof. L. Szczesniak

- Institute of Chemistry, University of Sofia, Bulgaria:
Prof. D. Drakova
- Ukrainian Academy of Sciences, Kiev, Ukraine:
Prof. S. Nepijko
- Beijing Laboratory of Vacuum Physics, P. R. China:
Prof. S. Pang
- NTT Japan:
Dr. Y. Maeda
- IBM Almaden, San José, USA:
Dr. D. Weller

4.2 Industrial Partners

- Philips Semiconductors, Hamburg
- Siemens, Erlangen
- IBM Deutschland Speichersysteme, Mainz
- OMICRON Vakuumphysik, Taunusstein
- Nanosensors, Aidlingen

Chapter 5

Theses

5.1 Diploma Theses

1. Markus Löhndorf (1994):
Untersuchungen von dünnen $\text{YBa}_2\text{Cu}_3\text{O}_{7-x}$ -Schichten mittels Rastersonormethoden und Aufbau eines Rastertunnelmikroskops.
2. Wolf Allers (1994):
Untersuchungen von C_{60} -Filmen auf Germaniumsulfid mittels Rasterkraft- und Reibungskraftmikroskopie und Entwicklung eines Rasterkraftmikroskops.
3. Slavomir Lukas (1994):
Nanostrukturierung mittels Rastersonormethoden.
4. Alexander Schwarz (1994):
Untersuchung von Übergangsmetalloxiden mittels der Rasterkraftmikroskopie und Aufbau eines faseroptischen, interferometrischen Detektionssystems für ein Rasterkraftmikroskop.
5. Christian Wittneven (1994):
Aufbau eines tunnelstabilisierten Magnetkraftmikroskops für den Betrieb im Hochvakuum und Untersuchung von Bariumferrit.
6. Carsten Oldorf (1994):
Aufbau eines Rastersondenmikroskops für Rastertunnelmikroskopie und tunnelstabilisierte Magnetkraftmikroskopie.
7. Michael Dreyer (1995):
Aufbau eines Rasterkapazitätsmikroskops und Einsatz von Rastersondenmethoden zur elektronischen Strukturierung.

8. Bernd Zenker (1995):
Aufbau eines Rastertunnelmikroskops und Untersuchungen von Silizium-(100)-Oberflächen mittels Rasterkraftmikroskopie.
9. René Pascal (1995):
Rastertunnelmikroskopische Studie der Wolfram-(110)-Oberfläche auf atomarer Skala.
10. Cathérine Hahn (1995):
Nanostrukturierung und Charakterisierung von Mikrobrücken aus Niob.
11. Peter Köster (1995):
Untersuchungen zur quantitativen Reibungskraftmikroskopie.
12. Martina Seider (1995):
Untersuchung von Teilchenspuren schwerer Ionen in Schichtstrukturen mittels Rastersondormethoden.

Diploma Theses (started)

1. Jörn Asmussen:
Rasterthermomikroskopie.
2. Christian Witt:
Aufbau eines UHV-Rastertunnelmikroskops und Untersuchungen des Wachstums dünner metallischer Filme.
3. Axel Born:
Nanostrukturierung mittels eines Rasterkapazitätsmikroskops.
4. Martin Winzer:
Nanokugellithographie.
5. Hendrik Hölscher:
Theorie der Reibungskraftmikroskopie.
6. Sven Hanszen:
Rastersondenmikroskopie an Emulsionen.
7. Jens Müller:
Aufbau eines Rasterkraftmikroskops.

8. Oliver Zwörner: Reibungskraftmikroskopie an verschiedenen Kohlenstoffverbindungen.
9. Wolfgang Kresse:
Rastertunnelmikroskopie an Verbindungshalbleitern.
10. Christoph Zarnitz:
Rastertunnelmikroskopie an ultradünnen magnetischen Filmen.
11. Stefan Heinze:
Spinaufgelöste Elektronenstrukturberechnungen zur Interpretation von RTM-Daten an dünnen magnetischen Filmen.

5.2 Ph. D. Theses

1. Hendrik Bluhm:
Rasterkraftmikroskopie mit piezoresistiven Kraftsensoren und Anwendung der Rasterkraftmikroskopie auf Ferroelektrika.
2. Matthias Bode:
Untersuchung der atomaren, elektronischen und magnetischen Struktur ultradünner Eisenfilme mittels UHV-Rastertunnelmikroskopie und -spektroskopie.
3. Markus Löhndorf:
Untersuchung mikromagnetischer Strukturen in dünnen magnetischen Filmen und Multilagenn mittels Magnetkraftmikroskopie.
4. Wolf Allers:
Tieftemperatur-Rasterkraftmikroskopie und Reibungskraftmikroskopie.
5. Alexander Schwarz:
Tieftemperatur-Rasterkraftmikroskopie und Untersuchungen von Nanopartikeln.
6. Christian Wittneven:
Tunnelstabilisierte Magnetkraftmikroskopie bei tiefen Temperaturen.
7. Ralph Dombrowski:
Tieftemperatur-Rastertunnelmikroskopie und -spektroskopie an magnetischen Systemen.

8. René Pascal:

UHV-Rastertunnelmikroskopie und -spektroskopie an in-situ präparierten, epitaktisch gewachsenen magnetischen Schichten.

9. Michael Dreyer:

Rasterkapazitätsmikroskopie und -spektroskopie an Halbleiterheterostrukturen und -bauelementen.

Chapter 6

Scientific Publications

6.1 Books

1. R. Wiesendanger, *Scanning Probe Microscopy and Spectroscopy: Methods and Applications*, Cambridge University Press, Cambridge 1994.
2. H.-J. Güntherodt and R. Wiesendanger (eds.), *Scanning Tunneling Microscopy I: General Principles and Applications to Clean and Adsorbate-Covered Surfaces*, Springer Series in Surface Sciences, Vol. 20, Springer Berlin, Heidelberg, 2nd edition 1994.
3. R. Wiesendanger and H.-J. Güntherodt (eds.), *Scanning Tunneling Microscopy II: Further Applications and Related Scanning Techniques*, Springer Series in Surface Sciences, Vol. 28, Springer Berlin, Heidelberg, 2nd edition 1995.
4. R. Wiesendanger and H.-J. Güntherodt (eds.), *Scanning Tunneling Microscopy III: Theory of STM and Related Scanning Probe Methods*, Springer Series in Surface Sciences, Vol. 29, Springer Berlin, Heidelberg 1993.

6.2 Book Contributions and Review Articles

1. R. Wiesendanger, in: *Magnetism and Structure in Systems of Reduced Dimensions*, ed. by R. F. C. Farrow, B. Dieny, M. Donath, B. D. Hermsmeier, and A. Fert, NATO ASI Series, Plenum Press, New York 1993: “Magnetic-sensitive scanning probe microscopy”.
2. R. Wiesendanger, in: *Atomic and Nanometer-Scale Modification of Materials: Fundamentals and Applications*, ed. by P. Avouris, NATO ASI Series E: Appl.Sci. Vol. 239, Kluwer Academic Publishers, Dordrecht 1993: “Atomic-scale imaging and modification of spins using a magnetic-sensitive scanning tunneling microscope”.

3. R. Wiesendanger, in: *The Technology of Proximal Probe Lithography*, ed. by C. R. K. Marrian, SPIE Optical Engineering Press, Bellingham 1993: "Nanofabrication by scanning probe instruments: methods, potential applications and key issues".
4. R. Wiesendanger, *Solid State Phenom.* **35-36**, 281 (1994): *Contributions of Scanning Probe Microscopy and Spectroscopy to the Investigation of Microstructures and Their Physical Properties.*
5. R. Wiesendanger, *J. Magn. Soc. Jpn.* **18**, 4 (1994): *Spin-polarized Scanning Tunneling Microscopy: Gateway to Imaging and Modification of Surface Spin Configurations at the Atomic Level.*
6. R. Wiesendanger, *J. Vac. Sci. Technol. B* **12**, 515 (1994): *Contributions of Scanning Probe Microscopy and Spectroscopy to the Investigation and Fabrication of Nanometer-Scale Structures.*
7. R. Wiesendanger, *Jpn. J. Appl. Phys.* **34**, 3388 (1995): *Recent Advances in Nano-Structural Investigations and Modifications of Solid Surfaces by Scanning Probe Methods.*
8. R. Wiesendanger, *Physik in unserer Zeit* **5**, 206 (1995): *Physik in unserer Zeit auf der Nanometerskala.*
9. R. Wiesendanger, in: *Trends in Sensor Technology/Sensor Market*, Sensors Vol. 8, ed. by R. Jones and H. Meixner, VCH 1995: "Future Nanosensors".
10. R. Wiesendanger, in: *Procedures in Scanning Probe Microscopies*, ed. by R. Colton, A. Engel, J. Frommer, H. Gaub, A. Gewirth, R. Guckenberger, W. Heckl, B. Parkinson, and J. Rabe, John Wiley & Sons Ltd. 1995: "Surface Modification".
11. R. Wiesendanger, in: *Physics and Chemistry of Low Dimensional Inorganic Conductors*, ed. by J. Dumas, NATO ASI Series B: Physics, Plenum: "STM and AFM on CDW and related materials".
12. R. Wiesendanger, in: *Handbook of Microscopy*, ed. by S. Amelinckx, D. Van Dyck, J. Van Landuyt and G. Van Tendeloo, VCH 1995: "Scanning Tunneling Microscopy".
13. U. D. Schwarz, in: *Handbook of Microscopy*, ed. by S. Amelinckx, D. Van Dyck, J. Van Landuyt and G. Van Tendeloo, VCH 1995: "Scanning Force Microscopy".
14. A. Wadas, in: *Handbook of Microscopy*, ed. by S. Amelinckx, D. Van Dyck, J. Van Landuyt and G. Van Tendeloo, VCH 1995: "Magnetic Force Microscopy".

15. U. D. Schwarz, H. Bluhm, H. Hölscher, W. Allers, and R. Wiesendanger, in: *The Physics of Sliding Friction*, ed. by B. N. J. Persson, NATO ASI Series, Kluwer, Dordrecht, 1996: "Friction in the Low-Load Regime: Studies on the Pressure and Direction Dependence of Frictional Forces by Means of Friction Force Microscopy".

6.3 Original Publications

1. R. Wiesendanger, I. V. Shvets, and J. M. D. Coey, *J. Vac. Sci. Technol. B* **12**, 2118 (1994): *Wigner glass on the magnetite (001) surface observed by scanning tunneling microscopy with a ferromagnetic tip.*
2. W. Allers, U. D. Schwarz, G. Gensterblum, and R. Wiesendanger, *Appl. Phys. A* **59**, 11 (1994): *Scanning and friction force microscopy of thin C₆₀ films on GeS(001).*
3. M. Löhndorf, F. Goerke, U. Merkt, and R. Wiesendanger, *Appl. Phys. A* **59**, 57 (1994): *Growth stages of YSZ buffer layers and YBa₂Cu₃O_{7-x} thin films on silicon substrates studied by scanning probe microscopy.*
4. A. Schwarz, U. D. Schwarz, H. Bluhm, and R. Wiesendanger, *Surf. and Interf. Anal.* **23**, 409 (1995): *Determination of small crystallites from scanning force microscopy angle measurements.*
5. M. Löhndorf and R. Wiesendanger, *Appl. Phys. A* **61**, 93 (1995): *MFM study of magnetic stray field effects due to mechanical surface modifications of patterned permalloy thin films.*
6. M. Dreyer and R. Wiesendanger, *Appl. Phys. A* **61**, 357 (1995): *Scanning capacitance microscopy and spectroscopy: Applications in semiconductor device characterization and storage technology.*
7. S. A. Nepijko and R. Wiesendanger, *Europhys. Lett.* **31**, 567 (1995): *Size dependence of the Curie temperature of separate nickel particles studied by interference electron microscopy.*
8. U. D. Schwarz, W. Allers, G. Gensterblum, J.-J. Pireaux, and R. Wiesendanger, *Phys. Rev. B* **52**, 5967 (1995): *Growth of C₆₀ thin films on GeS(001) studied by scanning force microscopy.*
9. U. D. Schwarz, W. Allers, G. Gensterblum, and R. Wiesendanger, *Phys. Rev. B* **52**, 15 Nov. 1995 (in press): *Low-load friction behaviour of epitaxial C₆₀ monolayers under Hertzian contact.*

10. W. Allers, U. D. Schwarz, G. Gensterblum, and R. Wiesendanger, *Z. Phys. B.* **99**, 1 (1995): *Low-load friction behavior of epitaxial C₆₀ monolayers.*
11. H. Bluhm, U. D. Schwarz, K.-P. Meyer, and R. Wiesendanger, *Appl. Phys. A* **61**, 525 (1995): *Anisotropy of sliding friction on the triglycine sulfate (010) surface.*
12. M. Bode, R. Pascal, and R. Wiesendanger, *Surf. Sci.* (in press): *STM study of carbon-induced reconstructions on W(110): Strong evidence for a surface lattice deformation.*
13. M. Bode, R. Pascal, and R. Wiesendanger, *Z. Phys. B* (in press): *Imaging and tunneling spectroscopy of individual iron adsorbates at room temperature.*
14. M. Bode, R. Pascal, and R. Wiesendanger, *Z. Phys. B* (in press): *Distance-dependent STM study of the lateral resolution on metal surfaces.*
15. A. Wadas, R. Wiesendanger, and P. Novotny, *J. Appl. Phys.* (in press): *Bubble domains in garnet films studied by magnetic force microscopy.*
16. M. Löhndorf, A. Wadas, R. Wiesendanger, and H. W. van Kesteren, *J. Vac. Sci. Technol. B: Domain Structure of Co/Pt Multilayers studied by Magnetic Force Microscopy.*
17. H. Bluhm, R. Wiesendanger, and K.-P. Meyer, *J. Vac. Sci. Technol. B: Surface structure of ferroelectric domains on the triglycine sulfate (010) surface.*
18. R. Wiesendanger, M. Bode, R. Pascal, W. Allers, and U. D. Schwarz, *J. Vac. Sci. Technol.:* *Issues in atomic-resolution structure and chemical analysis by scanning probe microscopy and spectroscopy.*
19. W. Allers, C. Hahn, M. Löhndorf, S. Lukas, S. Pan, U. D. Schwarz, and R. Wiesendanger, *Nanotechnology: Nanomechanical investigations and modifications of thin films based on scanning force methods.*
20. N. Diekmann, R. Kirsten, M. Löhndorf, and A. Bock, *Physica C* **245**, 212 (1995): *Epitaxial quality of c-axis and a-axis orientated YBaCuO films, Characterization by Raman Spectroscopy.*
21. M. Löhndorf, A. Wadas, H. A. M. van den Berg, and R. Wiesendanger, (submitted): *Structure of cross-tie wall in thin Co films resolved by magnetic force microscopy.*
22. M. Seider, U. D. Schwarz, and R. Wiesendanger, (submitted): *Load-dependent topographic and friction studies of individual ion tracks in layered materials by scanning and lateral force microscopy.*

23. C. Hahn, T. Matsuyama, U. Merkt, and R. Wiesendanger, (submitted): *Nanofabrication of weak links based on scanning force methods.*
24. M. Bode, R. Pascal, and R. Wiesendanger, (submitted): *Nanostructural and local electronic properties of Fe/W(110) correlated by scanning tunneling spectroscopy.*

Chapter 7

Talks

7.1 Invited Talks

- 08.01.93:** R. Wiesendanger. Bad Honnef, Germany (Dreikönigstreffen Oberflächenmagnetismus): *Spinempfindliche Rastertunnelmikroskopie: Stand und Perspektiven*
- 23.03.93:** R. Wiesendanger. Freiburg i. Br., Germany (Waldhoftagung): *Von der atomaren Abbildung zu atomaren Datenspeichern und Bauelementen: Zukunftsperspektiven der Rastertunnel- und Rastersensormikroskopie*
- 24.05.93:** R. Wiesendanger. Jaszowiec, Poland (XXII Int. School on Physics of Semiconducting Compounds): *Scanning Tunneling Microscopy*
- 01.09.93:** R. Wiesendanger. Szelmant, Poland (Workshop on Physics of Ultrathin Magnetic Films): *Scanning tunneling microscopy with ferromagnetic probe tips*
- 07.09.93:** R. Wiesendanger. Wien, Österreich (ICTF-9): *Contributions of Scanning Probe Microscopy and Spectroscopy to the Investigation and Fabrication of Nanostructures*
- 11.09.93:** R. Wiesendanger. Tokyo, Japan (Domestic conference of Magnetism Society of Japan): *Spin-sensitive Scanning Tunneling Microscopy*
- 15.12.93:** R. Wiesendanger. Dresden, Germany (1. Dresdner Sensor-Symposium): *Sensorik im Nanometerbereich: Rasterverfahren zur Abbildung und Strukturierung*
- 15.03.94:** R. Wiesendanger. Rottach-Egern, Germany (Int. Symp. on Artificially Structured Materials and Biomimetics): *Atomic and Nanometer-Scale Modification of Materials by Scanning Probe Methods*
- 06.06.94:** R. Wiesendanger. Keauhou-Kona, Hawaii, USA (Conference on Ordered Molecular and Nanoscale Electronics): *Nanoengineering based on local probe*

methods: mechanical, electronic, thermal and magnetic manipulations of matter at the nanometer scale

- 09.12.94:** R. Wiesendanger. Kanazawa, Japan (2nd Int. Coll. STM): *Recent Advances in Nano-Structural Investigations and Modifications of Solid Surfaces by Scanning Probe Methods*
- 12.12.94:** R. Wiesendanger. Tokyo, Japan (Workshop on Spin-STM): *Spin-Polarized Scanning Tunneling Microscopy and Spectroscopy: Concept, Potential Applications, and Key Issues*
- 20.12.94:** R. Wiesendanger. University of Warwick (IOP Conference): *High Resolution Magnetic Imaging by Scanning Probe Microscopy*
- 17.02.95:** R. Wiesendanger. Freiburg i.Br., Germany (Nanoscope User Meeting): *Nanomechanische Eigenschaften und Strukturierung von dünnen Filmen mittels eines Rasterkraftmikroskops*
- 27.03.95:** R. Wiesendanger. Helsinki, Finland (Seminar on Scanning Probe Techniques in Surface Engineering): *Nanostructural Investigations and Modifications of Solid Surfaces by Scanning Probe Microscopy and Spectroscopy*
- 09.05.95:** R. Wiesendanger. Niedernhausen, Germany (OMICRON User Meeting): *Micro- and Nanostructural Investigations of Magnetic Systems by UHV-STM and SFM Methods*
- 20.06.95:** R. Wiesendanger. Les Houches, France (NATO School on Physics and Chemistry of Low Dimensional Inorganic Conductors): *Scanning tunneling and atomic force microscopy on CDW and related materials*
- 22.06.95** U. D. Schwarz, W. Allers, G. Gensterblum, and R. Wiesendanger. Trieste, Italy (Adriatico Research Conference on Physics of Sliding Friction, NATO ASI Series): *Low-load friction behavior of epitaxial C₆₀ monolayers under Hertzian contact*
- 02.07.95:** R. Wiesendanger. Uppsala, Sweden (Summer School on Modern Characterization Techniques for Thin Molecular Films and Immobilized Biomolecules): *Scanning Probe Microscopy and Spectroscopy: Experimental Methods and Applications to Thin Molecular Films*
- 14.09.95:** R. Wiesendanger. Leipzig, Germany (DGE'95-Meeting): *Wechselwirkung von Oberflächen mit lokalen Sonden: Neue Wege der Nanostrukturierung*
- 21.09.95:** R. Wiesendanger. Leoben, Austria (ÖPG'95): *Rastersondenmikroskopie und Spektroskopie: Zugang zur Physik auf der Nanometerskala*

02.10.95: R. Wiesendanger. Rottach-Egern, Germany (Workshop on New Developments in the Physics of Low-Dimensional Systems): *Spektroskopie an einzelnen Atomen und Clustern*

04.10.95: R. Wiesendanger. Münster, Germany (Workshop on Surface Memories Using Atomically Resolving Techniques): *Interaction of surfaces with local probes: Novel routes to nanofabrication*

16.10.95: R. Wiesendanger. Minneapolis, USA (AVS'95): *Issues in Atomic-Resolution Structure and Chemical Analysis by Scanning Probe Microscopy and Spectroscopy*

7.2 Conference Contributions and Talks at Other Institutes

05.03.93: R. Wiesendanger. Düsseldorf, Germany (VDI-Veranstaltung): *Kombinierte SXM-Analyseverfahren*

30.04.93: R. Wiesendanger. Bad Honnef (Gemeinsame Sitzung der Arbeitskreise Mikro- und Nanotechnik sowie Optoelektronik): *Neue Entwicklungen in der Rastersonormikroskopie*

13.05.93: R. Wiesendanger. University of Hamburg (Kolloquium und Antrittsvorlesung): *Struktur und Strukturierung von Festkörperoberflächen bis zur atomaren Skala mittels Rastersondenmethoden*

25.05.93: R. Wiesendanger. Warsaw, Poland (Seminar Polish Academy of Sciences): *Effects of electron spin polarization in STM*

28.06.93: R. Wiesendanger. University of Duisburg, Germany (Kolloquium): *Lokale Eigenschaften von Festkörperoberflächen im Licht hochauflösender Rastersondenmethoden*

12.07.93: R. Wiesendanger. University of Tübingen, Germany (Kolloquium): *Neue Entwicklungen in der Rastersonormikroskopie*

13.08.93: R. Wiesendanger. Peking, China (STM'93): *Wigner glass on the magnetite (001) surface observed by STM with a ferromagnetic tip*

13.09.93: R. Wiesendanger. Yokokama, Japan (Seminar at SONY Research Center): *Contributions of Scanning Probe Microscopy and Spectroscopy to the Investigation and Fabrication of Nanostructures*

14.09.93: R. Wiesendanger. Tsukuba, Japan (Seminar at Electrotechnical Laboratory): *Contributions of Scanning Probe Microscopy and Spectroscopy to the Investigation and Fabrication of Nanostructures*

- 16.09.93:** R. Wiesendanger. Tsukuba, Japan (Seminar at Aono Atomcraft Project Laboratory): *Contributions of Scanning Probe Microscopy and Spectroscopy to the Investigation and Fabrication of Nanostructures*
- 28.09.93:** R. Wiesendanger. Jülich, Germany (1. Arbeitstreffen "Nanomodifikation von Oberflächen"): *Nanomodifikation von Oberflächen: Internationaler Stand der Technik, Handlungsbedarf*
- 28.10.93:** R. Wiesendanger. University of Paderborn, Germany (Kolloquium): *Neue Entwicklungen in der Rastersondenmikroskopie*
- 17.03.94** U. D. Schwarz, W. Allers, G. Gensterblum, R. Johnson, and R. Wiesendanger. Schluchsee, Germany (Conference of the NATO Advanced Study Institute (ASI) on Forces in Scanning Probe Methods): *Are C₆₀ molecules suitable as molecular ball-bearings?*
- 22.03.94** M. Löhndorf, F.Goerke, U.Merkt und R. Wiesendanger. Münster Germany (Frühjahrstagung der DPG): *Charakterisierung von YSZ-Pufferschichten und Untersuchung des Anfangstadiums des Wachstums von YBaCuO-Filmen auf Siliziumsubstraten.*
- 22.03.94** S. Lukas, U. D. Schwarz, M. Löhndorf, and R. Wiesendanger. Münster, Germany (Frühjahrstagung der DPG): *Nanostrukturierungsverfahren unter Umgebungsbedingungen mittels Rastersondenmethoden*
- 24.03.94** W. Allers, U. D. Schwarz, G. Gensterblum, R. Johnson, and R. Wiesendanger. Münster, Germany (Frühjahrstagung der DPG): *Können C₆₀-Moleküle als mikroskopische Kugellager dienen?*
- 04.05.94:** R. Wiesendanger. University of Chemnitz, Germany (Kolloquium): *Lokale Eigenschaften von Festkörperoberflächen im Licht hochauflösender Rastersondenmethoden*
- 11.05.94:** R. Wiesendanger. MPI Göttingen (Seminar): *Lokale Eigenschaften von Festkörperoberflächen im Licht hochauflösender Rastersondenmethoden*
- 27.06.94:** R. Wiesendanger. Hahn-Meitner-Institut Berlin, Germany (Kolloquium): *Lokale Eigenschaften von Festkörperflächen im Licht hochauflösender Rastersondenmethoden*
- 27.10.94:** R. Wiesendanger. Denver, USA (AVS/NANO-3): *Nanotribological Investigations of Epitaxial C₆₀ Films on GeS(001) by Lateral Force Microscopy and Force Spectroscopy*
- 06.07.95:** R. Wiesendanger. MPI für Festkörperforschung, Stuttgart, Germany (Seminar): *Rastersondenmikroskopie und -spektroskopie: Zugang zur Physik auf der Nanometerskala*

- 20.03.95** P. Köster, U. D. Schwarz, and R. Wiesendanger. Berlin, Germany (Frühjahrstagung der DPG): *Untersuchungen zur Problematik der quantitativen Analyse reibungskraftmikroskopischer Messungen*
- 20.03.95** A. Schwarz, U. D. Schwarz, H. Bluhm, and R. Wiesendanger. Berlin, Germany (Frühjahrstagung der DPG): *Bestimmung der Miller-Indizes von Seitenflächen kleiner Kristallite durch Winkelmessungen mittels Rasterkraftmikroskopie*
- 20.03.95** M. Dreyer, and R. Wiesendanger. Berlin, Germany (Frühjahrstagung der DPG): *Scanning Capacitance Microscopy and Charge Storage in NOS-Structures*
- 20.03.95** M. Löhndorf, A. Wadas, und R. Wiesendanger. Berlin, Germany (Frühjahrstagung der DPG): *Untersuchungen magnetischer Domänen dünner Permalloy-Strukturen mittels magnetischer Kraftmikroskopie (MKM).*
- 20.03.95** U. D. Schwarz, W. Allers, G. Gensterblum, and R. Wiesendanger. Berlin, Germany (Frühjahrstagung der DPG): *Reibungsverhalten von epitaktischen C_{60} -Monolagen auf GeS(001)*
- 23.03.95** A. Schwarz, U. D. Schwarz, H. Bluhm, W. Sager, and R. Wiesendanger. Berlin, Germany (Frühjahrstagung der DPG): *Wachstum von α - Fe_2O_3 -Nanokristalliten auf (0001) α - Al_2O_3 -Substrat*
- 23.03.95** W. Allers, U. D. Schwarz, G. Gensterblum, J.-J. Pireaux, and R. Wiesendanger. Berlin, Germany (Frühjahrstagung der DPG): *Rasterkraftmikroskopische Studie des Wachstums von C_{60} -Molekülen auf GeS*
- 23.03.95** R. Pascal, M. Bode, and R. Wiesendanger. Berlin, Germany (Frühjahrstagung der DPG): *STM-Studie der W(110)-Oberfläche auf atomarer Skala*
- 23.03.95** M. Bode, R. Pascal, and R. Wiesendanger. Berlin, Germany (Frühjahrstagung der DPG): *STM-Untersuchung des Wachstums von Eisen auf W(110) auf atomarer Skala*
- 23.06.95** H. Bluhm, U. D. Schwarz, K.-P Meyer and, R. Wiesendanger. Trieste, Italy (Adriatico Research Conference on Physics of Sliding Friction, NATO ASI Series): *Anisotropy of sliding friction on the TGS (010) surface*
- 29.05.95:** R. Wiesendanger. Universität Kiel, Germany (Kolloquium): *Rastersondenmikroskopie und -spektroskopie: Zugang zur Physik auf der Nanometerskala*
- 24.07.95** M. Löhndorf, A. Wadas, H. van Kesteren, and R. Wiesendanger. Snowmass, Colorado, USA (STM '95): *Domain Structure of Co/Pt Multilayers Studied by Magnetic Force Microscopy*

- 24.07.95** W. Allers, U. D. Schwarz, G. Gensterblum, J.-J. Pireaux and R. Wiesendanger. Snowmass, Colorado, USA (STM '95): *Growth of C_{60} thin films on $GeS(001)$ studied by scanning force microscopy*
- 25.07.95** H. Bluhm, K.-P. Meyer, and R. Wiesendanger. Snowmass, Colorado, USA (STM '95): *Domain structure, tip-induced growth and monolayer removal on the TGS (010) surface*
- 27.07.95** H. Bluhm, U. D. Schwarz, K.-P. Meyer, and R. Wiesendanger. Snowmass, Colorado, USA (STM '95): *Anisotropy of sliding friction on the TGS (010) surface*
- 28.07.95** U. D. Schwarz, W. Allers, G. Gensterblum, and R. Wiesendanger. Snowmass, Colorado, USA (STM '95): *Low-load friction behavior of epitaxial C_{60} monolayers under Hertzian contact*
- 10.08.1995** M. Bode, R. Pascal, and R. Wiesendanger. Snowmass, Colorado, USA (STM '95): *STM-Study of Carbon-Induced Reconstructions on $W(110)$: Strong Evidence for a Surface Lattice Deformation*
- 10.08.1995** M. Bode, R. Pascal, and R. Wiesendanger. Snowmass, Colorado, USA (STM '95): *Imaging and Tunneling Spectroscopy of Individual Fe-adatoms, clusters and ultrathin films by UHV-STM at 300 K*
- 10.08.1995** U. D. Schwarz, H. Bluhm, W. Allers, and R. Wiesendanger. McGill University, Montreal, Canada (Seminar): *Friction force microscopy: Approaching the fundamentals of wearless friction*
- 11.05.95:** R. Wiesendanger. RWTH Aachen, Germany (Seminar): *Rastersondenmikroskopie und -spektroskopie: Zugang zur Physik auf der Nanometerskala*
- 05.12.95:** R. Wiesendanger. Braunschweig, Germany (Kolloquium): *Rastersondenmikroskopie und -spektroskopie: Zugang zur Physik auf der Nanometerskala*

Chapter 8

Talks Given by Guests

- 19.04.1993** Prof. Dr. K. Mukasa (Hokkaido University, Japan): *Observation of spin-polarized photo-induced electron tunneling in a scanning tunneling microscope with GaAs and Ni.*
- 03.05.1993** Dr. H. Pinkvos (TU Clausthal): *Untersuchung magnetischer Domänen in ultradünnen Co-Schichten mittels spinpolarisierter Oberflächenelektronenmikroskopie.*
- 10.05.1993** Dr. U. Köhler (Universität Hannover): *In-situ STM-Untersuchungen von CVD-Wachstumsvorgängen auf Si(111)-Oberflächen.*
- 17.05.1993** Dr. J. Heil (Hochfeldmagnetlabor Grenoble, Frankreich): *Punktkontakt-spektroskopie und Rastertunnelmikroskopie bei tiefen Temperaturen.*
- 07.06.1993** Dipl.-Phys. H.-P. Lang (Universität Basel, Schweiz): *Rastertunnelmikroskopie an Hochtemperatursupraleiterschichten und -ein- kristallen.*
- 09.06.1993** Dr. O. Wolter (Nanosensors Wetzlar): *Mikrofabrikation von Sonden für lokale Rastensensormethoden.*
- 11.06.1993** Prof. Dr. D. Tománek (Michigan State University, USA): *C₆₀ and its derivatives: A plethora of unexpected phenomena.*
- 21.06.1993** Dipl.-Phys. B. Meyer (TU Hamburg-Harburg): *Rastensensormikroskopie-Aktivitäten an der TU Hamburg-Harburg.*
- 23.06.1993** Prof. Dr. J. C. Lodder (University of Twente, NL): *Preparation and Microstructure of Thin Films for High-Density Recording.*
- 16.07.1993** Dr. E. Schweizer (FHI Berlin): *Manipulation einzelner Atome mit dem 4-Kelvin-STM.*
- 02.08.1993** Prof. Dr. E. Torikai (University of Tokyo, Japan): *Spin dynamics in the 2-dimensional ferromagnetic superlattice: first application of muon spin rotation method for an extremely thin film.*

- 25.10.1993** Dipl.-Phys. K. Schiffmann (FHI für Schicht- und Oberflächentechnologie Hamburg/Braunschweig): *Rastersondenmikroskopie an dünnen Schichten.*
- 03.11.1993** Prof. Dr. H. Dimigen (FHI für Schicht- und Oberflächentechnologie Hamburg/Braunschweig): *Schicht- und Oberflächentechnologie.*
- 03.12.1993** Dr. T. A. Jung (IBM Yorktown Heights, USA): *Neue Entwicklungen in der Rastersondenmikroskopie.*
- 08.12.1993** Prof. Dr. O. Poulsen (Mikroelektronik Center Copenhagen, Dänemark): *Forschungsaktivitäten am neuen Mikroelektronikzentrum in Kopenhagen.*
- 05.01.1994** Dr. Graeger (Philips Hamburg): *Temperatur- und Magnetsensoren sowie deren Anwendungen.*
- 12.01.1994** Prof. Dr. W. Göpel (Universität Tübingen): *Nanostructures based on molecular materials.*
- 17.01.1994** Dr. H. van Kesteren (Philips Eindhoven, NL): *Co/Pt-Multilagensysteme.*
- 21.01.1994** Dr. G. Persch (IBM Mainz): *Anwendungen der Rastersondenmikroskopie für die Produktion von Magnetplattenspeicher.*
- 14.01.1994** Dr. R. Wolf (Philips Eindhoven, NL): *Magnetit-Filme und Multilagensysteme.*
- 31.01.1994** Dr. S. Magonov (Universität Freiburg i.Brsg.): *Towards a rational interpretation of STM and AFM images.*
- 09.03.1994** Dr. H. Tokumoto (Tsukuba, Japan): *Nanotechnology Program and Current Status of Nanotechnology Research at the Joint Research Center for Atom Technology.*
- 29.03.1994** Dr. R. M. Overney (Tokyo Institute of Technology, Japan): *Kraft- und Reibungsmikroskopieuntersuchungen an molekularen Systemen.*
- 20.04.1994** Dr. Ch. Schoenenberger (Philips Eindhoven, NL): *Single Electron Tunneling.*
- 21.04.1994** Prof. Dr. K. Lüders (FU Berlin): *Supraleitende Fullerene.*
- 02.05.1994** Dipl.-Phys. R. Koltun (RWTH Aachen): *Aufbau eines UHV-STM und Anwendung auf magnetische Messungen an Magnetit auf atomarer Skala.*
- 11.05.1994** Dr. H. P. Oepen (Forschungszentrum Jülich): *Magnetische Eigenschaften ultradünner, epitaktischer Filme: Co auf Cu.*

- 18.05.1994** Dr. D. P. E. Smith (IBM Physik-Gruppe München): *Neue Entwicklungen in der Rastersondenmikroskopie.*
- 01.06.1994** Dr. M. Lux-Steiner (Universität Konstanz): *Unkonventionelle Verbindungshalbleiter für die Photovoltaik und die Nanostrukturierung.*
- 16.06.1994** Prof. Dr. F. Besenbacher (Universität Århus, Dänemark): *Atomare Struktur und Dynamik auf Metalloberflächen.*
- 23.06.1994** Dr. R. Berndt (Universität Lausanne, Schweiz): *Subnanometer-Auflösung in Photonemissions-Experimenten.*
- 30.06.1994** Prof. Dr. W. Kraetschmer (MPI für Kernphysik, Heidelberg): *Fullerene und Fullerite: Neue Formen des Kohlenstoffs.*
- 04.07.1994** Dr. Th. Schimmel (Universität Bayreuth): *Rastersondenverfahren als Werkzeuge zur Nanostrukturierung.*
- 06.07.1994** Prof. Dr. G. Schön (Universität Essen): *Kleine Metallcluster und ihre mögliche Anwendung in der Mikroelektronik.*
- 11.07.1994** Dr. Ch. Ziegler (Universität Tübingen): *Rastersondenmikroskopie an molekularen Systemen.*
- 20.07.1994** Prof. Dr. U. Hartmann (Universität Saarbrücken): *Von der makroskopischen zur mikroskopischen Analyse des supraleitenden Zustands: Ein Streifzug durch die wichtigsten experimentellen Methoden.*
- 05.09.1994** Dr. M. Johnson (Naval Research Laboratory Washington, USA): *Spin-Valves and Spin-Transistor.*
- 05.09.1994** Prof. Dr. A. Itoh (Nihon University, Japan): *Spin-Polarized Scanning Tunneling Microscopy.*
- 05.09.1994** Dr. T. Kawagoe (Nihon University, Japan): *Recent STM experiments at Nihon University.*
- 15.09.1994** Dr. C. Chapelier (SPSMS Grenoble, Frankreich): *Experimental observation of persistent currents in a single mesoscopic loop.*
- 15.09.1994** Prof. Dr. J. Raulusiewicz (Polish Academy of Sciences, Warschau, Polen): *Current research activities at the Polish Academy of Sciences.*
- 26.09.1994** Dr. T. Shen (University of Leeds, Great Britain): *Growth and characterization of metallic multilayers.*
- 07.11.1994** Dipl.-Phys. R. Berger (Universität Erlangen- Nürnberg): *Rastersondenmikroskopie an Hochtemperatursupraleitern.*

- 25.11.1994** Dr. T. A. Jung (IBM Rüschlikon, Schweiz): *Neue Entwicklungen in der Rastersondenmikroskopie.*
- 05.01.1995** Dr. B. N. J. Persson (Forschungszentrum Jülich): *On the theory of friction and boundary lubrication.*
- 12.01.1995** Prof. Dr. J. Miltat (Universität Paris, Frankreich): *Magnetische Mikrostrukturforschung.*
- 26.01.1995** Dr. J. Mannhart (IBM Rüschlikon, Schweiz): *Nanostrukturen aus Hochtemperatur-Supraleitern: Physik und Anwendungen.*
- 27.01.1995** Prof. Dr. M. Henzler (Universität Hannover): *Charakterisierung der Wachstumsformen bei der Epitaxie mit Elektronenbeugung und Rastertunnelmikroskopie.*
- 27.01.1995** Prof. Dr. H. Neddermeyer (Universität Halle): *Rastertunnelmikroskopie in Echtzeit an Silizium-Oberflächen.*
- 27.01.1995** Dr. F. Grey (Mikroelektronik Center Copenhagen, Dänemark): *Fabrication of Nanostructures by the Scanning Tunneling Microscope.*
- 27.01.1995** Dr. H. Rotermund (FHI Berlin): *Photoemissions-Elektronenmikroskopie-Untersuchungen raum-zeitlicher Strukturbildung bei nichtlinearen Oberflächenreaktionen: Der Einfluß von Mikrostrukturen.*
- 27.01.1995** Prof. Dr. A. Hubert (Universität Erlangen-Nürnberg): *Magnetische Mikrostrukturforschung.*
- 27.01.1995** Prof. Dr. P. Grünberg (Forschungszentrum Jülich): *Zwischenschichtkopplung in magnetischen Multilagensystemen.*
- 27.02.1995** Prof. Dr. S. A. Nepijko (TU Clausthal-Zellerfeld): *Magnetism of small particles.*
- 22.05.1995** Dr. J. Buisset (FHI Berlin): *Hochauflösende STM-Untersuchungen an Adsorbaten auf Einkristall-Metalloberflächen zwischen 4 K und 300 K.*
- 12.06.1995** Prof. Dr. U. Gradmann (TU Clausthal-Zellerfeld): *Ultradünne magnetische Filme.*
- 29.06.1995** Prof. Dr. D. Kern (Universität Tübingen): *Ein miniaturisiertes Elektronenmikroskop: Konzeption und Anwendungen.*
- 07.07.1995** Dipl.-Phys. K. Schiffmann (FHI für Schicht- und Oberflächentechnologie Braunschweig): *Rastersondenmikroskopie und Kleinwinkelstreuung an metallhaltigen Kohlenwasserstoffschichten.*

- 10.07.1995** Dr. V. Vill (Universität Hamburg): *Flüssigkristalle*.
- 13.07.1995** Dr. D. W. Pohl (IBM Rüschlikon, Schweiz): *Nahfeldoptische Mikroskopie und Spektroskopie*.
- 18.07.1995** Prof. Dr. M. H. Whangbo (North Carolina State University, USA): *Importance of tip-sample force interactions in the STM/AFM image interpretation*.
- 08.08.1995** Dr. J. Barth (FHI Berlin): *Rastertunnelmikroskopie an Metalloberflächen*.
- 18.08.1995** Dr. M. Getzlaff (Universität Mainz): *Elektronische und magnetische Eigenschaften von dünnen magnetischen Schichten*.
- 15.09.1995** Prof. Dr. D. Drakova (Universität Sofia, Bulgarien): *Theory of STS for clean and adsorbate covered metal surfaces*.
- 23.11.1995** Dr. T. A. Jung (IBM Rüschlikon, Schweiz): *Molekulare Nanostrukturen aus einzelnen Molekülen: Herstellungsmethoden, Struktur und Funktion*.
- 27.11.1995** Dipl.-Phys. T. Müller (Universität Konstanz): *Rasterkraftmikroskopie und Reibungskraftmikroskopie unter Ultrahochvakuumbedingungen*.
- 07.12.1995** Prof. Dr. L. Samuelson (Lund University, Sweden): *Manipulation and probing of quantum dots*.
- 18.12.1995** Dipl.-Phys. P. Weitz (MPI f. Festkörperforschung Stuttgart): *Tief-temperatur-Rasterkraftmikroskopie an Halbleiter-Mikrostrukturen*.

Chapter 9

Lectures and Courses at the University of Hamburg

Einführung in die Struktur der Materie (Kursusvorlesung)

Aktuelle Themen der Festkörperphysik

Einführung in die Nanotechnologie

Einführung in die Rastertunnel- und Rastersonormikroskopie I und II

Anwendungen der Rastertunnel- und Rastersonormikroskopie I und II

Oberflächen- und Grenzflächenphysik mit spinpolarisierten Elektronen

Ringvorlesung "Physik der Mikrostrukturen"

Seminar über hochauflösende Mikroskopie an Festkörperoberflächen

Seminar über lokale Methoden in der Festkörperphysik

Seminar über Nahfeldgrenzflächenphysik

Proseminar über Rastertunnelmikroskopie und verwandte Rastersonormethoden

Proseminar über Neue Materialien

Übungen zur Einführung in die Struktur der Materie

Übungen zur Einführung in die Rastertunnel- und Rastersonormikroskopie

Laborpraktikum

Diplompraktikum

Chapter 10

Contributions to International Organisations and Journals

- Member of the Program Committee of the international semiconductor conference “ICFSI-4” (Jülich 1993)
- Member of the Program Committee of the “5th European Conference on Electron and Optical Beam Testing of Electronic Devices” (Wuppertal 1995)
- Co-Organizer of the Symposium “Physics of Microstructures” (Hamburg 1995)

Journals

- Co-editor of Applied Physics A (topic “Nanostructure Physics and Technology”)

Chapter 11

How to reach us

... by mail	write to University of Hamburg, Microstructure Advanced Research Center and Institute of Applied Physics, Jungiusstraße 11, D-20355 Hamburg, Germany.
... by phone	call (+49) 40 4123 2028.
... by fax	send to (+49) 40 4123 6368.
... by e-mail	send to <code>group\$r@physnet.uni-hamburg.de</code>
... within the WWW	open http://www.physnet.uni-hamburg.de/ fb12/angew-wi.html
... personally	

